THE INTERACTION OF DNA WITH NANO-STRUCTURED BETA-GALLIA RUTILE INTERGROWTHS

BY

NATHAN H. EMPIE

A THESIS

SUBMITTED TO THE FACULTY OF

ALFRED UNIVERSITY

IN PARTIAL FULFILLMENT OF THE REQUIREMENTS
FOR THE DEGREE OF

DOCTOR OF PHILOSOPHY

IN

MATERIALS SCIENCE & ENGINEERING

ALFRED, NEW YORK

OCTOBER, 2006

THE INTERACTION OF DNA WITH NANO-STRUCTURED BETA-GALLIA RUTILE INTERGROWTHS

BY

NATHAN H. EMPIE

B.S. ALFRED UNIVERSITY (2002)

SIGNATURE OF AUTHOR (Signature on file)

APPROVED BY (Signature on file)
DOREEN D. EDWARDS, ADVISOR

(Signature on file)
ALASTAIR N. CORMACK, ADVISORY COMMITTEE

(Signature on file)
ALEXIS G. CLARE, ADVISORY COMMITTEE

(Signature on file)
MATTHEW M. HALL, ADVISORY COMMITTEE

(Signature on file)
DOREEN D. EDWARDS, CHAIR, ORAL THESIS DEFENSE

ACCEPTED BY (Signature on file)
ALASTAIR N. CORMACK, DEAN
KAZUO INAMORI SCHOOL OF ENGINEERING

ACCEPTED BY (Signature on file)
WILLIAM M. HALL, ASSOCIATE PROVOST
FOR GRADUATE AND PROFESSIONAL PROGRAMS
ALFRED UNIVERSITY

ACKNOWLEDGMENTS

I would like to thank Dr. Edwards for her help and guidance throughout the course of this study, as well as the input and feedback of my committee members. Special thanks to Carrie, my family, and my friends for understanding the times when I couldn't be there, and truly making the most of the times when I was. Additional thanks to my co-workers, the faculty, and supporting staff here at Alfred University. This research has been supported by the National Science Foundation (DMR-0093690) and the National Defense Science and Engineering Fellowship.

TABLE OF CONTENTS

Page

ACKNOWLEDGMENTS iii

TABLE OF CONTENTS iv

LIST OF TABLES vii

LIST OF FIGURES viii

1 INTRODUCTION **1**

1.1 References 6

2 BACKGROUND **7**

2.1 Nano-Devices Based on Deoxyribonucleic Acid 7

2.2 Atomic Force Microscopy of DNA on Mica 17

2.3 Beta-Gallia Rutile Intergrowths 23

2.4 References 27

3 PHASE STABILITY AND STRUCTURE OF ALKALI DOPED BETA-GALLIA RUTILE INTERGROWTHS **35**

3.1 Introduction 35

3.2 Experimental Methods 40

3.3 Simulation Methods 40

3.4 Results and Discussions 43

3.4.1 Phase analysis 43

3.4.2 Computer simulations of $A_xGa_{4+x}Ti_{1-x}O_8$ 48

3.4.3 Computer simulations of $Na_{0.8}Ga_{4.8}Ti_{1.2}O_{10}$ and $Na_{0.8}Ga_{4.8}Ti_{2.2}O_{12}$ 56

3.5 Conclusions 61

3.6 References 62

4 AN ATOMIC FORCE MICROSCOPY STUDY OF THE INTERACTION OF DNA AND NANO-STRUCTURED BETA-GALLIA RUTILE **64**

4.1 Introduction 64

4.2 Experimental Procedure 66

4.3 Results and Discussion 68

4.3.1 Beta-gallia rutile synthesis 68

4.3.2 DNA attachment studies 74

4.4 Conclusions 84
4.5 References 86
5 THE ATTACHMENT OF DNA TO BETA-GALLIA RUTILE SURFACES AS A FUNCTION OF DNA SOLUTION AGE 89
5.1 Introduction 89
5.2 Experimental Procedure 93
5.2.1 Synthesis of beta-gallia rutile substrates 93
5.2.2 AFM imaging 93
5.2.3 DNA solution preparation 93
5.2.4 Reporting bound DNA concentration 94
5.2.5 Gel electrophoresis 94
5.3 Results and Discussion 94
5.3.1 AFM results and discussion 94
5.3.2 AFM results and discussion 97
5.4 Conclusion 106
5.5 References 109
6 DNA ATTACHMENT TO BETA-GALLIA RUTILE SURFACES AS A FUNCTION OF DIVALENT CATIONIC CONCENTRATION 112
6.1 Introduction 112
6.2 Experimental Procedure 115
6.2.1 Substrate synthesis 115
6.2.2 DNA preparation 116
6.2.3 AFM Imaging 116
6.2.4 Degree of binding preference 116
6.3 Results and Discussion 117
6.3.1 Strength of attachment 127
6.4 Conclusion 132
6.5 References 133
7 SUMMARY AND CONCLUSION 137
7.1 Future Directions 139
7.1.1 BGR substrate 139
7.1.2 DNA preparation 140
7.1.2 Binding mechanism 140

7.1 References 141

LIST OF TABLES

Page

Table 3.I. Known Alkali Gallium Titanium Oxide Phases with One-dimensional Tunnels 38

Table 3.II. Potential Parameters used in this Study 42

Table 3.III. Phase Analyses of Samples Prepared as $A_xGa_{4+x}Ti_{1-x}O_8$ 44

Table 3.IV. Phase Analyses of Samples Prepared as $Na_yGa_{4+Y}Ti_{2-y}O_{10}$ 45

Table 3.V. Structural Parameters and Lattice Energy of Ga_4TiO_8 and $A_{0.7}Ga_{4.7}Ti_{0.3}O_8$ 49

Table 3.VI. Minimized Lattice Energies of Observed and Component Oxides 50

Table 3.VII. Comparison of the Lattice of Energy of Ga_4TiO_8 to Compositionally Equivalent Mixtures 50

Table 3.VIII. Structural Parameters and Lattice Energy of $A_{0.8}Ga_{4.8}Ti_{1.2}O_{10}$ 57

Table 3.IX. Structural Parameters and Lattice Energy of $A_{0.8}Ga_{4.8}Ti_{2.2}O_{12}$ 58

Table 4.I. Summary of DNA Attachment to BGR Surfaces 75

Table 4.II. Summary of DNA Attachment to TiO_2 Surfaces 76

LIST OF FIGURES

Page

Figure 1.1. Polyhedral models of a) the surface structure of an n=25 BGR intergrowth; b) the (001) cleavage surface of muscovite mica. 2

Figure 1.2. Schematic of DNA binding to divalent cations occupying BGR intergrowth tunnel sites. 4

Figure 2.1. Image of DNA double helix structure. 8

Figure 2.2. Diagram of deoxyribose sugar and connecting phosphate groups of the DNA structure. 9

Figure 2.3. Diagram of complementary nitrogenous base binding in DNA structure. a) A = adenine to T = thymine. b) G = guanine to C = cytosine. c) Diagram of a hybridized DNA chain with complementary bases bound via hydrogen bonds. 10

Figure 2.4. Schematic diagram of molecular self-assembly of nanoparticles. 12

Figure 2.5. Schematic diagram of a "DNA junction" formed from four partially complementary ssDNA molecules. 13

Figure 2.6. Schematic diagram of: a) "Dip-pen nanolithography" process to pattern molecularly active "inks" on non-adsorbing substrates. 16

Figure 2.7. a) Polyhedral model of the layered structure of muscovite mica 19

Figure 2.8. a) Polyhedral model of the (001) cleavage plane of muscovite mica 20

Figure 2.9. Polyhedral model of a) the (010) plane of beta-gallia.. 24

Figure 2.10. Polyhedral model of the (010) plane of an n=9 BGR ($Ga_4Ti_5O_{16}$). 25

Figure 2.11. Diagram of BGR $\{210\}_r$ intergrowth boundary orientation 26

Figure 3.1. B-axis projection of BGR-derived $A_xGa_{4+x}Ti_{n-4-x}O_{2n-2}$ structures 36

Figure 3.2. B-axis projection of reported $A_xGa_{4+x}Ti_{n-4-x}O_{2n-2}$ structures 39

Figure 3.3. Prepared compositions in relationship to compatibility triangles..... 46

Figure 3.4. Calculated (minimized) lattice energies of BGR-derived structure, observed phase mixture, and component oxide mixture as a function of x in $Li_xGa_{4+x}Ti_{1-x}O_8$. 52

Figure 3.5. Calculated (minimized) lattice energies of BGR-derived structure, observed phase mixture, and component oxide mixture as a function of x in $Na_xGa_{4+x}Ti_{1-x}O_8$. 53

Figure 3.6. Calculated (minimized) lattice energies of BGR-derived structure, observed phase mixture, and component oxide mixture as a function of x in $K_xGa_{4+x}Ti_{1-x}O_8$. 55

Figure 4.1. Projection of the ß-gallia rutile ($Ga_4Ti_{21}O_{48}$) structure along [001] of the parent rutile structure, after Ref. [24]. 67

Figure 4.2. AFM height images (10 x 10 μm) of a) bare single crystal [001]

TiO_2 (z range: 100 nm). 69

Figure 4.3. a) SEM micrograph of BGR surface, and b) Auger electron spectroscopy overlay of (a).. 71

Figure 4.4. Preferential alignment of intergrowth boundaries observed in: a) AFM height image (10 x 10 μm) of BGR fired at 1350 ^oC for 96 hours (z range: 100 nm) 72

Figure 4.5. Relative line density as a function of heating time. Sample B was heated at 1350 ^oC.. 73

Figure 4.6. AFM height image (1 x 1 μm, z range: 10 nm) of DNA molecules bound to a BGR surface.. 77

Figure 4.7. a) AFM height image (50 x 50 μm, z range: 300 nm) of the edge of a buffer coating on a BGR surface. 79

Figure 4.8. AFM images (1 x 1 μm) of DNA attached to BGR surfaces in the presence of a) Co (II) (phase image, z range: 35^o).. 80

Figure 4.9. AFM image (1 x 1 μm) of DNA attached to a [001]-oriented single crystal TiO_2 surface in the presence of Ni (II) (height image, z range: 15 nm).. 81

Figure 4.10. A comparison of the density of DNA attached to$\{210\}_r$ intergrowths (solid bars) to the density of DNA observed along random lines along the surface of BGR substrates (dashed bars) for different divalent cation. 83

Figure 5.1. a) AFM phase image (1.75 x 1.75 μm, z-range: 15^o) demonstrating the preferential attachment of DNA along $\{210\}_r$ intergrowth boundaries of a BGR surface... 90

Figure 5.2. a) AFM image (1.2 x 1.2 μm, z-range: 10 nm) of a bare BGR surface.. 92

Figure 5.3. Average linear DNA density along $\{210\}_r$ intergrowth boundaries as a function of DNA solution age. 95

Figure 5.4. AFM scans (1.5 x 1.5 μm, z-scale 10 nm) of BGR surfaces exposed to DNA solutions containing additions of 1 mM $CoCl_2$ at a buffer age of: a) 1 day, and b) 42 days. 96

Figure 5.5. Average degree of DNA preference for $\{210\}_r$ intergrowth boundaries as a function of DNA solution age.. 98

Figure 5.6. Average linear DNA density along $\{210\}_r$ intergrowth boundaries as a function of DNA solution (containing 1 mM MCl_2) age 99

Figure 5.7. AFM image (2 x 2 μm scan, z-scale: 8 nm), post rinsing, of a freshly prepared DNA solution containing 5 mM $MgCl_2$ dried to a BGR surface. 100

Figure 5.8. Electrophoresis gel of new and aged DNA solutions containing additions of $MgCl_2$.. 101

Figure 5.9. Electrophoresis gel of new and aged DNA solutions containing additions of $NiCl_2$. 102

Figure 5.10. AFM scans (1.5 x 1.5 μm, z-scale 18 nm) of BGR surfaces exposed to freshly prepared DNA solutions containing additions of: a) 0.5 mM $NiCl_2$. b) 5.0 mM $NiCl_2$. 105

Figure 5.11. AFM scan (5 x 5 μm, z-scale 30 nm, 78 day-old buffer) of a BGR surface exposed to a DNA solution containing the addition of 0.5 mM $CoCl_2$. 107

Figure 6.1. a) AFM image (1.5 x 1.5 μm, z-scale: 15 μm) of a bare BGR surface. The bright line running left to right is a $(210)_r$ intergrowth boundary..... 114

Figure 6.2 Average linear DNA densities as a function of cation species and cation concentration..... 118

Figure 6.3. AFM images (3 x 3 μm, z scale: 30nm) of: a) A BGR surface exposed to a DNA solution containing 1 mM $ZnCl_2$..... 120

Figure 6.4. A schematic of a DNA solution droplet (grey) drying on a BGR surface..... 121

Figure 6.5. Average degree of DNA preference for $\{210\}_r$ intergrowth boundaries on BGR surfaces as a function of cation species and concentration..... 123

Figure 6.6. Average linear DNA density along $\{210\}_r$ boundaries as a function of cation concentration and cation species.. 124

Figure 6.7. AFM images (1.5 x 1.5 μm, z-range: 15 nm) of BGR surfaces exposed to DNA solutions containing additions of: a) 0.5 mM $ZnCl_2$ b) 1.0mM $ZnCl_2$ c) 5.0 mM $ZnCl_2$..... 126

Figure 6.8. AFM images (1.5 x 1.5 μm) of BGR surfaces exposed to DNA solutions containing additions of: a) 0.5 mM $NiCl_2$ (z-scale: 15nm) 128

Figure 6.9. AFM images (1.5 x 1.5 μm, z-scale: 15nm) of BGR surfaces exposed to DNA solutions containing additions of: a) 0.5 mM $CoCl_2$. b) 1.0 mM $CoCl_2$. c) 5.0 mM $CoCl_2$..... 129

Figure 6.10. AFM images (1.5 x 1.5 μm) of BGR surfaces exposed to DNA solutions containing additions of: a) 0.5 mM $MgCl_2$ (z-scale: 15nm)..... 130

Abstract

The demand for viable methods to fabricate nano-devices has driven research into the realm of molecular self-assembly. This thesis outlines a procedure to synthesize beta-gallia rutile (BGR) substrates capable of preferentially binding DNA molecules. The information provided serves as a basis to direct future research toward the patterning of BGR surfaces to facilitate self-assembled DNA nano-constructs. The ability to tailor the separation and orientation of preferentially binding $\{210\}_r$ intergrowth boundaries could enable BGR surfaces to be used as nano-assembling substrates to benefit nano-biologic, electronic and mechanical technologies.

This research initially focused on a sol gel method to apply thin films of Ga_2O_3 to single-crystal [001] oriented TiO_2 substrates. The thermal treatments were systematically studied to obtain a better understanding of how time and temperature influence the formation of the intergrowth structure. Atomic force microscopy (AFM) was used to observe the alignment of the synthesized intergrowth regions.

A 100bp-ladder DNA solution was applied to BGR and bare [001]-oriented rutile substrates. The surfaces were investigated with tapping mode AFM. It was identified from the generated images that DNA deposition solutions containing 1.0 mM additions of select divalent chlorides facilitated the preferential attachment of DNA along $\{210\}_r$ intergrowth regions of BGR surfaces. The large deviations within recorded DNA densities and binding preferences were attributed primarily to the effect of DNA solution aging.

Investigations involving mono-sized, 1000 bp DNA solutions were conducted to determine the influence that cation concentration and DNA solution age had on DNA attachment. Evaluating the density of bound DNA molecules and their end-to-end distances led to insights into the binding behavior. For each cation species and concentration tested, the greatest DNA density was observed at a cation concentration of 1.0 mM; further additions in salt concentration led to decreases in DNA density. Results of bound DNA end-to-end distances reveal that the binding strength of DNA molecules had increased with increasing cation concentration. The results of this research provide

increased knowledge about the interaction of DNA with oxide surfaces and may influence the development of new molecular electronic devices.

1. Introduction

The National Nanotechnology Innitiative (NNI) defines the need for research to explore matter and its interaction at the intermediate length scale between single atoms / molecules and groups of molecules ranging from 1 to 100nm, as it could prove valuable in the development of efficient nano-scale manufacturing methods.[1] Researchers have answered the call, and the development of molecular directed-assembly is an area of intense interest. The sequence –specific binding of deoxyribonucleic acid (DNA) and the wealth of methods to control both its synthesis and processing make it the molecule of choice for the majority of self-assembly studies.

Attaching DNA selectively to surfaces has been attained using surface functionalization strategies teamed with a variety of nano-patterning methods. These techniques all appear to possess certain limitations including (but not limited to) poor spatial resolution, high cost, intensive fabrication time requirements, and cumbersome techniques. While some studies focus on optimizing current technology, others seek alternate methods. The goal of this work was to investigate the interaction of DNA and beta-gallia rutile (BGR) surfaces to determine if this system could lend itself as a substrate for the self-assembly of DNA constructs.

Based on structural considerations and previous reports on the interaction of DNA with mica surfaces, it was hypothesized that the beta-gallia rutile surface could serve as a novel substrate that would facilitate the alignment of DNA. Beta-gallia rutile is an intergrowth structure, characterized by periodic tunnels (voids in the lattice) which run parallel to the [001] direction and are aligned in rows along the $[210]_r$ directions of the parent rutile structure (Figure 1.1a). The spacing between the $[210]_r$ rows of hexagonal tunnels on the BGR intergrowth surface can be varied from ~1 nm to ∞ by varying the rutile-to-gallia ratio. The 1-D tunnels are ~ 0.25 nm in diameter and can accommodate small-to-medium sized cations. Hexagonal- shaped recesses are inherent to cleaved mica surfaces as well (Figure 1.1b). For muscovite mica, the recesses are occupied by K (I) cations, which can be exchanged for cations of a higher valence.

Previous researchers have shown that DNA binds to the mica surface in the presence of divalent cations. While the mechanism for binding is not well understood, it

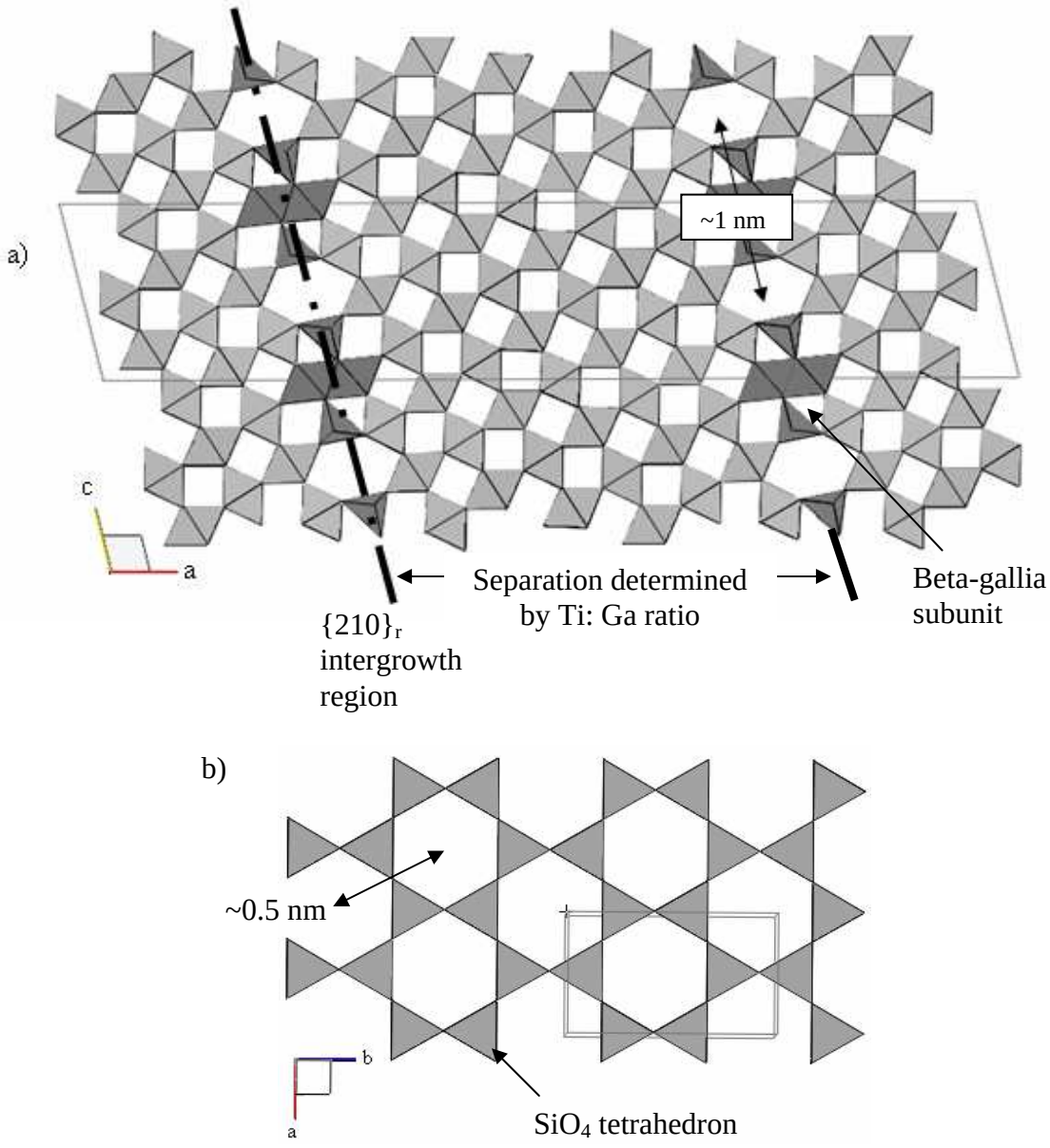

Figure 1.1. Polyhedral models of a) the surface structure of an n=25 BGR intergrowth; two dimensional projections of TiO_6 octahedra are shown in light grey, GaO_6 octahedra and GaO_4 tetrahedra in dark grey. b) The (001) cleavage surface of muscovite mica; two dimensional projections of SiO_4 tetrahdra shown in grey. Both BGR and mica surfaces possess hexagonal sites large enough to accommodate small to mid-sized cations.

has been suggested that divalent cations sitting in/on the hexagonal sites of the mica surface may provide an electrostatic bridge between the negatively charged mica surface and the DNA backbone.[2,3] The current work was initiated under the supposition that a similar binding mechanism may occur between DNA and the intergrowth tunnel (Figure 1.2). Unlike mica, the BGR intergrowth surface possesses a tailored periodicity and may possess site-specific reactivity that would facilitate the long-range alignment (patterning) of DNA molecules, which may be beneficial for the construction of molecular devices.

This dissertation is presented as a collection of four stand-alone manuscripts that have been submitted to peer-reviewed journals:

- ***Phase Stability and Structure of Alkali Doped Beta-Gallia Rutile Intergrowths.***[4]

  This paper describes an investigation of the phase stability of $A_xGa_{4+x}Ti_{1-x}O_8$ using experimental investigations and atomistic computer simulations. The $A_xGa_{4+x}Ti_{1-x}O_8$ compound is structurally related to the BGR intergrowths used for DNA attachment studies.

- ***An Atomic Force Microscopy Study of the Interaction of DNA and Nano-Structured Beta-Gallia Rutile.***[5]

  This paper describes the preparation of BGR intergrowth substrates and DNA (multi-sized) attachment studies in the presence of various divalent cations using atomic force microscopy.

- ***The Attachment of DNA to Beta-Gallia Rutile Surfaces as a Function of DNA Solution Age.***

  This paper describes the influence DNA solution age has on the degree of DNA (mono-sized) attachment, investigated using atomic force microscopy and gel electrophoresis.

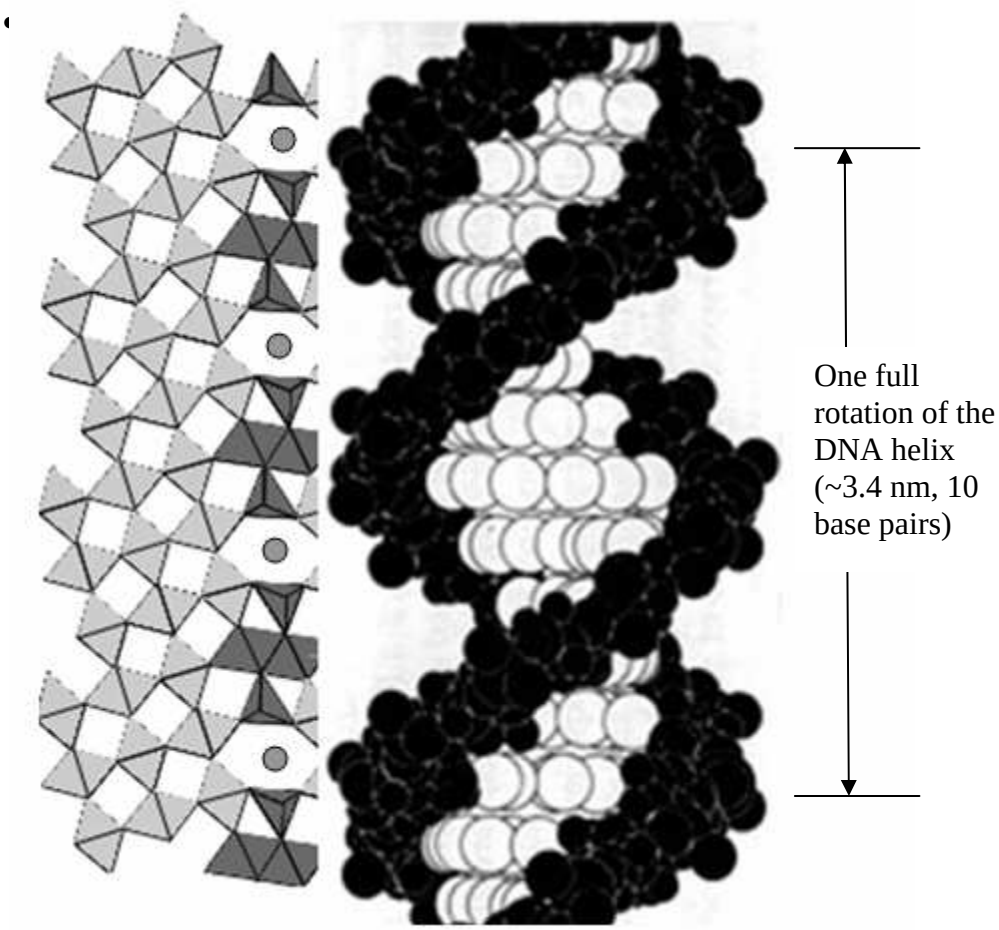

Figure 1.2. Scaled schematic of DNA binding to divalent cations occupying BGR intergrowth tunnel sites. The DNA backbone is roughly in alignment with every third BGR tunnel site. Partial image of DNA structure from www.labbies.com.

DNA Attachment to Beta-Gallia Rutile Surfaces as a Function of Divalent Cationic Concentration.

This study targets the influence that cation concentration has on the degree (via the quantity of bound molecules) and strength (via molecular conformation) of mono-sized DNA attachment using atomic force microscopy.

Each of the four manuscripts contains its own introduction, description of experimental details, results & discussion, conclusions, figures, and list of references. Preceding the four manuscripts is a chapter that provides a more thorough review of the literature relevant to the four manuscripts. Following the compilation is a general summary and conclusion which makes some recommendations for future work.

1.1. References

1. M.C. Roco, "Nanoscale Science and Engineering: Unifying and Transforming Tools," *AIChE J.,* **50** [5] 890-7 (2004).

2. H.G. Hansma and D.E. Laney, "DNA Binding to Mica Correlates with Cationic Radius: Assay by Atomic Force Microscopy," *Biophys. J.,* **70** [4] 1933-9 (1996).

3. N.H. Thomson, S. Kasas, B.L. Smith, H.G. Hansma, and P.K. Hansma, "Reversible Binding of DNA to Mica for AFM Imaging," *Langmuir,* **12** [24] 5905-8 (1996).

4. N. Empie and D. Edwards, "Phase Stability and Structure of Alkali Doped-beta-gallia Rutile Intergrowths," *Solid State Ionics,* **177** [1-2] 77-87 (2006).

5. N. Empie and D. Edwards, "Atomic Force Microscopy Study of the Interaction of DNA and Nano-structured Beta-gallia Rutile," *Langmuir,* **22** [18] 7678-63 (2006).

2. Background

2.1. Nano-Devices Based on Deoxyribonucleic Acid

Deoxyribonucleic acid (DNA) is a molecular biopolymer approximately two-nanometers in diameter (Figure 2.1). DNA is composed of stacked nucleotide blocks, which can exist in different conformations. The most common DNA conformation (in vivo) is B-DNA. The surface plane of each nucleotide base in B-DNA is perpendicular to the helix axis. Each base pair is rotated 36^{o} and spaced 3.4 Å from its adjacent pair.[1] At approximately every tenth base pair (3.4 nm) the helix has performed a full turn. B-DNA is the favored conformation at high water concentrations. As the DNA strand becomes dehydrated, it can take on an A-DNA conformation. This right-handed helix is shorter, and wider than B-DNA. Approximately 11 base pairs comprise one full rotation, and each base pair is spaced ~2.7Å apart.

Each DNA nucleotide consists of three parts: a deoxyribose sugar (a five-carbon cyclic sugar), a pyrimidine or purine (nitrogenous) base, and a phosphate group to attach the deoxyribose sugars (Figure 2.2). Purine (double ring) bases include adenine (A) and guanine (G); pyrimidine (single ring) bases include thymine (T) and cytosine (C).[1] Each base has a complement that it pairs with (and only with): T to A and C to G (Figure 2.3 a, b). Each single DNA strand is a covalent unit on its own; once paired they become a non-covalent molecule attached via hydrogen bonding to form a stable double helix (Figure 2.3c). Two hydrogen bonds form between T and A while three form between C and G. DNA helices with a greater percentage of C-G base pairs are more stable because of more hydrogen bonds. The joining of two complementary single-stranded DNA (ssDNA) molecules via hydrogen bonding is termed hybridization.

Modern biology has equipped us with the tools to exploit DNA hybridization and apply it to nano-fabrication. Automated methods exist to manufacture and amplify (via the polymerase chain reaction (PCR)) any DNA sequence. Single-stranded DNA molecules possessing complementary sequences can be synthesized and will self-assemble in appropriate conditions. Additionally, highly specific enzymes (endo- / exonucleases, ligases) exist that are capable of processing DNA molecules with atomic

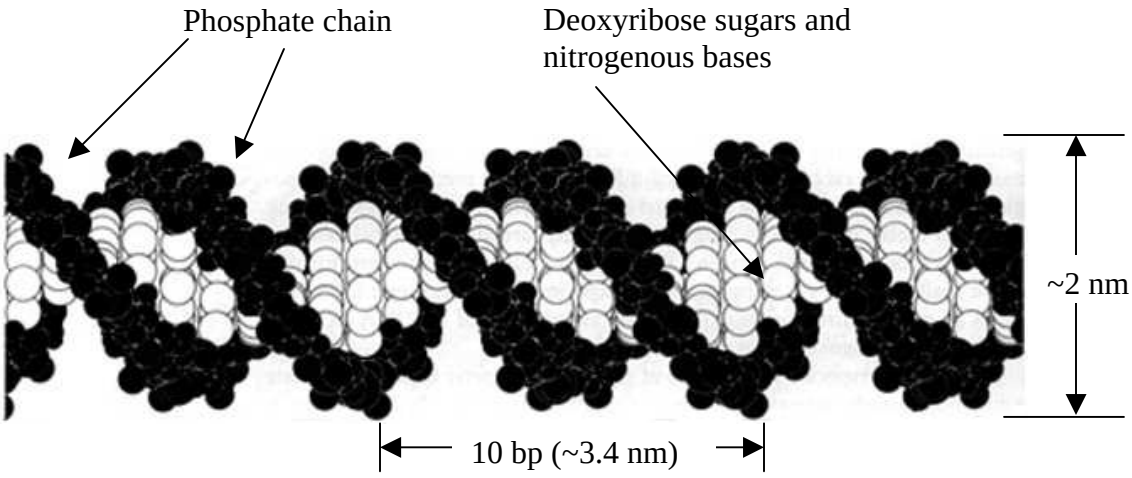

Figure 2.1. Image of DNA double helix structure. The phosphate backbone is shown in black and the deoxyribose sugars and nitrogenous bases are shown in white. Image of DNA structure from www.labbies.com.

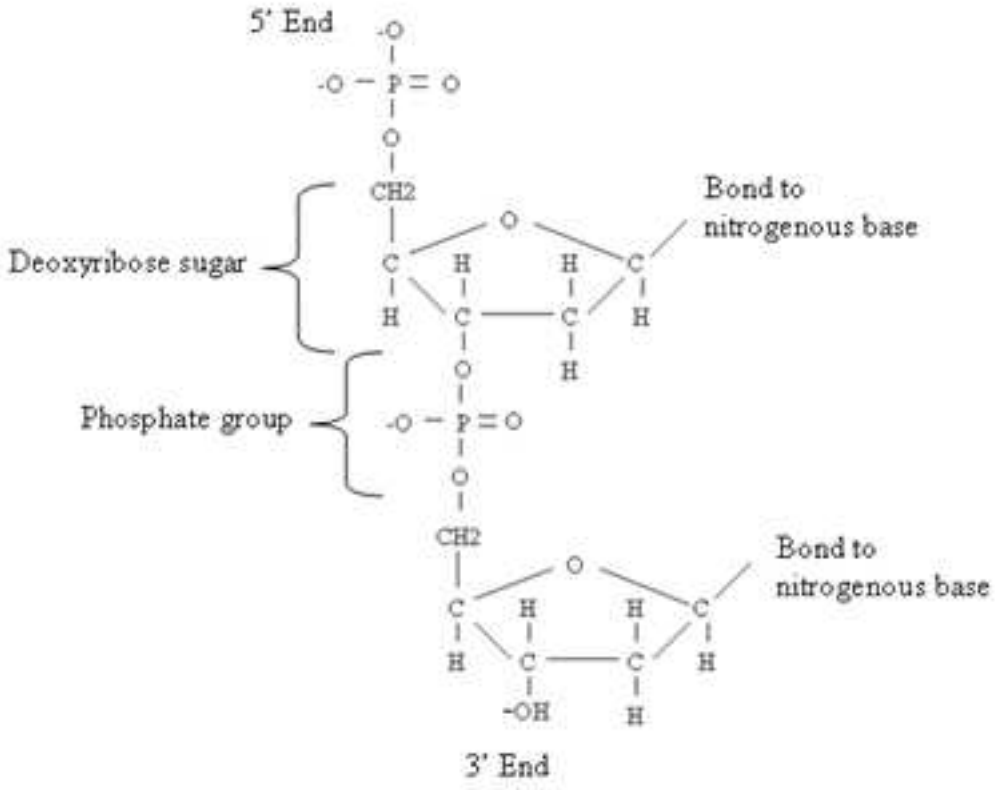

Figure 2.2. Diagram of deoxyribose sugar and connecting phosphate groups of the DNA structure.

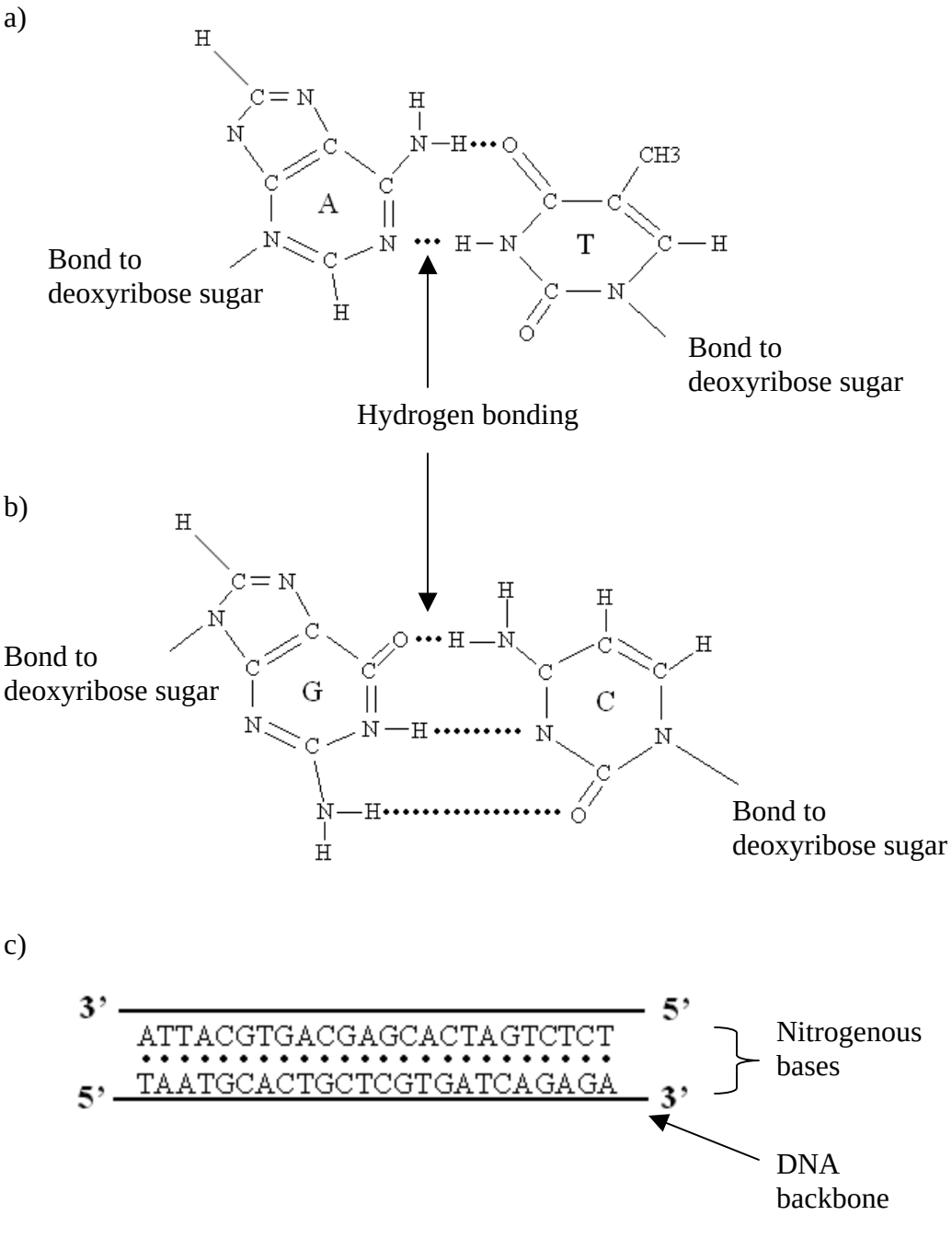

Figure 2.3. Diagram of complementary nitrogenous base binding in DNA structure. a) A = adenine to T = thymine. b) G = guanine to C = cytosine. c) diagram of a hybridized DNA chain with complementary bases bound via hydrogen bonds.

precision and angstrom level accuracy.[2,3] Synthesized double-stranded DNA (dsDNA) molecules can be bound to a substrate, the unbound end can be selectively cut (via endo- / exonucleases) to generate a ssDNA overhang ("sticky end").[4,5] A single-stranded oligonucleotide, or a dsDNA molecule with a sticky end possessing the complement to the overhang can then hybridize to it.[2,3,6] This process of binding complementary ssDNA molecules is the basis of biochip and microarray sensor technologies for biological diagnostics. DNA hybridization can also be used to selectively self-assemble micro and nano-scale assemblies of molecules and nano-particles (Figure 2.4).[3,6,7] By patterning ss-DNA molecules (or dsDNA with sticky ends) to a substrate, they will selectively distinguish and bind their complementary chain along with any additionally linked nano-particles, or molecules.

For the last few decades Nadrian Seeman has been exploring designable, branched DNA structures.[4,5,8-11] By synthesizing and combining select sequences of DNA molecules "dna junctions" were generated which led to the development of more intricate 2-D and 3-D architectures (Figure 2.5). The 2-D constructs are envisioned to serve as scaffolding for nano-electronic components. Once DNA frameworks were constructed, they could be coated with silver or palladium to form nano-wires.[12-14] M-DNA provides another accepted conduction pathway. Here, cations are bonded directly between the nucleic acids, replacing the imino proton of each base pair of the DNA helix.[15-17] The insertion of metal ions into the DNA structure converts the DNA into a molecular wire, proven to conduct.[15-17]

The development of regular DNA lattices can also act as nano-cages, immobilizing large biological molecules into periodic arrays facilitating x-ray crystallography studies of their structure.[8] A number of DNA-based nano-mechanical applications have been developed including DNA "triggers"[8] and "tweezers"[18] capable of aligning and manipulating matter on the nanoscale.

Presented above are a few examples where DNA is being used in bottom-up approaches to fabricate nano-devices. A major limitation to DNA-mediated assembly remains the development of patterned, site-specific, DNA-reactive substrates onto which these applications can be built. A number of current approaches to achieve suitable

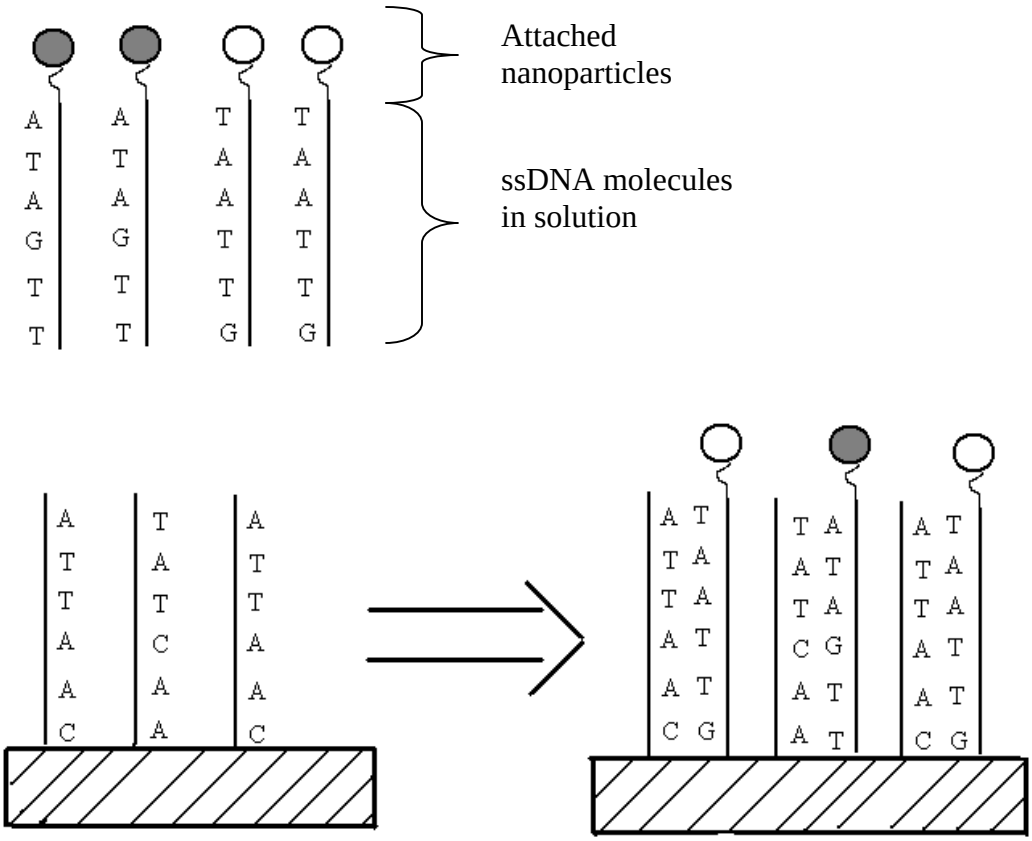

Figure 2.4. Schematic diagram of molecular self-assembly of nanoparticles. ssDNA molecules in solution bind with their anchored complements, directing the site-specific assembly of attached nanoparticles.

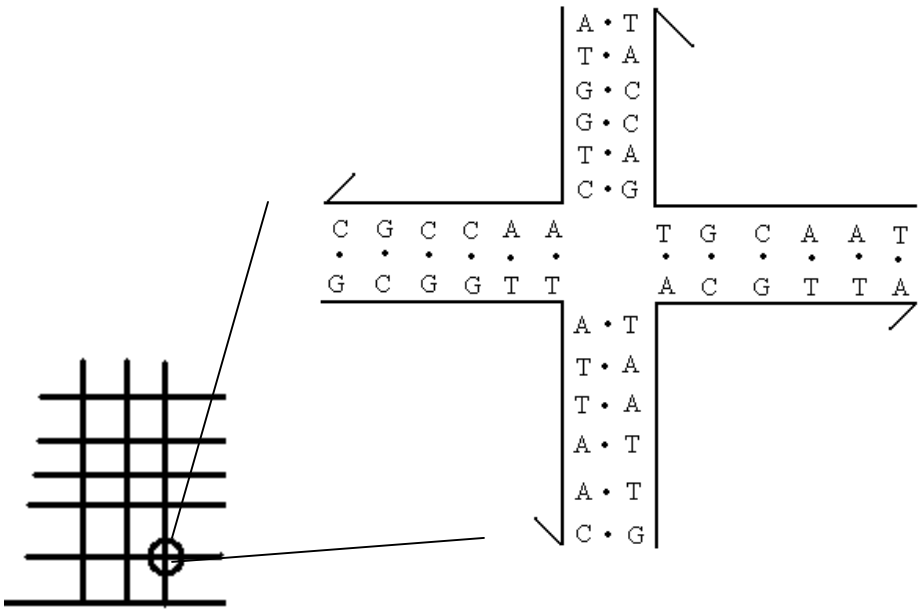

Figure 2.5. Schematic diagram of a “DNA junction” formed from four partially complementary ssDNA molecules. Collections of DNA junctions could be assembled to form 2-D and 3-D networks of DNA.

substrates involve the utilization of surface functionalization teamed with a nano-patterning process.

A common surface functionalization method involves the gold-thiol interaction. Gold is relatively inert to biomolecules, requiring a reactive anchoring molecule for immobilization to occur.[19] Thiols and other molecules (dialkylsulfides, dialkyldisulfides) with exposed sulfur functional groups covalently bind to gold surfaces with a high affinity.[20,21] Thiol functional groups can be applied to DNA molecules via polymerase chain reaction using oligonucleotide primers with thiol groups bound to their ends, enabling the thiol tagged DNA molecule to selectively bind to a gold surface at its endpoint.[20] Endpoint binding can be desirable because it allows the DNA backbone to be free to interact with enzymes or DNA binding proteins. Applying functionalization methods to surfaces will provide a means to bind DNA; but, to spatially orient DNA selectively upon these surfaces requires additional patterning methods. Patterning via photolithographic- and probe-based processes are being investigated, but appear to possess significant limitations currently inhibiting their scale up.

Photolithography involves the generation of an intricately patterned mask which is used to selectively shield / expose an underlying photosensitive polymeric material, which can then be etched to yield a patterned surface. Patterns can easily be applied to gold substrates, allowing only exposed surfaces to bind with thiolated-DNA molecules. This technology abounds; unfortunately there exist major limitations to traditional photolithography. The first drawback lies with the size scale of the generated patterns. The microelectronics industry has optimized the photolithographic process to yield features on the order of 100 nm; below these scales, blurring of the patterned features results from light diffraction.[22] This size scale will not be sufficient to keep up with demands of industry, academia, and the consumer, so alterations must be made. Pushing the light source to extreme UV or X-ray wavelengths may appear a solution, but prove damaging to current mask and lens materials.[23] Electron-beam lithography can provide a means to achieve smaller scaled patterns as well; unfortunately the process is too expensive, and inefficient for large-scale production. Limitations in size scale teamed with ever rising costs of photolithographic tools currently prove prohibitive to those outside of the microelectronics industry.

Soft lithography may provide a means to reduce the cost of e-beam and photolithographic processes, while creating nanoscale patterned surfaces.[22,24,25] Soft lithography involves the generation of a bas-relief master mold via e-beam or photolithography. The master is then used to make a polydimethylsiloxane (PDMS) stamp. The stamp can be used a number of ways: in a process called "microcontact printing",[22] the stamp is inked with a thiol solution, applied to a gold or gold coated surface, where the thiols form a self-assembled monolayer (maintaining the pattern on the stamp. Features as small as 50 nm have been reported using this process.[22] A second process, termed "micromolding in capillaries",[22] involves the PDMS stamp being flush against a surface, while a liquid polymer is applied along the periphery. The polymer is pulled into the recesses between the surface and the stamp. The polymer is solidified and maintains the stamps pattern. Features as small as 10 nm have been reported using this process.[22] A limitation to soft lithographic patterning methods is observed if the fabrication of multiple layered structures is desired. Misalignment of stamped patterns could result in a malfunctioning nano-electronic device. "Bleeding" of some functionalized inks can also influence the spatial resolution of this application process.

Dip pen nanolithography (DPN) is a probe-based process which involves the transfer of an "ink" from a coated AFM tip to a sample surface (Figure 2.6a).[26,27] DPN probes are commonly prepared by soaking the AFM tips in desired inks, then drying the tips in nitrogen.[28] Depending on the substrate, an appropriate ink can be selected to accommodate the desired attachment. Beyond DPN pattering with thiolated inks on gold substrates, a method developed by Demers *et al.* described the patterning of DNA on SiO_2 substrates. The SiO_2 surface was activated by treatment with 3'mercaptopropyltrimethoxysilane; while the AFM tip applied an ink of oligonucleotides with 5'-terminal acrylamide groups.[27] Depending on the AFM tip, substrate, and ink selected, the DPN process is capable of producing feature sizes less than 15 nm.[29] A major limitation to DPN is based around ink replenishment. A single tip lacks sufficient ink to draw large or complicated patterns, so when the ink runs out, the tip must be removed from the surface for re-coating. Once contact with the pattern is lost, a series of realignment procedures is required to resume construction. A tool termed the

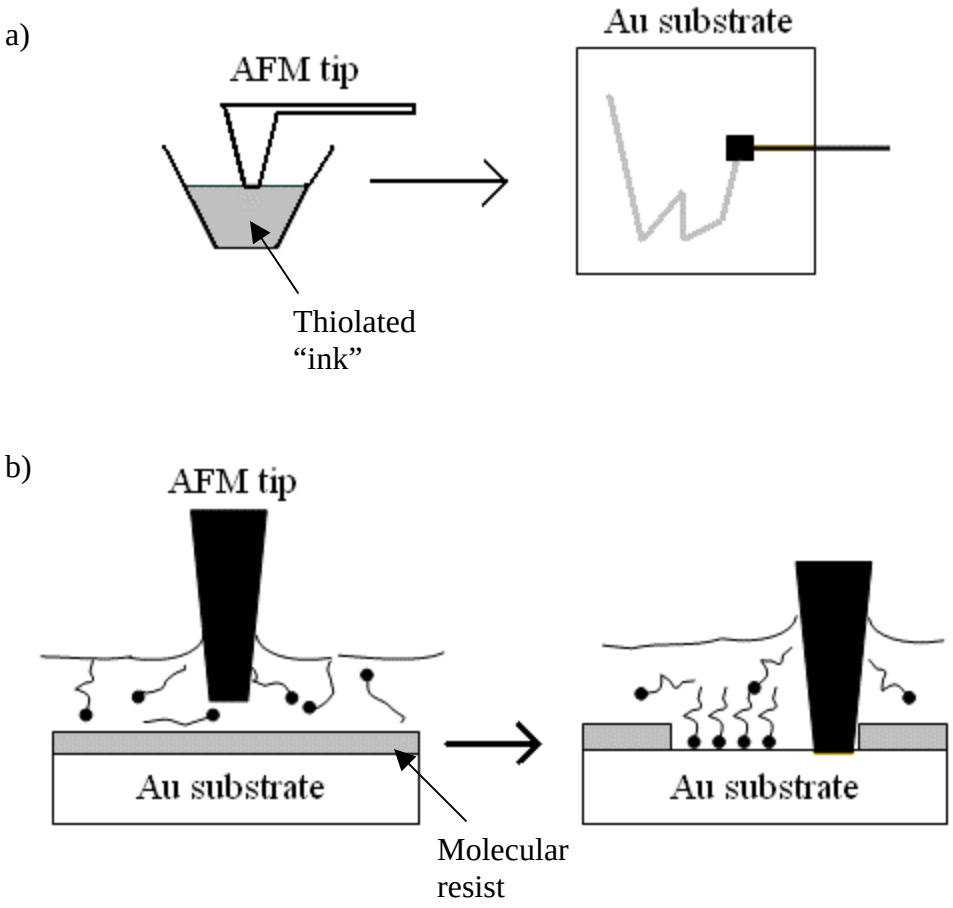

Figure 2.6. Schematic diagram of: a) "Dip-pen nanolithography" process to pattern molecularly active "inks" on non-adsorbing substrates. b) "Meniscus force nanografting" process to pattern molecules via the selective removal of a molecular resist.

"Nanofountain Probe" was recently developed by Kim *et al*. to allow continuous ink application without tip re-coating.[29] The hollow tipped probe contains integrated microchannels which deliver ink from a reservoir to the tip via capillary action. DPN with "nanofountain" tips were capable of writing patterns with line widths as small as 40 nm.[29]

Meniscus force nanografting (MFN) involves the selective removal of a self-assembled monolayer (SAM) resist to reveal reactive sites on an underlying substrate (Figure 2.6b).[28] For a gold substrate: a droplet of a solution of thiols with protein adhesive terminal groups can be applied to a SAM coated surface. The AFM tip is forced into the SAM, displacing the resist molecules. The thiol molecules in solution then bind selectively to the newly exposed gold surface behind the path of the AFM tip. Patterned lines have been formed at rates as fast as 320 μm / s.[21] Structure sizes resemble those obtained with DPN, on the order of 10 nm line widths.[28] Although extremely small patterns can be constructed by probe-based techniques, the output of these processes is far too limited to support large scale production. The use of numerous, automated probes may address this limitation, but for now these methods remain insufficient for scale up.

2.2. Atomic Force Microscopy of DNA on Mica

The atomic force microscope (AFM), developed by Bining *et al*. in the 1980s, enables the imaging of surfaces at the atomic scale.[30] Interest in molecular biology and genetics spurred AFM exploration into the structure of DNA and the molecules' interaction with other proteins. AFM investigation of molecular structure requires a substrate possessing both atomic flatness and a means to bind DNA molecules with sufficient strength to withstand tip-scanning forces. If DNA is bonded too weakly it will not be imaged by AFM, instead the AFM tip will simply move the DNA molecules across the substrate. If the DNA molecules are bound too tightly, they may become denatured on the substrate surface. Mica has emerged as the preferred substrate for AFM investigation of DNA structure. The atomic flatness of the mica surface is ideal to achieve molecular resolution.

Mica minerals are layered crystals with atomically flat cleavage planes over several hundred square-microns.[31] An aluminum-octahedral sheet resides at the center of a muscovite mica ($KAl_2(Si_3Al)O_{10}(OH)_2$) layer, sandwiched between two silicon-tetrahedral sheets (Figure 2.7).[32,33] Three quarters of the tetrahedral sheet sites are occupied by Si and one quarter by Al.[34] The replacement of Si (IV) by Al (III) leads to a charge imbalance which is compensated by interlayer potassium cations (for muscovite).[35] The potassium cations reside on recessed hexagonal oxygen rings (Figure 2.8) (with a spacing of 0.5 nm) on the cleavage surface ((001) plane), binding the laminar mica layers.[31,36-38] Cleaving a mica crystal, and exposing the surface to water, leads to the dissociation of some K (I) ions from the mica surface, generating an overall negative surface charge density at neutral pH.[31,39] The potassium ions remaining along the cleaved mica surface can be exchanged for cations of equal or higher valence. In a study by Osman *et al.* the muscovite cleavage surface was exposed to a hot lithium nitrate-water mixture to obtain a surface covered with Li^+ ions (the rate to exchange for Li (I) was found to be much faster than the rate to exchange for K^+).[40] The Li (I) rich surface was then exposed to alkali chloride solutions containing Na (I), K (I), Rb (I), and Cs (I) to induce ion-exchange. There exists a distinction when categorizing the type of interaction between the cation and the hexagonal surface sites along the mica surface, namely the ability of a cation to absorb into- as opposed to adsorb onto-these cavities. Nishimura *et al.* described that only cations on the size scale of Li (I), and Mg (II) could fit into the recessed sites.[41]

Initial experiments conducted on mica involved DNA solutions applied to freshly cleaved mica surfaces, rinsed with water, and imaged with the AFM. The negative surface charge of mica impedes the binding of negatively charged DNA. In order to increase the binding affinity between these surfaces a modification to the mica surface or the binding environment is required.[42] In numerous studies, it was shown that the addition of certain divalent cations facilitated the binding of DNA to mica surfaces.[36,42-55] Initially, only Ni (II) cations were found capable of binding DNA to mica surfaces sufficiently enough to allow AFM imaging without drying.[56] Hansma *et al*. investigated a series of divalent cations with fluid tapping AFM and determined that buffers

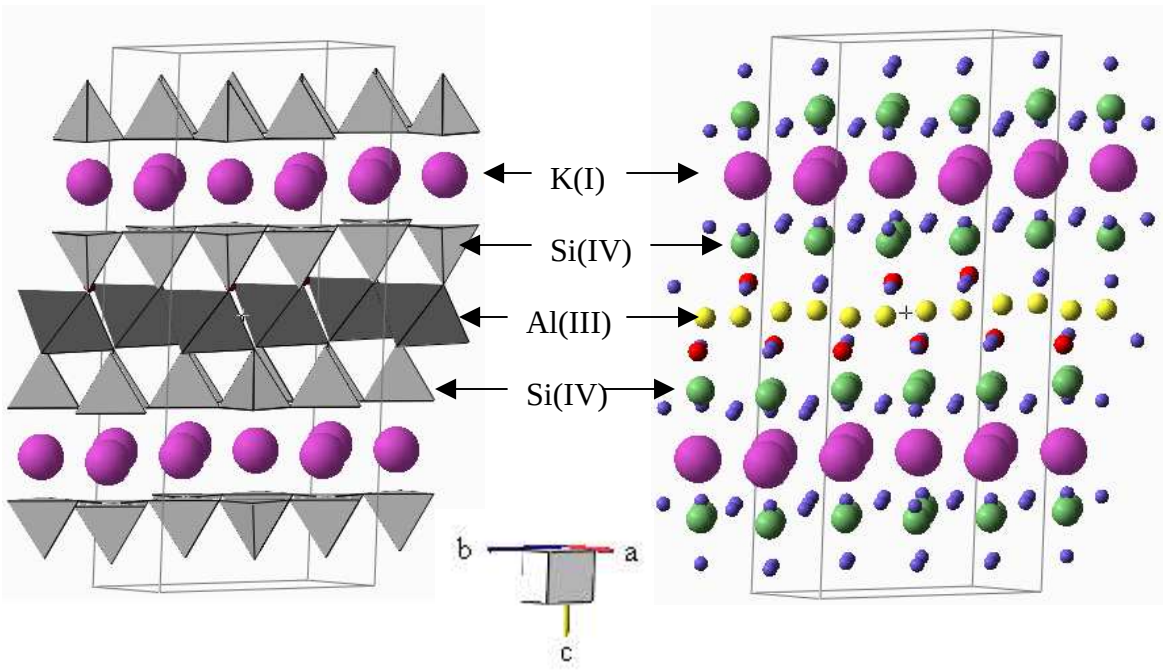

Figure 2.7. a) Polyhedral model of the layered structure of muscovite mica. Cleavage occurs along the (001) plane populated by K (I) ions. Dark grey octahedra are AlO_6 and tetrahedra of SiO_4 are shown in light grey. b) Atomistic model of (a).

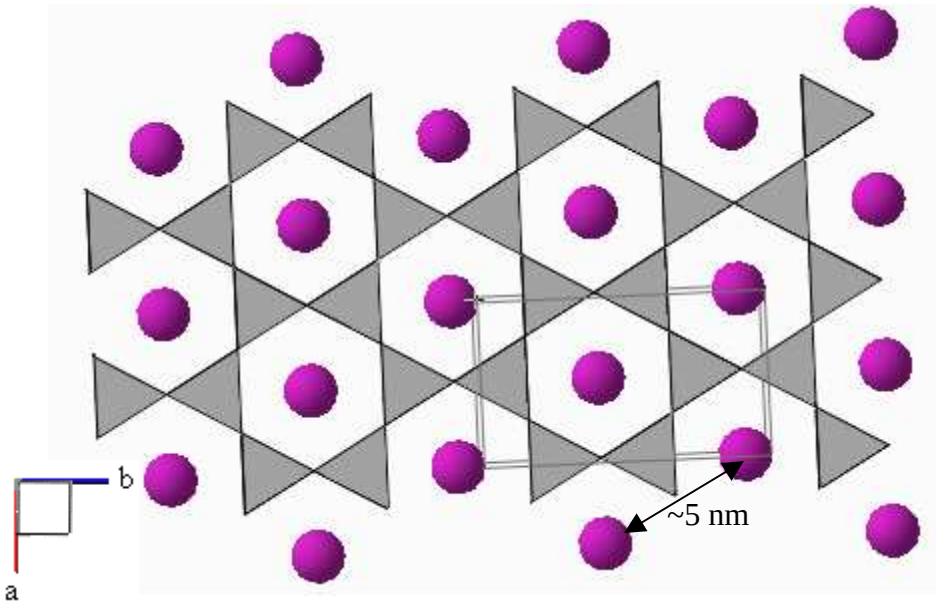

Figure 2.8. a) Polyhedral model of the (001) cleavage plane of muscovite mica. Grey tetrahedral represent SiO_4. Hexagonal surface cavities possess a spacing of ~5 nm and are occupied by K (I) ions (spheres).

containing additions of Co (II), Mn (II), and Zn (II) also enabled stable attachment of DNA.[48] It was determined that cationic size may play a significant role in the binding strength, suggesting that the smaller cations were capable of residing within the hexagonal recesses of the mica surface effectively bridging the two negatively charged surfaces.[43,45,47-49,53,57-59] Hansma *et al*., however, reported that Mg (II) ions (possessing a similar ionic radii to Ni (II)) were unable to bind DNA to mica surfaces, and attributed this result (possibly) to the lower hydration enthalpy of Mg (II).[48] Additionally, a correlation between ionic concentration and density of bound DNA molecules was observed. Increasing salt concentration to 1.0 mM resulted in an increase in concentration of bound DNA; while further increases typically resulted in subsequent decreases in bound DNA concentration.[48] The effect observed above 1.0 mM levels was attributed to a mass action effect, where both the DNA and mica surfaces become so saturated with cations that the probability of cation bridging is reduced.[48] The exact mechanism of DNA to mica attachment is unknown, but the importance of divalent cation incorporation has been recognized.[44,45,48,51-53,58-62] The interaction of divalent cations to DNA molecules has been investigated previously; according to Izatt et al. cations have been shown to exhibit affinities to either phosphate groups along the DNA backbone or to nucleotide base binding sites.[63] The affinity of divalent cations to bind at nucleotide bases instead of the phosphate groups was determined to increase in the following order: Mg (II), Co (II), Ni (II), Mn (II), Zn (II), Cd (II), and Cu (II).[63,64]

The strength of molecular attachment has been linked to the DNA molecules bound conformation. In strongly bound situations (termed “kinetic trapping”) the DNA molecule is immobilized on the surface so rigidly that its conformation in 2D will resemble that of a projected 3D conformation.[51,65] Alternatively, a weaker bound molecule will be able to equilibrate onto the surface in a 2D conformation. The end-to-end distance of a DNA molecule could therefore reflect the strength of molecular attachment. The strength of DNA attachment is important depending on the application. When investigating DNA- protein interactions it is important that the molecule is bound firmly enough to withstand the scanning force, but bound loose enough so its natural conformation and reactivity are maintained. As described by Stein *et al*., the ends of the DNA molecule are more negatively charged than its mid-segment, so with proper

immobilization conditions the extremities of DNA will be bound, while the inner portions are not.[66,67] It has been previously observed that the strength of attachment can be tailored by altering the pH of the solution buffer,[67] or introducing concentrations of monovalent ions to divalent deposition solutions.[51] In terms of nano-molecular devices, post-attachment processing of molecules requires a more loosely bound molecule. The alignment of bound molecules in particular has received a considerable amount of attention. In a process termed "molecular combing",[68] end bound DNA molecules are stretched and aligned in the direction of a receding air-water interface by an associated meniscus force. One method of molecular combing involves applying a drop of DNA solution onto a DNA reactive substrate, upon which an un-reactive cover slip is floated on top of the droplet spreading it across the entire substrate surface. The solution can then be evaporated, or the cover slip can be withdrawn at a given rate to allow the receding interface to align the DNA molecules. Additional methods to achieve aligned molecules have been developed; most depend on the meniscus force generated by a receding air/ fluid interface.[67,69-75]

Mica has proven itself to be an ideal surface to investigate molecular species; however, it appears to bind DNA non-uniformly, reflecting the natural diversity of mica surface properties.[54] In order for mica to be used as a substrate to fabricate nano-devices, additional functionalization and patterning steps (such as those described above) will be required, which may prove inefficient or expensive to justify their employment. Beta-gallia rutiles (BGRs) are intergrowth phases possessing nano- and microscale features that can be tailored by altering the material's chemistry. Among those nano-scale features are periodically occurring hexagonal tunnel sites of a similar size to the hexagonal recesses of mica surfaces. The occurrence of similar surface sites between these two substrates generates an interest to investigate if DNA binding interactions will behave similarly as well. The interaction of BGR surfaces with molecular species has not previously been investigated, but will be examined in this thesis.

2.3. Beta-Gallia Rutile Intergrowths

The series of BGR intergrowth phases can be described by $Ga_4M_{n-4}O_{2n-2}$, where M is cation of the rutile forming family (Sn, Ge, or Ti).[76-79] For the scope of this work intergrowths solely involving Ti as M, will be examined. Analysis of the Ga_2O_3-TiO_2 system was first reported by Lejus *et al*. in 1959, where a structurally-unknown ternary phase was observed stable above 1570 K.[80] It was not until 1972, when a study by Gibb and Anderson identified the structure of a series of oxide phases in the Ga_2O_3-TiO_2 system as $Ga_4Ti_{m-4}O_{2m-2}$ (m = odd, between 15 and 23).[81] Further investigations into the Ga_2O_3-TiO_2 system have led to BGR intergrowth phases being expressed as: $Ga_4Ti_{n-4}O_{2n-2}$, where n is >9 (n= 5, 7 were found metastable, only existing at limited temperature ranges).[76-78,82,83] The BGR intergrowth structure may be described as a [½, ¼, ½] $(210)_r$ crystallographic shear phase, derived from rutile by the periodic removal of $(210)_r$ plane of atoms, with a sequential displacement of the rutile slabs by the vector $[-½, ¼, ½]_r$.[83] The limited degree of lattice mismatch (<3%) allows the insertion of beta-gallia (Figure 2.9a) subunits (b-axis oriented parallel to the $[001]_r$) into $(210)_r$ planes of rutile (Figure 2.9b), leading to the formation of one-dimensional hexagonal-shaped tunnel sites.[79] The unit cell of a BGR intergrowth (n=25, $Ga_4Ti_{21}O_{48}$) is presented in Figure 2.9c. An expanded unit cell (along the $[001]_r$ surface of rutile) is provided to aid in visualizing the alignment of tunnel sites and beta-gallia groups along $\{210\}_r$ planes (Figure 2.9d). BGR intergrowths represent a series of compounds, where changes in the ratio of Ga:Ti (n value) result in contraction or expansion between $\{210\}_r$ intergrowth regions (compare Figure 2.9 c / d (n=25) to Figure 2.10 (n=9)).

The formation of $\{210\}_r$ BGR intergrowth boundaries were observed in samples prepared by applying finely powdered Ga_2O_3 onto a [001]-oriented single crystal TiO_2 substrate with firing in excess of 1500^{o}C, where Bursill *et al*. observed a "maze of intersections and junctions" of $\{210\}_r$ boundaries.[82] Similar results were obtained by firing [001]-oriented rutile single crystal surfaces coated with gallium nitrate hydrate solutions.[84] Figure 2.11 displays the various orientations of intersecting $\{210\}_r$ boundaries. In the work of Bursill *et al.,* the random orientation of $\{210\}_r$ intergrowth

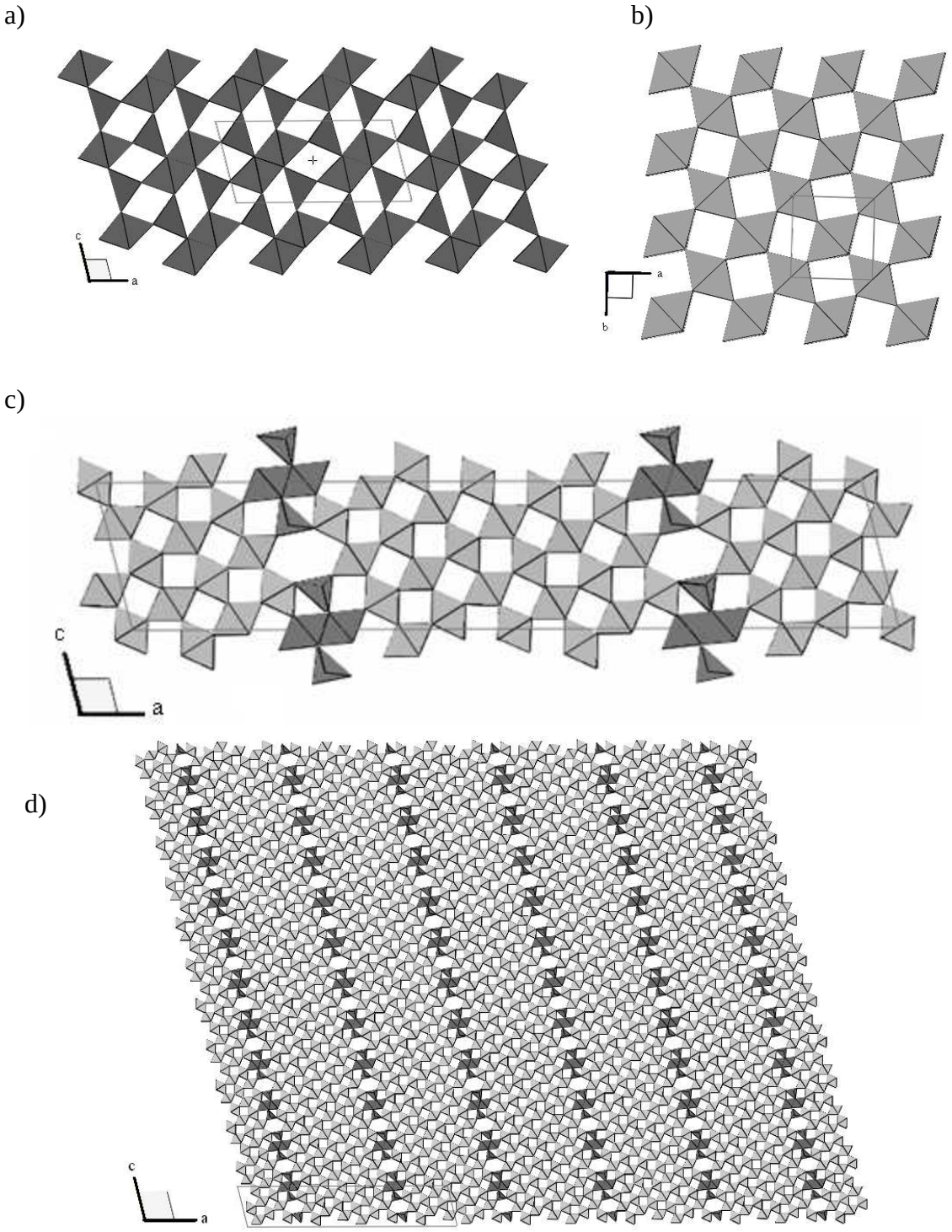

Figure 2.9. Polyhedral models of a) the (010) plane of beta-gallia. b) the (001) plane of rutile. c) The (010) plane of an n=25 BGR ($Ga_4Ti_{21}O_{48}$). Two dimensional projections of TiO_6 octahedra are shown in light grey. Projections of GaO_6 octahedra and GaO_4 tetrahedra are shown in dark grey. d) an expansion of (c).

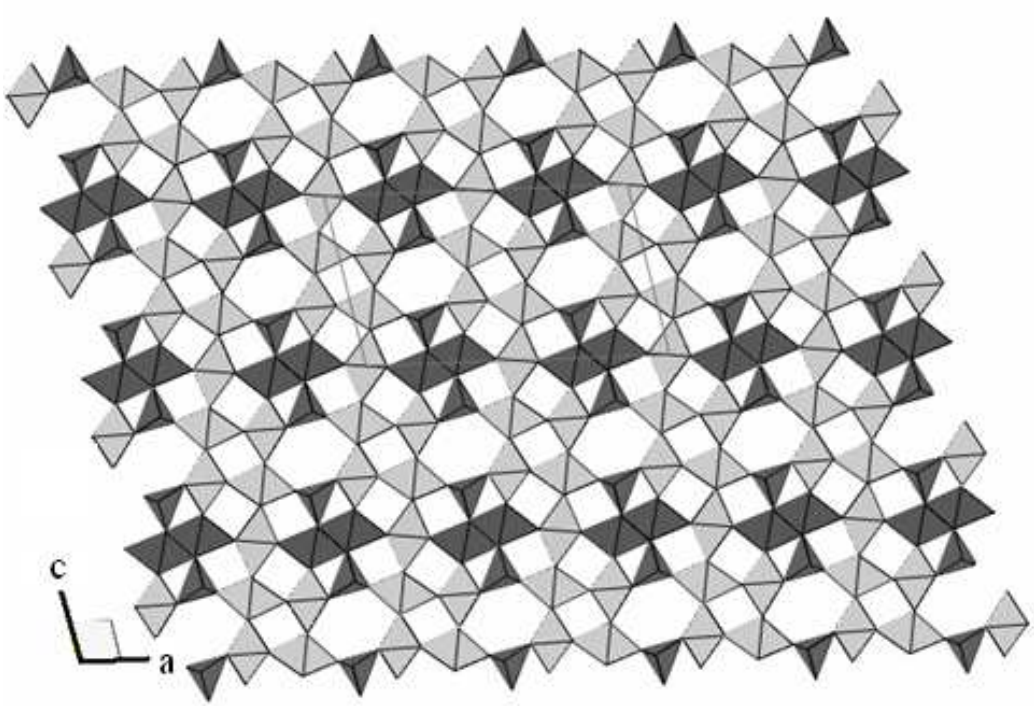

Figure 2.10. Polyhedral model of the (010) plane of an n=9 BGR ($Ga_4Ti_5O_{16}$). Two dimensional projections of TiO_6 octahedra are shown in light grey. Projections of GaO_6 octahedra and GaO_4 tetrahedra are shown in dark grey. Compared with n=25 BGR, the n=9 possesses a greater tunnel density.

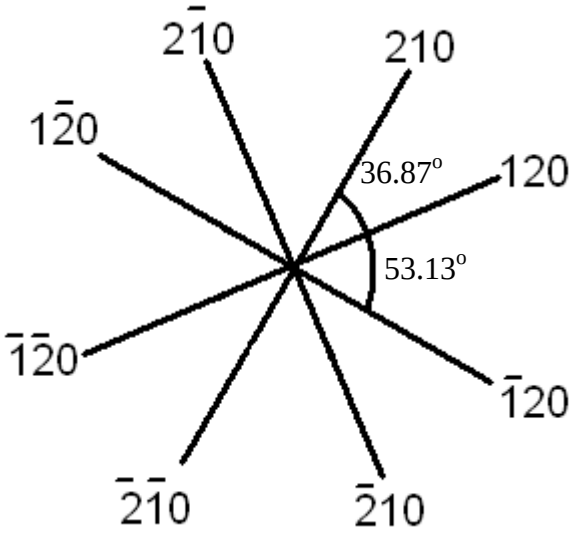

Figure 2.11. Diagram of BGR $\{210\}_r$ intergrowth boundary orientation

boundaries observed experimentally is believed to be due to the formation of a variety of n value BGR phases, attributed to the inhomogeous application of beta-gallia.[82]

The BGR tunnel site is approximately 0.25 nm in diameter, sufficient to accommodate small to medium-sized cations. The spacing between adjacent tunnel sites along $\{210\}_r$ directions is approximately 1 nm. The BGR material had been previously investigated for 1-D ion conduction applications, where tunnel density is of the utmost importance.[79,85,86] The phase stabilization of an n=5 BGR intergrowth was achieved via the incorporation of sodium cations at the tunnel site ($Na_{0.7}Ga_{4.7}Ti_{0.3}O_8$) which supports the hypothesis that cations will prefer to occupy the vacant tunnel sites of BGR structures.[85]

As described above, results obtained from DNA attachment to mica surfaces suggest divalent and / or multivalent cations are required for sufficient DNA adsorption. Studies of divalent cation insertion into BGR structures have not been previously conducted nor has the interaction between DNA and BGR surfaces. This current study will aid in identifying if the interaction of divalent cations with tunnel sites behaves similarly to the monovalent condition, and if the preferential incorporation of divalent cations at surface $\{210\}_r$ tunnel sites will in turn lead to the preferential attachment of DNA to $\{210\}_r$ regions of BGR surfaces.

2.4. References

1. J.D. Watson and F.H.C. Crick, "Molecular Structure of Nucleic Acids: A Structure for Deoxyribose Nucleic Acid," *Nature,* **171** [4356] 737-8 (1953).

2. D. Luo, "The Road from Biology to Materials," *Mater. Today,* **6** [11] 38-43 (2003).

3. C.M. Niemeyer, "Self-assembled Nanostructures Based on DNA: Towards the Development of Nanobiotechnology," *Cur. Opin. Chem. Biol.,* **4** [6] 609-18 (2000).

4. N.C. Seeman, "DNA Engineering and Its Application to Nanotechnology," *Trends in Biotechnology,* **17** [11] 437-43 (1999).

5. N.C. Seeman, "DNA Nanotechnology," *Materials Today,* **6** [1] 24-9 (2003).

6. R. Bashir, "Invited Review: DNA-mediated Artificial Nanobiostructures: State of the Art and Future Directions," *Superlattices and Microstruct.,* **29** [1] 1-16 (2001).

7. D.M. Hartmann, M. Heller, and S.C. Esener, "Selective DNA Attachment of Micro- and Nanoscale Particles to Substrates," *J. Mater. Res.,* **17** [2] 473-8 (2002).

8. N. Seeman, "Nanotechnology and the Double Helix," *Sci. Am.,* **290** [6] 65-75 (2004).

9. N. Seeman and A. Belcher, "Emulating Biology: Building Nanostructures from the Bottom up," *Proc. Natl. Acad. Sci. U.S.A.,* **99** [2] 6451-5 (2002).

10. N. Seeman, J. Rosenberg, and A. Rich, "Sequence-specific Recognition of Double Helical Nucleic Acids by Proteins," *Proc. Natl. Acad. Sci. U.S.A.,* **73** [3] 804-8 (1976).

11. N.C. Seeman, "The Design and Engineering of Nucleic Acid Nanoscale Assemblies," *Cur. Opin. Struc. Biol.*, **6** [4] 519-26 (1996).

12. M. Barbic, J. Mock, D. Smith, and S. Schultz, "Single Crystal Silver Nanowires Prepared by the Metal Amplificaiton Method," *J. Appl. Phys.,* **91** [11] 9341-5 (2002).

13. E. Braun, Y. Eichen, U. Sivan, and G. Ben-Yoseph, "DNA-templated Assembly and Electrode Attachment of a Conducting Silver Wire," *Nature,* **391** [6669] 775-7 (1998).

14. J. Richter, M. Mertig, W. Pompe, I. Monch, and H. Schackert, "Construction of Highly Conductive Nanowires on a DNA Template," *Appl. Phys. Lett.,* **78** [4] 536-8 (2001).

15. P. Aich, S.L. Labiuk, L.W. Tari, L.J.T. Delbaere, W.J. Roesler, K.J. Falk, R.P. Steer, and J.S. Lee, "M-DNA: A Complex Between Divalent Metal Ions and DNA which Behaves as a Molecular Wire," *J. Mol. Biol.,* **294** [2] 477-85 (1999).

16. A. Rakitin, P. Aich, C. Papadopoulos, Y. Kobzar, A.S. Vedeneev, J.S. Lee, and J.M. Xu, "Metallic Conduction Through Engineered DNA: DNA Nanoelectronic Building Blocks," *Phys. Rev. Lett.,* **86** [16] 3670-3 (2001).

17. S. Wettig, C. Li, Y. Long, H. Kraatz, and J. Lee, "M-DNA: A Self-assembling Molecular Wire for Nanoelectronics and Biosensing," *Anal. Sci.,* **19** [1] 23-6 (2003).

18. B. Yurke, A. Turberfield, A. Mills, F. Simmel, and J. Neumann, "A DNA-fueled molecular machine made of DNA," *Nature,* **406** [6796] 605-8 (2000).

19. P. Wagner, P. Kernen, M. Hegner, E. Ungewickell, and G. Semenza, "Covalent Anchoring of Proteins onto Gold-directed NHS-terminated Self-assembled Monolayers in Aqueous Buffers: SFM Images of Clathrin Cages and Triskelia.," *FEBS Lett.,* **356** [2-3] 267-71 (1994).

20. M. Hegner, P. Wagner, and G. Semenza, "Immobilizing DNA on Gold Via Thiol Modification for Atomic Force Micrscopy Imaging in Buffer Solutions," *FEBS,* **336** [3] 452-6 (1993).

21. P.V. Schwartz, "Meniscus Force Nanografting: Nanoscopic Patterning of DNA," *Langmuir,* **17** [19] 5971-7 (2001).

22. G.M. Whitesides and J.C. Love, "The Art of Building Small," *Sci. Am.,* **285** [3] 38-48 (2001).

23. G. Whitesides and M. Boncheva, "Beyond Molecules: Self-assembly of Mesoscopic and Macroscopic Components," *Proc. Natl. Acad. Sci. U.S.A.,* **99** [8] 4769-74 (2002).

24. X. Zhao, Y. Xia, and G. Whitesides, "Soft Lithographic Methods for Nano-fabrication," *J. Mater. Chem.,* **7** [7] 1069-74 (1997).

25. B. Gates, Q. Xu, C. Love, D. Wolfe, and G. Whitesides, "Unconventional Nanofabrication," *Annu. Rev. Mater. Res.,* **34** 339-72 (2004).

26. H. Jiang and S. Stupp, "Dip-pen Patterning and Surface Assembly of Peptide Amphiphiles," *Langmuir,* **21** [12] 5242-6 (2005).

27. L.M. Demers, D.S. Ginger, S.J. Park, Z. Li, S.W. Chung, and C.A. Mirkin, "Direct Patterning of Modified Oligonucleotides on Metals and Insulators by Dip-pen Nanolithography," *Science,* **296** [5574] 1836 (2002).

28. G.Y. Liu and N.A. Amro, "Positioning Protein Molecules on Surfaces: A Nanoengineering Approach to Supramolecular Chemistry," *Proc. Natl. Acad. Sci. U.S.A.,* **99** [8] 5165-70 (2002).

29. H. Kim, N. Moldovan, and H. Espinosa, "A Nanofountain Probe with Sub-100nm Molecular Writing Resolution," *Small,* **1** [6] 632-5 (2005).

30. G. Binnig and C.F. Quate, "Atomic Force Microscope," *Phys. Rev. Lett.,* **56** [9] 930-3 (1986).

31. D.J. Muller, M. Amrein, and A. Engel, "Adsorption of Biological Molecules to a Solid Support for Scanning Probe Microscopy," *J. Struct. Biol.*, **119** [2] 172-88 (1997).

32. P.C. Rankin and A.T. Wilson, "The Surface Chemistry of the Mica-aluminum-sulfate System," *J. Colloid Interface Sci.*, **30** [3] 277-82 (1969).

33. E.W. Radoslovich, "The Structure of Muscovite, $KAl_2(Si_3Al)O_{10}(OH)_2$," *Acta Cryst.*, **13** [11] 919-32 (1960).

34. W.A. Deer, R.A. Howie, and J. Zussman, *Rock Forming Minerals*. London, 1962.

35. P. Samori, S. Pieraccini, S. Masiero, G.P. Spada, G. Gottarelli, and J.P. Rabe, "Controlling the Self-assembly of a Deoxiguaninosine on Mica," *Colloids Surf., B*, **23** [4] 283-8 (2002).

36. C.N. Gordon and A.K. Kleinschmidt, "Electron Microscopic Observation of DNA Adsorbed on Aluminum-mica," *J. Colloid Interface Sci.*, **34** [1] 131-41 (1970).

37. J. Zheng, Z. Li, A. Wu, and H. Zhou, "AFM Studies of DNA Structures on Mica in the Presence of Alkaline Earth Metal Ions," *Biophys. Chem.*, **104** [1] 37-43 (2003).

38. W. Wang, J. Lin, and D. Schwartz, "Scanning Force Microscopy of DNA Molecules Elongated by Convective Fluid Flow in an Evaporating Droplet," *Biophys. J.*, **75** [1] 513-20 (1998).

39. R.M. Pashley, "DLVO and Hydration Forces between Mica Surfaces in Li+, Na+, K+, and Cs+ Electrolyte Solutions: A Correlation of Double-layer and Hydration Forces with Surface Cation Exchange Properties," *J. Colloid Interface Sci.*, **83** [2] 531-46 (1981).

40. M.A. Osman, C. Moor, W.R. Caseri, and U.W. Suter, "Alkali Metals Ion Exchange on Muscovite Mica," *J. Colloid Interface Sci.*, **209** [1] 232-9 (1999).

41. S. Nishimura, P.J. Scales, T. Tateyama, K. Tsunematsu, and T.W. Healy, "Cationic Modification of Muscovite Mica: An Electrokinetic Study," *Langmuir*, **11** [1] 291-5 (1995).

42. L.T. Costa, J.R. Pinto, M.B. Moraes, G.G.B. de Souza, M.M. Sorenson, P.M. Bisch, and G. Weissmuller, "Chemical Treatment of Mica for Atomic Force Microscopy Can Affect Biological Sample Conformation," *Biophys. Chem.*, **109** [1] 63-71 (2004).

43. M. Bezanilla, C. Bustamante, and H.G. Hansma, "Improved Visualization of DNA in Aqueous Buffer with the Atomic Force Microscope.," *Scanning Microsc.,* **7** [4] 1145-8 (1993).

44. M. Bezanilla, S. Manne, D. Laney, Y. Lyubchenko, and H. Hansma, "Adsorption of DNA to Mica, Silylated Mica and Minerals: Characterization by Atomic Force Microscopy," *Langmuir,* **11** [2] 655-9 (1995).

45. C. Bustamante, J. Vesenka, C. Tang, W. Rees, M. Guthold, and R. Keller, "Circular DNA Molecules Imaged in Air by Scanning Force Microscopy," *Biochemistry,* **31** [1] 33-26 (1992).

46. H. Hansma, M. Benzanilla, F. Zanhausern, M. Adrian, and R. Sinsheimer, "Atomic Force Microscopy of DNA in Aqueous Solutions," *Nucleic Acids Res.,* **21** [3] 505-12 (1993).

47. H. Hansma, L. Sinsheimer, M. Li, and P. Hansma, "Atomic Force Microscopy of Single- and Double-stranded DNA," *Nucleic Acids Res.,* **20** [14] 3585-90 (1992).

48. H.G. Hansma and D.E. Laney, "DNA Binding to Mica Correlates with Cationic Radius: Assay by Atomic Force Microscopy," *Biophys. J.,* **70** [4] 1933-9 (1996).

49. T. Thundat, D.P. Allison, R.J. Warmack, G.M. Brown, K.B. Jacobson, J.J. Schrick, and T.L. Ferrell, "Atomic Force Micrsocopy of DNA on Mica and Chemically Modified Mica," *Scanning Microsc.,* **6** [4] 911-8 (1992).

50. Y. Fang, T.S. Spisz, T. Wiltshire, N.P. D'Costa, I.N. Bankman, R.H. Reeves, and J.H. Hoh, "Solid-state DNA Sizing by Atomic Force Microscopy," *Anal. Chem.,* **70** [10] 2123-9 (1998).

51. D. Pastre, O. Pietrement, S. Fusil, F. Landousy, J. Jeusset, M. David, L. Hamon, E. Cam, and A. Zozime, "Adsorption of DNA to Mica Mediated by Divalent Counterions: A Theoretical and Experimental Study," *Biophys. J.,* **85** [4] 2507-18 (2003).

52. O. Pietrement, D. Pastre, F. Stephane, J. Jeusset, M. David, F. Landousy, L. Hamon, A. Zozime, and E. Le Cam, "Reversible Binding of DNA on $NiCl_2$-treated Mica by Varying the Ionic Strength," *Langmuir,* **19** [6] 2536-9 (2003).

53. N.H. Thomson, S. Kasas, B.L. Smith, H.G. Hansma, and P.K. Hansma, "Reversible Binding of DNA to Mica for AFM Imaging," *Langmuir,* **12** [24] 5905-8 (1996).

54. S.J.T. van Noort, K.O. van der Werf, A.P.M. Eker, C. Wyman, B.G. de Grooth, N.F. van Hulst, and J. Greve, "Direct Visualization of Dynamic Protein-DNA

Interactions with a Dedicated Atomic Force Microscope," *Biophys. J.,* **74** [6] 2840-9 (1998).

55. D. Allison, L. Bottomley, T. Thundat, G. Brown, R. Woychik, J. Schrick, K. Jacobson, and R. Warmack, "Immobilization of DNA for Scanning Probe Microscopy," *Proc. Natl. Acad. Sci. U.S.A.,* **89** [21] 10129-33 (1992).

56. M. Bezanilla, B. Drake, E. Nudler, M. Kashlev, P. Hansma, and H. Hansma, "Motion of Enzymatic Degradation of DNA in the Atomic Force Microscope," *Biophys. J.,* **67** [6] 2454-9 (1994).

57. H. Hansma, J. Vesenka, C. Siergerist, G. Kelderman, H. Morrett, R. Sinsheimer, V. Elings, C. Bustamante, and P. Hansma, "Reproducible Imaging and Dissection of Plasmid DNA Under Liquid with the Atomic Force Microscope.," *Science,* **256** [5060] 1180-4 (1992).

58. T. Thundat, D. Allison, R. Warmack, and T. Ferrell, "Imaging Isolated Strands of DNA Molecules by Atomic Force Microscopy," *Ultramicroscopy,* **42-44** [2] 1101-6 (1992).

59. J. Vesenka, M. Guthold, C.L. Tang, D. Keller, E. Delaine, and C. Bustamante, "Substrate Preparation for Reliable Imaging of DNA Molecules with the Scanning Force Microscope," *Ultramicroscopy,* **42-44** [2] 1243-9 (1992).

60. C. Bustamante and D. Keller, "Scanning Force Micrcoscopy in Biology," *Phys. Today,* **48** [12] 32-8 (1995).

61. H. Cheng, K. Zhang, J. Libera, M. Olvera de la Cruz, and M. Bedzyk, "Polynucleotide Adsorption to Negatively Charged Surfaces in Divalent Salt Solutions," *Biophys. J.,* **90** [4] 1164-74 (2006).

62. T. Thundat, R.J. Warmack, D.P. Allison, L.A. Bottomley, A.J. Lourenco, and T.L. Ferrell, "Atomic Force Microscopy of Deoxyribonucleic Acid Strands Adsorbed on Mica: The Effects of Humiditiy on Apparent Width and Image Contrast," *J. Vac. Sci. Technol. A,* **10** [4] 630-5 (1992).

63. R. Izatt, J. Christensen, and J. Rytting, "Sites and Thermodynamic Quantities Associated with Proton and Metal Ion Interaction with Ribonucleic Acid, Deoxyribonucleic Acid, and Their Constituent Bases, Nucleosides, and Nucleotides," *Chem. Rev.,* **71** [5] 439-81 (1971).

64. G.L. Eichhorn and Y.A. Shin, "Interaction of Metal Ions with Polynucleotides and Related Compounds. XII. The Relative Effect of Various Metal Ions on DNA Helicity," *J. Am. Chem. Soc.,* **90** [26] 7323-8 (1968).

65. C. Rivetti, M. Guthold, and C. Bustamante, "Scanning Force Microscopy of DNA Deposited onto Mica: Equilibration Versus Kinetic Trapping Studied by Statistical Polymer Chain Analysis," *J. Mol. Biol.,* **264** [5] 919-32 (1996).

66. V. Stein, J. Bond, M. Capp, C. Anderson, and M. Anderson Jr, "Importance of Coulombic End Effects on Cation Accumulation Near Oligonucleotide B-DNA Using Na NMR," *Biophys. J.,* **68** [3] 1063-71 (1995).

67. J.F. Allemand, D. Bensimon, L. Jullien, A. Bensimon, and V. Croquette, "pH-dependent Specific Binding and Combing of DNA," *Biophys. J.,* **73** [4] 2064-70 (1997).

68. A. Bensimon, A. Simon, A. Chiffaudel, V. Croquette, F. Heslot, and D. Bensimon, "Alignment and Sensitive Detection of DNA by Moving Interface," *Science,* **265** [5181] 2096-8 (1994).

69. D. Bensimon, J. Simon, V. Croquette, and A. Bensimon, "Stretching DNA with a Receding Meniscus: Experiments and Models," *Phys. Rev. Lett.,* **74** [23] 4754-7 (1995).

70. S. Karrasch, M. Dolder, F. Schabert, J. Ramsden, and A. Engel, "Covalent Binding of Biological Samples to Solid Supports for Scanning Probe Microscopy in Buffer Solution," *Biophys. J.,* **65** [6] 2437-46 (1993).

71. D. Klein, L. Gurevich, J. Janssen, L. Kouwenhoven, J. Carbeck, and L. Sohn, "Ordered Stretching of Single Molecules of Deoxyribose Nucleic Acid Between Microfabricated Polystyrene Lines," *Appl. Phys. Lett.,* **78** [16] 2396-8 (2001).

72. J. Li, C. Bai, C. Wang, C. Zhu, Z. Lin, Q. Li, and E. Cao, "A Convenient Method of Aligning Large DNA Molecules on Bare Mica Surfaces for Atomic Force Microscopy," *Nucleic Acids Res.,* **26** [20] 4785-6 (1998).

73. K. Otobe and T. Ohtani, "Behavior of DNA Fibers Streched by Precise Meniscus Motion Control," *Nucleic Acids Res.,* **29** [22] 1-6 (2001).

74. M. Sasou, S. Sugiyama, T. Yoshino, and T. Ohtani, "Molecular Flat Mica Surface Silanized with Methyltrimethoxysilane for Fixing and Straightening DNA.," *Langmuir,* **19** [23] 9845-9 (2003).

75. H. Yokota, H. Johnson, R. Robinson, A. Belu, M. Garrison, B. Ratner, B. Trask, and D. Miller, "A New Method for Straightening DNA Molecules for Optical Restriction Mapping," *Nucleic Acids Res.,* **25** [5] 1064-70 (1997).

76. L.A. Bursill and G.G. Stone, "Tunnel and Intergrowth Structures in the Gallia-rich Gallium Titanate System," *J. Solid State Chem.,* **38** [2] 149-57 (1981).

77. A. Kahn, V. Agafonov, D. Michel, and M. Perez Y Jorba, "New Gallium Germanates with Tunnel Structures: alpha-Ga_4GeO_8 and $Ga_4Ge_3O_{12}$," *J. Solid State Chem.,* **65** [3] 377-82 (1986).

78. S. Kamiya and R.J.D. Tilley, "Phase Relations in the Pseudobinary System TiO_2-Ga_2O_3," *J. Solid State Chem.,* **22** [2] 205-16 (1977).

79. D.D. Edwards, T.O. Mason, W. Sinkler, L.D. Marks, K.R. Poeppelmeier, Z. Hu, and J.D. Jorgensen, "Tunneled Intergrowth Structures in the Ga_2O_3-In_2O_3-SnO_2 System," *J. Solid State Chem.,* **150** [2] 294-304 (2000).

80. A. Lejus, D. Goldberg, and A. Revcolevschi, "New Compounds Formed from Rutile, TiO_2, and Oxides of Trivalent and Tetravalent Metals," *C.R. Seances Acad. Sci., Ser. C.,* **263C** [20] 1223-6 (1966).

81. R.M. Gibb and J.S. Anderson, "Electron Microscopy of Solid Solutions and Crystallographic Shear Structures II. Fe_2O_3-TiO_2 and Ga_2O_3-TiO_2 Systems," *J. Solid State Chem.,* **5** [2] 212-25 (1972).

82. L.A. Bursill, "Intersecting Defect Structures in Gallia- and Magnesia-doped Rutiles," *Acta Cyst.,* **A 35** [3] 449-58 (1979).

83. D.J. Lloyd, I.E. Grey, and L.A. Bursill, "The Structure of $Ga_4Ti_{21}O_{48}$," *Acta Cryst.,* **B32** [6] 1756-61 (1976).

84. M. Pilliod, "Preferentially Aligning DNA Molecules on the Treated Surfaces of a Single Crystal TiO_2 (001)"; B.S. Thesis. Alfred University, Alfred, NY, 2001.

85. G.V. Chandrashekar, A. Bednowitz, and S.J. La Placa, "A One Dimensional Sodium Ion Conductor," pp. 447-50 in *Fast Ion Transport in Solids.* Edited by P. Vashishta, J. N. Mundy, and G. K. Shenoy. Elsevier North-Holland, New York, 1979.

86. D.D. Edwards and T.O. Mason, "Subsolidus Phase Relations in the Ga_2O_3-In_2O_3-SnO_2 System," *J. Am. Ceram. Soc.,* **81** [12] 3285-91 (1998).

3. Phase Stability and Structure of Alkali Doped Beta-Gallia Rutile Intergrowths

Abstract

The incorporation of alkali cations into the tunneled structure of Ga_4TiO_8 (n=5) was investigated and compared to predictions based on atomistic computer simulations. Samples were prepared as $A_xGa_{4+x}Ti_{1-x}O_8$, A= Li, Na, and K, $x \leq 0.7$, and as $Na_yGa_{4+y}Ti_{2-y}O_{10}$ (y = 0.7, 0.85, 1.0) using solid-state reactions at 1050 – 1350^oC. The sodium-incorporated n=5 intergrowth formed via solid-state reaction, but the potassium and lithium analogs formed mixed-phase assemblages, which are discussed in reference to compatibility triangles in the Li_2O-Ga_2O_3-TiO_2 and K_2O-Ga_2O_3-TiO_2 systems. Experimental results were compared to the results of energy minimization calculations using the General Utility Lattice Program (GULP). For the lithium-containing system, the computer simulations correctly predicted the formation of a mixed-phase assemblage containing $LiGa_5O_8$, Ga_2O_3, and TiO_2. For the sodium- and potassium-containing system, the computer simulations indicated that mixtures of the single-cation oxide components are preferred. Energy minimization calculations conducted on structurally different $Na_xGa_{4+x}Ti_{2-x}O_{10}$ and $Na_xGa_{4+x}Ti_{3-x}O_{12}$ phases indicated that n = 6 and n = 7 ß-gallia rutile intergrowth structures have lower lattice energies than the experimentally observed structures reported previously in literature.

3.1. Introduction

The sodium-ion conductor with a reported composition of $Na_{0.7}Ga_{4.72}Ti_{0.29}O_8$ (Figure 3.1b) is structurally related to Ga_4TiO_8 (Figure 3.1a), the metastable n = 5 member of a beta-gallia rutile (BGR) intergrowth series. The relationship between $Na_{0.7}Ga_{4.72}Ti_{0.29}O_8$ and Ga_4TiO_8 is more apparent when the composition of the former is expressed as $Na_xGa_{4+x}Ti_{1-x}O_8$, $x \cong 0.7$. In the derived structure, trivalent gallium cations

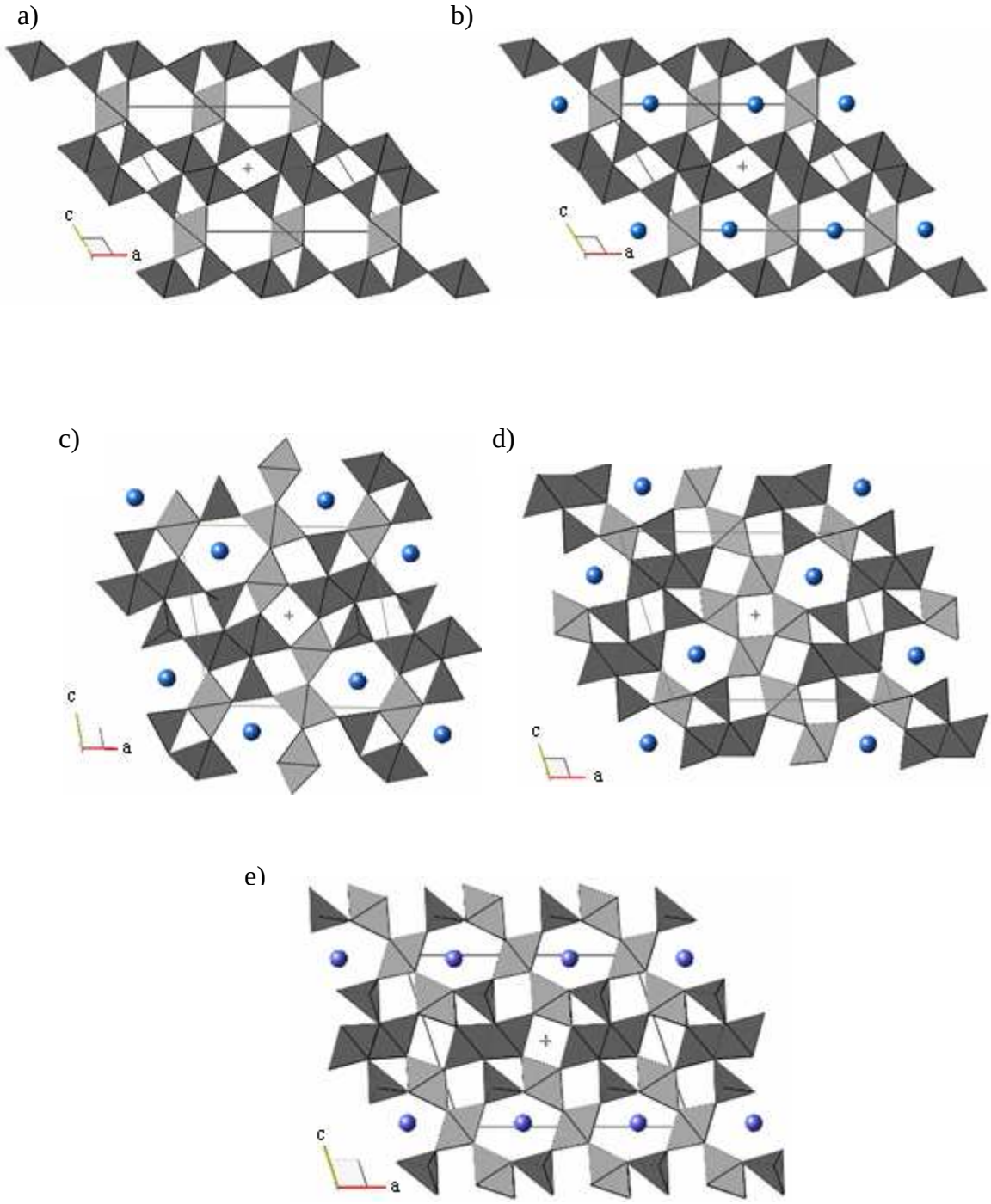

Figure 3.1. B-axis projection of BGR-derived $A_xGa_{4+x}Ti_{n-4-x}O_{2n-2}$ structures: a) BGR n=5 intergrowth structure, b) $Na_{0.7}Ga_{4.72}Ti_{0.29}O_8$ structure,[2] c) BGR n=6 intergrowth structure, d) BGR n=7 structure (P 2/m), and e) BGR n=7 structure (C 2/m).

replace tetravalent titanium cations in the host structure and sodium ions reside in the one-dimensional tunnels that serve as pathways for conduction.

BGR intergrowths, expressed generically as $Ga_4M_{n-4}O_{2n-2}$, $n \geq 5$, result from the coherent intergrowth of beta-gallia (β-Ga_2O_3) and oxides possessing the rutile structure (MO_2), in such a manner that b_{gallia} is parallel to c_{rutile}. The resulting homologous structures are monoclinic (C2/m or P2/m) and possess hexagonal-cross-sectioned tunnels lying parallel to the unique b-axis. Two distinct BGR intergrowth series are known to form – a C2/m series which includes members with $n \geq 5$ (odd) and a P2/m series which includes members with $n \geq 6$ (even and odd).[1] With increasing n in either BGR series, the tunnel density decreases, but the size and shape of the tunnels remains largely unchanged suggesting that it should be possible to form a series of sodium-ion conductors based on the BGR intergrowths, e.g. $Na_xGa_{4+x}Ti_{2-x}O_{10}$ and $Na_xGa_{4+x}Ti_{3-x}O_{12}$ for the n = 6 and n = 7 intergrowths, respectively (Figure 3.1c-e). A comparison of ionic size to tunnel diameter suggests that it should be possible to form Li and K analogs of the proposed Na-based materials.

The sodium-substituted BGR intergrowth $Na_xGa_{4+x}Ti_{1-x}O_8$ is just one of many alkali gallium titanium oxides that possess one-dimensional tunnels that serve as pathways for alkali-ion conduction. As summarized in Table 3.I, these oxides have a variety of different crystal structures with different sized and shaped tunnels that can accommodate a range of alkali ions.[2-9] Of particular interest to the current study are two structures that possess tunnels with a distorted octagonal cross section, i.e. $A_xGa_{4+x}Ti_{2-x}O_{10}$ and $A_xGa_{4+x}Ti_{3-x}O_{12}$ (Figure 3.2) where A represents an alkali cation. While these materials have the same compositions as the proposed conductors based on the n = 6 and n = 7 BGR intergrowths, their structures are considerably different, as can be seen by comparing Figure 3.1c-e to Figure 3.2.

This paper describes our attempts to prepare a series of alkali-substituted BGR intergrowths using solid-state reaction techniques. With the exception of compositions expressed as $Na_xGa_{4+x}Ti_{1-x}O_8$, the desired materials were not obtained. Instead, a variety of mixed-phase assemblages were observed. This paper also discusses the results of lattice-energy calculations of metastable Ga_4TiO_8, the proposed alkali-substituted BGR

Table 3.I. Known Alkali Gallium Titanium Oxide Phases with One-dimensional Tunnels

Composition	A	x	Structure	Tunnel Cross-section	Reference
$A_xGa_{4+x}Ti_{1-x}O_8$	Na	≤ 0.7	P2/m or C2/m	Hexagonal	[2]
$A_xGa_{2+x}Ti_{2-x}O_7$	K	≤ 0.25	I4/m	Octagonal	[9]
$A_xGa_{4+x}Ti_{2-x}O_{10}$	Na	~0.8	C2/m	Distorted Octagonal	[5]
$A_xGa_{4+x}Ti_{3-x}O_{12}$	Na,K	~0.8	Pbam	Distorted Octagonal	[4,8]
$A_xGa_xTi_{4-x}O_8$	Na	~0.8	C2/m	1x1	[6]
$A_xGa_xTi_{8-x}O_{16}$	K		I4/m	2x2	[7]
$A_xGa_{16+x}Ti_{16-x}O_{56}$	K,Rb,Cs	≤ 2.0	I4/m	Octagonal	[3]

a) b)

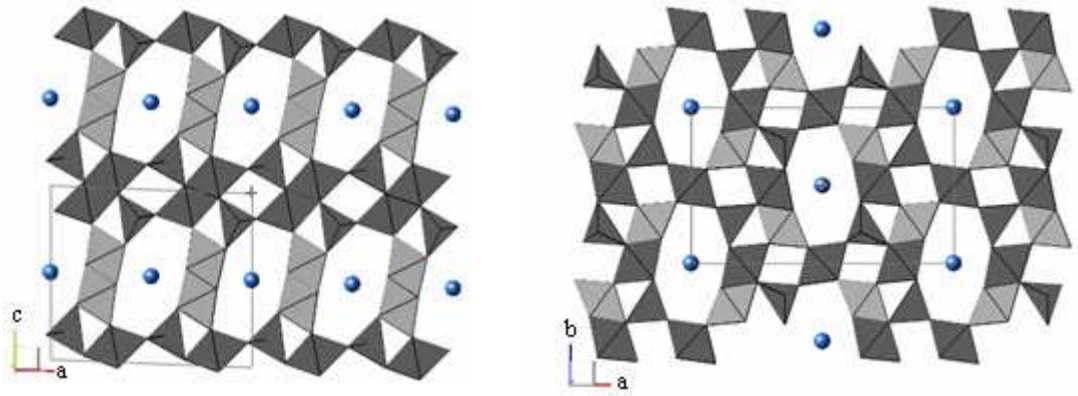

Figure 3.2. B-axis projection of reported $A_xGa_{4+x}Ti_{n-4-x}O_{2n-2}$ structures a) n=6, C2/m structure.[5] b) n=7, Pbam structure.[4]

materials, the alternative $A_xGa_{4+x}Ti_{n-4-x}O_{2n-2}$ structures (Figure 3.2), and other oxides observed in our experimental investigations.

3.2. Experimental Methods

Alkali carbonate (A_2CO_3), gallium (III) oxide (Sigma Aldrich 99.999+%), and titanium (IV) oxide (Fisher Scientific 99.8%) powders were mixed in proportions to obtain $A_xGa_{4+x}Ti_{1-x}O_8$ (x = 0.1, 0.3, 0.5, 0.7, A = Li, Na, K) and $Na_yGa_{4+y}Ti_{2-y}O_{10}$ (y = 0.7, 0.85, 1.0). Starting materials were dried overnight at 600°C. Appropriate amounts were mixed in a mortar. The powder samples were pressed (~50 MPa) into pellets and fired for 24 to 264 hours at 1000°C to 1350°C with quenching in dry air. The pellets were sandwiched between sacrificial pellets of the same composition when fired. Fired samples were crushed and ground in a mortar. The powders were mounted on a zero-background holder and analyzed by X-ray diffraction with CuKα radiation using a Phillips 3100 x-ray generator (40kV, 30mA). Diffraction patterns were collected over 10-70° 2Θ, 0.05° step-size, and a 2 second dwell. The collected patterns were used for phase identification.

3.3. Simulation Methods

Computer simulations were conducted with the General Utility Lattice Program (GULP).[10] All computer simulations were conducted on a SGI O2 workstation (MPS R10000, 256 MB).

The lattice energy of various crystal-structure models was minimized with respect to structural parameters, first under constant volume conditions, then under constant pressure conditions. The lattice energy was calculated as the summation of long and short-range potentials, according to a reduced Born model:

$$E_{latt} = \frac{1}{2}\sum \frac{q_i q_j}{r_{ij}} + V(r_{ij}) \qquad (1)$$

The first term in Eq. 1 is the sum of the Coulombic interactions (long-range) between pairs of ions "i" and "j"; where q is the charge of each ion, and r_{ij} is the distance separating the two ions. The summation of $V(r_{ij})$ represents the contribution of ion pair short-range interactions within the lattice. For ionic crystals, the short-range potential is adequately modeled with the pair interaction term $V(r_{ij})$ described as the Buckingham potential:

$$V_{ij}(r_{ij}) = A_{ij} \exp(\frac{-r_{ij}}{\rho_{ij}}) - \frac{C_{ij}}{r_{ij}^{6}} \qquad (2)$$

where A, ρ (range of repulsion interaction), and C (associated with the attraction interaction) are potential parameters.[11]

The intergrowth phases all contain a ß-Ga_2O_3 sub-structure; so separate potential parameters were developed for Ga^{3+} in octahedral and tetrahedral coordination from a potential fit of ß-Ga_2O_3. The space group and atomic positions for ß-Ga_2O_3 were obtained from Ahman *et al.*[12] Values for interatomic distances of Ga-O in tetrahedral and octahedral coordination (for ß-Ga_2O_3) were taken from Kahn.[13] Potential parameters for Ti-O and Na-O were developed by fitting to both the $Na_{0.7}Ga_{4.72}$ $Ti_{0.29}O_8$ structure described by Chandrashekar *et al.* and the Ga_2TiO_5 structure described by Mueller-Buschbaum and Freund.[2,14] Oxygen core-shell potential parameters were gathered from Theobald *et al.*[15] Table 3.II summarizes the potential parameters that were used in this study. The collected potentials were then applied to energy minimization simulations of the intergrowth compounds to obtain relaxed structures and associated lattice energies for the various intergrowth phases. Bond valence sum (BVS) analysis[16] was incorporated to ensure that the potentials being used generated structures with reasonable bond distances. The structures obtained via simulation were within 1% of published lattice volumes of experimentally observed structures.[2,13]

Minimized lattice energies of mixed phase assemblages and intergrowths were calculated and compared to explain the results collected from the synthesis study. The results from X-ray diffraction experiments were used to identify appropriate alternatives to the intergrowth species. Atomic parameters for phases in mixed phase assemblages were obtained from literature.[5,8,9,12,17-21]

Table 3.II Potential Parameters used in this Study.

Interaction	A (eV)	ρ (Å)	C (eV Å^{-6})	Comment
Ga (oct) – O	1542.00	0.3065	0.0	Developed in this study
Ga (tet) – O	1417.25	0.3099	0.0	Developed in this study
O – O	22764.30	0.149	27.063	From reference [15]
Ti – O	765.20	0.38096	0.0	Developed in this study
Li – O	908.30	0.2992	0.0	Developed in this study
Na – O	1226.80	0.3055	0.0	Developed in this study
K – O	1518.50	0.3218	0.0	Developed in this study

Energy minimization calculations were conducted for differing n=6 and n=7 structures (Figure 3.1 c-e, and Figure 3.2). Starting lattice parameters and atomic positions were taken from literature.[4,5,13,22] Minimized lattice energies, as well as initial and final atomic positions and lattice parameters, were compared for each compositionally equivalent structure to predict the preferred phase. BVS analysis was used to assess the suitability of the potential parameters in these structures.

3.4. Results and Discussion

3.4.1. Phase analysis

The phase analyses of samples prepared as $A_xGa_{4+x}Ti_{1-x}O_8$ are summarized in Table 3.III. X-ray diffraction experiments revealed that Na was the only alkali species to form an $A_xGa_{4+x}Ti_{1-x}O_8$ intergrowth; however, the samples were not phase pure, but rather a mixture of intergrowth, TiO_2, and β-Ga_2O_3. Compositions prepared as $Li_xGa_{4+x}Ti_{1-x}O_8$ and heat-treated at 1100°C to 1350°C failed to yield any intergrowth phases, instead yielding a mixture of Ga_5LiO_8, Ga_2O_3, and TiO_2. Compositions prepared as $K_xGa_{4+x}Ti_{1-x}O_8$ and heat-treated at 1100°C to 1350°C yielded a number of potassium-gallate and potassium-titano-gallate phases in addition to Ga_2O_3, and TiO_2.

For the $Na_yGa_{4+y}Ti_{2-y}O_{10}$ compositions (y = 0.7, 0.85, 1.0), shown in Table 3.IV, no phase-pure samples were obtained. Most of the prepared samples contained $Na_{0.7}Ga_{4.7}Ti_{0.3}O_8$ and TiO_2. Samples prepared with y=0.85 and y=1.0 at temperatures between 1150°C and 1250°C contained a phase with a structure similar to that reported by Michiue *et al.* for $Na_{0.8}Ga_{4.8}Ti_{2.2}O_{10}$.[5]

In Figure 3.3, the prepared $A_xGa_{4+x}Ti_{1-x}O_8$ and $Na_yGa_{4+y}Ti_{2-y}O_{10}$ compositions are shown in reference to the compatibility triangles formed by the observed phases. As shown in Figure 3.3a, the $Li_xGa_{4+x}Ti_{1-x}O_8$ samples lie within the Ga_5LiO_8-Ga_2O_3-TiO_2 compatibility triangle over the temperature range 1100 –1350°C.

The $Na_xGa_{4+x}Ti_{1-x}O_8$ and $Na_yGa_{4+y}Ti_{2-y}O_{10}$ samples lie in different compatibility triangles depending on composition and temperature. Over the temperature range

Table 3.III. Phase Analyses of Samples Prepared as $A_xGa_{4+x}Ti_{1-x}O_8$.

Composition	x	Temperature (^oC)	Time (hrs)	Phases Observed
$Li_xGa_{4+x}Ti_{1-x}O_8$	0.1	1100	96	G, GL, T
	0.1	1200	148	G, GL, T
	0.1	1350	24	G, GL, T
	0.3	1100	96	G, GL, T
	0.3	1200	148	G, GL, T
	0.5	1100	96	G, GL, T
	0.5	1200	148	G, GL, T
	0.5	1350	24	G, GL, T
	0.7	1100	96	G, GL, T
	0.7	1200	148	G, GL, T
	0.7	1350	24	G, GL, T
$Na_xGa_{4+x}Ti_{1-x}O_8$	0.1	1000	96	N5, G, T
	0.1	1100	100	N5, G, T
	0.1	1200	100	N5, G, T
	0.1	1350	120	N5, G, T
	0.3	1000	96	N5, G, T
	0.3	1100	100	N5, G, T
	0.3	1200	100	N5, G, T
	0.3	1350	120	N5, G, T
	0.5	1000	96	N5, G, T
	0.5	1100	100	N5, G, T
	0.5	1200	100	N5, G, T
	0.5	1350	120	N5, G, T
	0.7	1000	96	N5, G
	0.7	1100	100	N5, G^*
	0.7	1200	100	N5, G
	0.7	1350	120	N5, G
	0.9	1000	65	N5, G, N
	0.9	1100	72	N5, G, N
	0.9	1200	120	N5, G, N
$K_xGa_{4+x}Ti_{1-x}O_8$	0.1	1100	96	K7, G, T
	0.1	1200	76	K7, G, T
	0.1	1350	120	KGT, G, KG
	0.3	1100	96	KG, K7, G
	0.3	1200	76	KG, K7, G
	0.3	1350	120	KGT, G, KG
	0.5	1100	96	KG, K7, G
	0.5	1200	76	KG, K7, G
	0.5	1350	120	KGT, G, KG
	0.7	1100	96	KG, T, K
	0.7	1200	76	KG, K7, G
	0.7	1350	120	KGT, G, KG

Key: G = Ga_2O_3 [12], G^* = trace amounts of Ga_2O_3 [12], GL = Ga_5LiO_8 [18], T = TiO_2 [19], N5 = $Na_{0.7}Ga_{4.7}Ti_{0.3}O_8$ (BGR), N = Na_2O [21] K7 = $K_{0.8}Ga_{4.8}Ti_{2.2}O_{12}$ (Watanabe)[8], KG = $K_{2.56}Ga_{22}O_{34.28}$[17], KGT = $K_{0.14}Ga_{2.14}Ti_{1.86}O_7$ [9], K = K_2O [20].

Table 3.IV. Phase Analyses of Samples Prepared as $Na_yGa_{4+y}Ti_{2-y}O_{10}$

y	Temperature (^oC)	Time (hrs)	Phases Observed
0.7	1000	72	N5, T, G
0.7	1050	36	N5, T
0.7	1150	20	N5, T
0.7	1200	20	N5, T
0.7	1250	20	N5, T
0.7	1300	20	N5, T
0.85	1000	72	N5, T
0.85	1050	36	N5, T
0.85	1150	20	N6, N5, T
0.85	1200	20	N6, N5, T
0.85	1250	20	N6, N5, T
0.85	1300	20	N5, T
1.0	1000	72	N5, T
1.0	1050	36	N5, T
1.0	1150	20	N5, T, N6
1.0	1200	20	N5, T, N6
1.0	1250	20	N5, T
1.0	1300	20	N5, T

Key: G = Ga_2O_3 [12], T = TiO_2 [19], N5 = $Na_{0.7}Ga_{4.7}Ti_{0.3}O_8$ (BGR), N6 = $Na_{0.8}Ga_{4.8}Ti_{2.2}O_{10}$ [5]

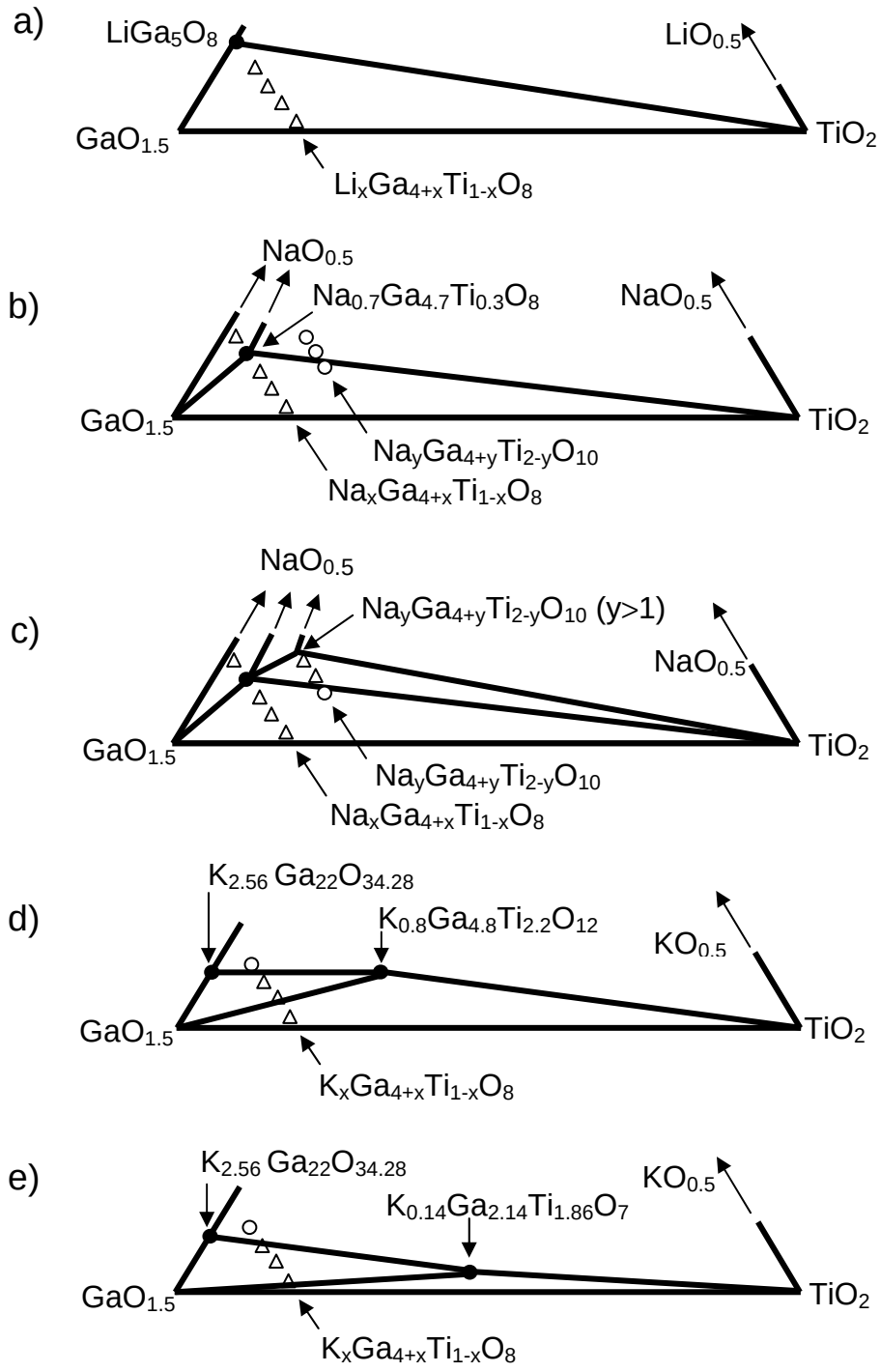

Figure 3.3. Prepared compositions in relationship to compatibility triangles in: a) the Li_2O-Ga_2O_3-TiO_2 system at 1100 – 1350^oC, b) the Na_2O-Ga_2O_3-TiO_2 system at 1000^oC, 1050^oC and 1350^oC, c) the Na_2O-Ga_2O_3-TiO_2 system at 1150 - 1250^oC, d) the K_2O-Ga_2O_3-TiO_2 system at 1200^oC, and c) the K_2O-Ga_2O_3-TiO_2 system at 1350^oC.

studied, 1000°C – 1350°C, samples prepared as $Na_xGa_{4+x}Ti_{1-x}O_8$, x < 0.7 lie within the $Na_xGa_{4+x}Ti_{1-x}O_8$ (x ≅ 0.7) – Ga_2O_3 – TiO_2 compatibility triangle whereas samples prepared with x > 0.7 lie within the $Na_xGa_{4+x}Ti_{1-x}O_8$ (x ≅ 0.7) – Ga_2O_3 – Na_2O compatibility triangle. Based on structural considerations, we had anticipated that the $Na_xGa_{4+x}Ti_{1-x}O_8$ samples would form as a solid solution with x ranging from 0 to around 0.7 – the upper limit being the approximate value of x reported by Chandrashekar for crystals grown in a flux containing excess sodium.[2] However, the results of our study suggest that the $Na_xGa_{4+x}Ti_{1-x}O_8$ forms with either a relatively narrow solid solution (0.5 < x < 0.9) or that it forms a compound with x ≅ 0.7.

Most of the samples prepared as $Na_yGa_{4+y}Ti_{2-y}O_{10}$ with y = 0.7 – 1.0 at 1000, 1050 and 1350°C were found to contain only two phases ($Na_{0.7}Ga_{4.7}Ti_{0.3}O_8$ and TiO_2). If we consider $Na_xGa_{4+x}Ti_{1-x}O_8$ (x ≅ 0.7) to exist as a compound, then the prepared $Na_yGa_{4+y}Ti_{2-y}O_{10}$ compositions lie within either the $Na_{0.7}Ga_{4.7}Ti_{0.3}O_8$ – TiO_2 –Ga_2O_3 or the Na_2O – $Na_{0.7}Ga_{4.7}Ti_{0.3}O_8$ – TiO_2 compatibility triangle. Considering that the prepared compositions are quite close to the $Na_{0.7}Ga_{4.7}Ti_{0.3}O_8$ - TiO_2 join, it is plausible that the third phases are present in such small amounts that they were not detected by X-ray diffraction.

The $Na_yGa_{4+y}Ti_{2-y}O_{10}$ samples prepared with y = 0.8 and 1.0 at 1150 and 1200°C showed evidence of a phase similar to that reported by Michiue *et al.*[5] Our results generally agree with those of Michiue *et al.* in that $Na_yGa_{4+y}Ti_{2-y}O_{10}$ was identified in samples prepared with 0.75 < x <1.0 at temperatures lower than 1300°C. However, the phase analysis of our samples suggests that the $Na_yGa_{4+y}Ti_{2-y}O_{10}$ phase has a y value in excess of 1.0.

The $K_xGa_{4+x}Ti_{1-x}O_8$ samples also lie in different compatibility triangles depending on temperature and composition as shown in Figure 3.3d and 3.3e. At 1200°C, the $K_xGa_{4+x}Ti_{1-x}O_8$ samples lay within three compatibility triangles. The x = 0.1 sample lies within the $K_{0.8}Ga_{4.8}Ti_{2.2}O_{12}$-$Ga_2O_3$-$TiO_2$ triangle. The x = 0.3 and 0.5 samples lie within the $K_{2.56}Ga_{22}O_{34.28}$-Ga_2O_3-$K_{0.8}Ga_{4.8}Ti_{2.2}O_{12}$ compatibility triangle. The results of phase analysis suggest that the x = 0.7 sample lies in the $K_{2.56}Ga_{22}O_{34.28}$-Ga_2O_3-$K_{0.8}Ga_{4.8}Ti_{2.2}O_{12}$ compatibility triangle, but Figure 3.3b suggests that the starting composition of the x = 0.7 sample lies outside of this compatibility triangle. The weight

loss of the x = 0.7 sample, presumably due to the loss of volatilization K_2O, was sufficient to yield a potassium concentration of x ~ 0.579, which would lie just inside the $K_{2.56}Ga_{22}O_{34.28}$-Ga_2O_3-$K_{0.8}Ga_{4.8}Ti_{2.2}O_{12}$ compatibility triangle.

At 1350°C, phase analysis indicated that all of the samples existed within the $K_{2.56}Ga_{22}O_{34.28}$-Ga_2O_3-$K_{0.14}Ga_{2.14}Ti_{1.86}O_7$ composition triangle. The starting composition of the x = 0.7 sample lies outside of this compatibility triangle, but the weight loss of this sample was sufficient to bring it within the compatibility triangle. Upon heating to 1350°C, the $K_{0.8}Ga_{4.8}Ti_{2.2}O_{12}$ phase decomposed, and $K_{0.14}Ga_{2.14}Ti_{1.86}O_7$ formed.[8,9] The $K_{0.8}Ga_{4.8}Ti_{2.2}O_{12}$ phase is isostructural with the $Na_{0.8}Ga_{4.8}Ti_{2.2}O_{12}$ phase (Figure 3.2 b), which is reported to be unstable above 1250°C.[4,5]

3.4.2. Computer simulations of $A_xGa_{4+x}Ti_{1-x}O_8$

Table 3.V summarizes the structural parameters and minimized lattice energy of Ga_4TiO_8 and its alkali-containing derivatives. Simulated lattice parameters and atom positions of $Na_{0.7}Ga_{4.7}Ti_{0.3}O_8$ agreed with those reported by Chandrashekar *et al.*[2] The simulated lattice parameters of the metastable phase, Ga_4TiO_8, are in good agreement with those reported by Bursill and Stone.[23] Computer simulations were also conducted to investigate Ga-Ti site mixing in Ga_4TiO_8 and $Na_xGa_{4+x}Ti_{1-x}O_8$. In all cases, site mixing resulted in an increase in lattice energy (not shown), thereby confirming that atom assignments shown in Table 3.V are favored. The lattice energies of the alkali-containing derivatives are higher than that of the parent structure. Lattice energy and unit cell volumes increase with increasing size of the alkali cation.

In an attempt to provide insight as to why $Na_{0.7}Ga_{4.7}Ti_{0.3}O_8$ forms and why $Li_xGa_{4+x}Ti_{1-x}O_8$, and $K_xGa_{4-x}Ti_{1-x}O_8$ do not, simulations were conducted to compare the lattice energies of the intergrowths to the weighted sum of the lattice energies of the component single oxides and to the observed mixed phase assemblages. The lattice energies used in these calculations are summarized in Table 3.VI.

The lattice energy of Ga_4TiO_8 is compared to those of two compositionally equivalent mixtures in Table 3.VII. The lattice energy calculations suggest that a mixture of Ga_2O_3 and TiO_2 in a 2:1 molar ratio (-423.49 eV) is preferred over the formation of the

Table 3.V. Structural Parameters and Lattice Energy of Ga_4TiO_8 and $A_{0.7}Ga_{4.7}Ti_{0.3}O_8$

Phase and Lattice Parameters	Atom Positions				Bond Valence Sum (Obtained/Expected)
	Site	x	y	z	
Ga_4TiO_8	Ti1	0.0000	0.0	0.0000	4.30/4.00
a=11.8000 Å	Ga1	0.2422	0.0	0.6373	2.94/3.00
b= 3.1480 Å	Ga2	0.4549	0.0	0.2855	3.08/3.00
c= 9.4175 Å	O1	0.1663	0.0	0.2171	
β=125.6716°	O2	0.3535	0.0	0.5348	
V=284.1796 Å^3	O3	0.4584	0.0	0.0938	
S.G. = C 2/m	O4	0.1056	0.0	0.6888	
Lattice Energy =-422.66 eV					
$Li_{0.7}Ga_{4.7}Ti_{0.3}O_8$	Li1	0.2288	0.0	0.0281	
a=12.0573 Å	M1	0.0000	0.0	0.0000	3.32/3.30
b= 3.0764 Å	Ga1	0.2445	0.0	0.6450	2.96/3.00
c= 9.2689 Å	Ga2	0.4754	0.0	0.3036	3.10/3.00
β=122.4054°	O1	0.1640	0.0	0.2187	
V=290.2711 Å^3	O2	0.3493	0.0	0.5273	
S.G. = C 2/m	O3	0.4505	0.0	0.0927	
Lattice Energy =-403.25 eV	O4	0.0927	0.0	0.6850	
$Na_{0.7}Ga_{4.7}Ti_{0.3}O_8$	Na1	0.2325	0.0	0.0148	
a=12.1515 Å	M1	0.0000	0.0	0.0000	3.29/3.30
b= 3.0772 Å	Ga1	0.2449	0.0	0.6465	2.91/3.00
c= 9.2580 Å	Ga2	0.4783	0.0	0.3081	3.09/3.00
β=122.1460°	O1	0.1665	0.0	0.2160	
V=293.1047 Å^3	O2	0.3478	0.0	0.5262	
S.G. = C 2/m	O3	0.4570	0.0	0.0990	
Lattice Energy =-402.63 eV	O4	0.0980	0.0	0.6810	
$K_{0.7}Ga_{4.7}Ti_{0.3}O_8$	K1	0.2385	0.0	0.0053	
a=12.3230 Å	M1	0.0000	0.0	0.0000	3.23/3.30
b= 3.0706 Å	Ga1	0.2451	0.0	0.6483	2.85/3.00
c= 9.2516 Å	Ga2	0.4837	0.0	0.3155	3.07/3.00
β=121.7121°	O1	0.1706	0.0	0.2114	
V=297.8072 Å^3	O2	0.3449	0.0	0.5245	
S.G. = C 2/m	O3	0.4677	0.0	0.1093	
Lattice Energy =-401.49 eV	O4	0.0925	0.0	0.6725	

M1 = mixed occupancy Ti/Ga = 0.7 / 0.3; Li1, Na1, and K1 occupancy = 0.35. All other species at full occupancy

Table 3.VI. Minimized Lattice Energies of Observed and Component Oxides

Phase	**Lattice Energy (eV per formula unit)**	**Structure Reference**
Ga_2O_3	-153.83	[12]
TiO_2	-115.83	[19]
Li_2O	-28.40	[21]
Na_2O	-24.90	[21]
K_2O	-24.19	[20]
Ga_2TiO_5	-266.90	[14]
$LiGa_5O_8$	-399.93	[18]
$K_{0.8}Ga_{4.8}Ti_{2.2}O_{12}$	-629.45	[8]
$K_{2.56}Ga_{22}O_{34.28}$	-1650.49	[17]

Table 3.VII. Comparison of the Lattice of Energy of Ga_4TiO_8 to Compositionally Equivalent Mixtures

Phase	**Lattice Energy (eV per formula unit)**
Ga_4TiO_8	-422.66
$2Ga_2O_3 + TiO_2$	**-423.49**
$Ga_2TiO_5 + Ga_2O_3$	-420.73

Ga_4TiO_8 intergrowth (-422.66 eV). These results are in agreement with the experimental results reported by Lejus[24] who reported that TiO_2 and Ga_2O_3 are the only phases stable in the Ga_2O_3-TiO_2 system below ~ 1100°C.

Figure 3.4 shows the calculated lattice energies of $Li_xGa_{4+x}Ti_{1-x}O_8$ in comparison to compositionally equivalent mixtures. The lattice energy of the component oxides, E_{comp}, and the lattice energy of the observed oxides, E_{obs} were calculated as:

$$E_{comp} = \frac{x}{2}E_{Li_2O} + \frac{4+x}{2}E_{Ga_2O_3} + (1-x)E_{TiO_2} \quad (3)$$

$$E_{obs} = xE_{LiGa_5O_8} + \frac{4-4x}{2}E_{Ga_2O_3} + (1-x)E_{TiO_2} \quad (4)$$

In general, the lattice energy of $Li_xGa_{4+x}Ti_{1-x}O_8$ is 1.5 – 4.0 eV greater than either a mixture of Ga_2O_3, Li_2O, and TiO_2 or a mixture of Ga_2O_3, Ga_5LiO_8, and TiO_2. In this case, lattice energy calculations predict the formation of the observed mixture, i.e. the mixture of Ga_2O_3, Ga_5LiO_8, and TiO_2 has the lowest lattice energy over the entire composition range studied.

Figure 3.5 shows the lattice energy of $Na_xGa_{4+x}Ti_{1-x}O_8$ in comparison to compositionally equivalent mixtures. The lattice energy of the component oxides, E_{comp}, was calculated as:

$$E_{comp} = \frac{x}{2}E_{Na_2O} + \frac{4+x}{2}E_{Ga_2O_3} + (1-x)E_{TiO_2} \quad (5)$$

The lattice energy of the oxides observed at 1000 °C were calculated as:

$$E_{obs,lowx} = \frac{x}{0.7}E_{Na_{0.7}Ga_{4.7}Ti_{0.3}O_8} + \frac{4-5.71x}{2}E_{Ga_2O_3} + \frac{0.7-x}{0.7}E_{TiO_2} \quad (6)$$

$$E_{obs,highx} = \frac{1-x}{0.3}E_{Na_{0.7}Ga_{4.7}Ti_{0.3}O_8} + \frac{16.67x-11.67}{2}E_{Ga_2O_3} + \frac{3.33x-2.33}{2}E_{Na_2O} \quad (7)$$

where $E_{obs,low\ x}$ is valid for $x \leq 0.7$ and $E_{obs,highx}$ is valid for $x \geq 0.7$.

For the sodium-containing compositions, the simulations do not support the experimental observations. The simulations suggest that a mixture of the component oxides – Ga_2O_3, Na_2O, and TiO_2 – is preferred over the observed phases. While the simulations do indicate that the observed mixture of phases is preferred over a single intergrowth phase for $x \neq 0.7$, the concurrence of the lattice energies of the intergrowth and the observed phases at $x = 0.7$ is not particularly significant since $Na_{0.7}Ga_{4.7}Ti_{0.3}O_8$

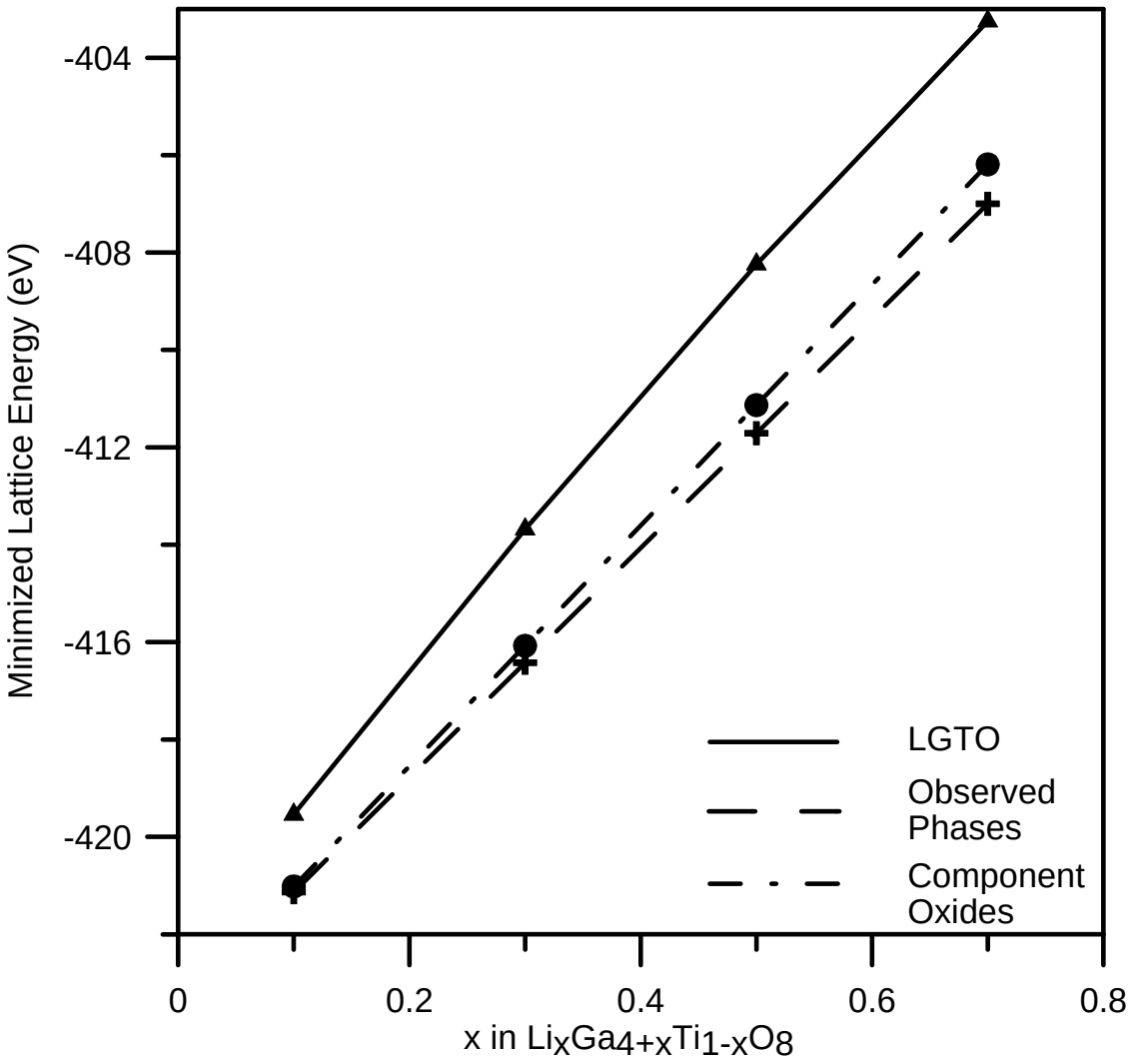

Figure 3.4. Calculated (minimized) lattice energies of BGR-derived structure, observed phase mixture, and component oxide mixture as a function of x in $Li_xGa_{4+x}Ti_{1-x}O_8$.

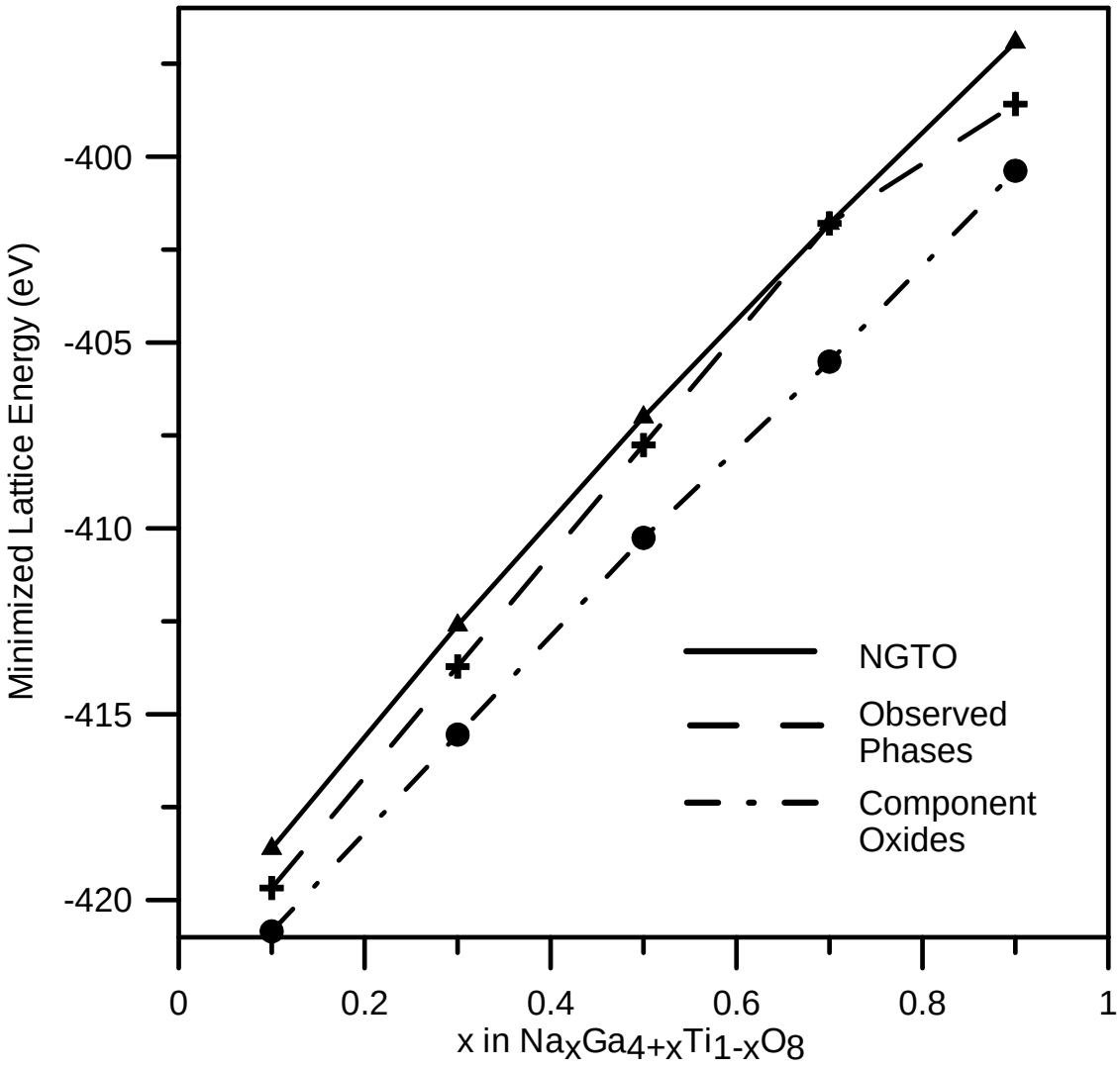

Figure 3.5. Calculated (minimized) lattice energies of BGR-derived structure, observed phase mixture, and component oxide mixture as a function of x in $Na_xGa_{4+x}Ti_{1-x}O_8$.

was a component in the observed mixture. The near linear increase in lattice energy with increasing x does not provide a ready explanation as to why the intergrowth forms with x ≅ 0.7.

One possible explanation for the discrepancy between the observed and predicted phases in the Na_2O-Ga_2O_3-TiO_2 system is that the static lattice energy calculations conducted in this study do not consider the contributions of entropy and temperature to the free energy of the system. In the structure of the BGR derivative, sodium resides on a site that is only partially occupied and one of the framework cation sites has mixed Ga/Ti occupancy. The configurational entropy resulting from site mixing (per formula unit) can be expressed in terms of x as:

$$\Delta S_{conf} = -k\left[x\ln(x) + (1-x)\ln(1-x) + 2\left[\frac{x}{2}\ln\left(\frac{x}{2}\right) + \left(1-\frac{x}{2}\right)\ln\left(1-\frac{x}{2}\right)\right]\right] \qquad (8)$$

By taking the derivative of this expression and setting it equal to zero,

$$\frac{d\Delta S_{conf}}{dx} = -k\ln\frac{x^2}{(1-x)(2-x)} = 0 \quad \rightarrow \quad x = 0.667 \qquad (9)$$

one can show that the maximum configurational entropy occurs at x = 0.667, near the reported stable composition of x ≅ 0.7. However, the TΔS term associated with the configurational entropy, which is approximately 0.2 eV at 1273 K, is not sufficient to compensate for differences in lattice energy and to explain the formation of the observed phase. Another possible explanation for the discrepancy between the predicted and observed phases is that the model does not consider possible association energies between sodium and the framework ions.

Figure 3.6 shows the lattice energy of $K_xGa_{4+x}Ti_{1-x}O_8$ compared to that of the compositionally equivalent mixtures. The lattice energy of the component oxides, E_{comp}, was calculated as:

$$E_{comp} = \frac{x}{2}E_{K_2O} + \frac{4+x}{2}E_{Ga_2O_3} + (1-x)E_{TiO_2} \qquad (10)$$

For the K_2O-Ga_2O_3-TiO_2 system, the observed phases changed with overall composition and temperature. The lattice energies for the observed phases at 1200 ^oC were calculated according to Eqs. 11-13, where $E_{obs,lowx}$ is for x<0.267, $E_{obs,midx}$ is for 0.267< x <0.579, and $E_{obs,highx}$ is for 0.579< x <0.7.

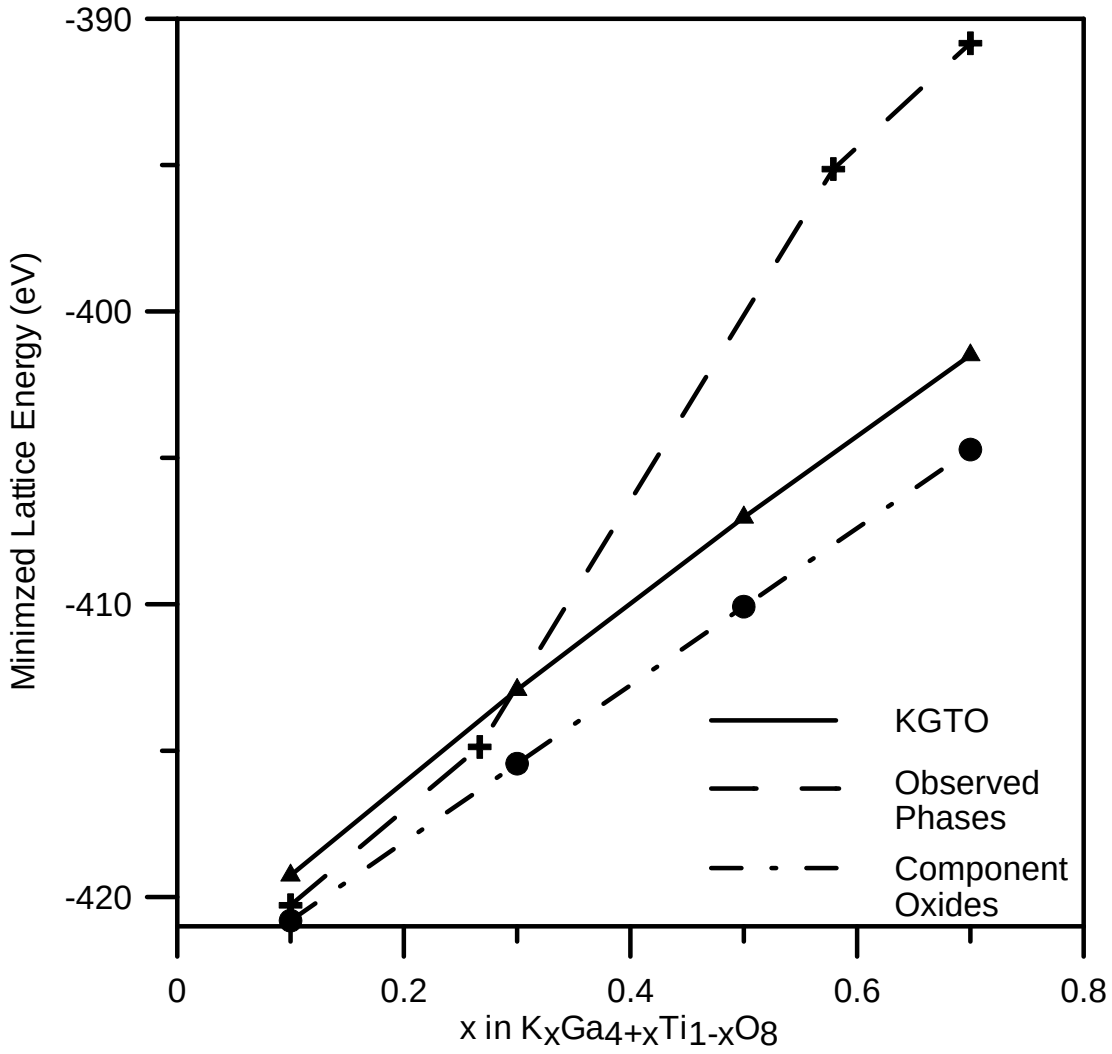

Figure 3.6. Calculated (minimized) lattice energies of BGR-derived structure, observed phase mixture, and component oxide mixture as a function of x in $K_xGa_{4+x}Ti_{1-x}O_8$.

$$E_{obs,low\,x} = \frac{x}{0.8} E_{Ka_{0.8}Ga_{4.8}Ti_{2.2}O_{12}} + \frac{4-5x}{2} E_{Ga_2O_3} + (1-3.75x) E_{TiO_2} \quad (11)$$

$$E_{obs,mid\,x} = \frac{1-x}{2.2} E_{Ka_{0.8}Ga_{4.8}Ti_{2.2}O_{12}} + \frac{1.36x-0.364}{2.56} E_{K_{2.56}Ga_{22}O_{34.28}} + \frac{4.94-8.53x}{2} E_{Ga_2O_3} \quad (12)$$

$$E_{obs,high\,x} = \frac{1-x}{2.2} E_{Ka_{0.8}Ga_{4.8}Ti_{2.2}O_{12}} + \frac{1.82x-3.18}{22} E_{K_{2.56}Ga_{22}O_{34.28}} + \frac{0.994x-0.575}{2} E_{K_2O} \quad (13)$$

As in the case of the sodium-containing system, the simulations do not support the experimental observations. The simulations suggest that the mixture of single-component oxides is preferred over the entire composition range. The simulations also suggest that the intergrowth phase is preferred over the observed phases at low x values. The discrepancy between the predictions and observations suggests that the model is inadequate, perhaps because it did not consider the effects of temperature, changes in entropy, or any association interactions between potassium and the host-structure ions.

3.4.3. Computer simulations of $Na_{0.8}Ga_{4.8}Ti_{1.2}O_{10}$ and $Na_{0.8}Ga_{4.8}Ti_{2.2}O_{12}$

Computer simulations were also conducted to compare the lattice energies of reported (Figure 3.2) and BGR-derived (Figure 3.1c-e) structures with compositions expressed as $Na_{0.8}Ga_{4.8}Ti_{1.2}O_{10}$ and $Na_{0.8}Ga_{4.8}Ti_{2.2}O_{12}$. The results are shown in Tables 3.VIII and 3.IX.

The structure of $Na_{0.8}Ga_{4.8}Ti_{1.2}O_{10}$ reported by Michiue *et al.*[5] (Figure 3.2a) has the same composition as the structure derived from an n = 6 BGR intergrowth (Figure 3.1c). Both structures maintain a beta-gallia subunit, characterized by a pair of edge-sharing octahedra and two tetrahedra. In the reported structure (Figure 3.2a), columns of edge-sharing octahedra separate beta-gallia subunits. This arrangement results in eight-sided tunnels, which host the sodium ions. In the case of the BGR derivative, columns of corner-sharing octahedra separate the beta-gallia subunits, which results in the formation of six-sided tunnels.

As shown in Table VIII, the simulated structure of C2/m $Na_{0.8}Ga_{4.8}Ti_{1.2}O_{10}$ is in good agreement with the reported structure.[4] The bond valance sums calculated for both structures are within 3% of their expected values, which attests to the validity of the potential models. The unit cell volume of the BGR derivative is around 8% smaller than

Table 3.VIII. Structural Parameters and Lattice Energy of $A_{0.8}Ga_{4.8}Ti_{1.2}O_{10}$

Phase and Lattice Parameters	Atom Positions				Occupancy	Bond Valence Sum (Obtained / Expected)
	Site	x	y	z		
$A_{0.8}Ga_{4.8}Ti_{1.2}O_{10}$	Na1	0.0000	0.0	0.5	0.57	
As reported [4]	Na2	0.0000	0.285(58)	0.5	0.12	
(Figure 2a)	M1	0.26466(5)	0.0	0.62584(5)	0.60 / 0.40*	3.50/3.60
a=12.093(2) Å	Ga1	0.32353(4)	0.0	0.10149(4)	1.0	3.02/3.00
b= 3.0117(5) Å	Ga2	0.06370(4)	0.0	0.16338(4)	1.0	3.04/3.00
c=10.4134(9) Å	O1	0.1640(2)	0.0	0.0316(3)	1.0	
β=92.29(1)^o	O2	0.1304(2)	0.0	0.3244(3)	1.0	
V=378.94(9) Å^3	O3	0.2047(2)	0.0	0.7896(3)	1.0	
S.G. = C 2/m	O4	0.3243(2)	0.0	0.4461(3)	1.0	
Lattice Energy	O5	0.4803(2)	0.0	0.1431(3)	1.0	
= -510.39 eV						
$A_{0.8}Ga_{4.8}Ti_{1.2}O_{10}$	Na1	0.0000	0.0	0.5	0.55	
Post	Na2	0.0000	0.3858	0.5	0.125	
Simulation	M1	0.2601	0.0	0.6305	0.60 / 0.40*	3.67/3.60
(Figure 2a)	Ga1	0.3243	0.0	0.1020	1.0	3.10/3.00
a=11.8984 Å	Ga2	0.0604	0.0	0.1565	1.0	2.97/3.00
b= 3.1189 Å	O1	0.1636	0.0	0.0262	1.0	
c=10.3965 Å	O2	0.1446	0.0	0.3070	1.0	
β=92.2581^o	O3	0.1996	0.0	0.7917	1.0	
V=385.5126 Å^3	O4	0.3141	0.0	0.4502	1.0	
S.G. = C 2/m	O5	0.4847	0.0	0.1388	1.0	
Lattice Energy						
= -513.69 eV						
$A_{0.8}Ga_{4.8}Ti_{1.2}O_{10}$	Na1	0.1989	0.0	0.8511	0.80	
Post	M2	0.0000	0.0	0.0000	0.60 / 0.40*	3.70/3.60
Simulation	M3	0.5000	0.0	0.0000	0.60 / 0.40*	3.67/3.60
(Figure 1c)	M4	0.5785	0.5	0.3107	0.60 / 0.40*	3.60/3.60
a=10.9060 Å	Ga1	0.0718	0.5	0.2928	1.0	2.93/3.00
b= 3.0789 Å	Ga2	0.1514	0.0	0.5857	1.0	2.97/3.00
c=10.6561 Å	Ga3	0.2814	0.5	0.1110	1.0	2.95/3.00
β=101.2002^o	Ga4	0.3238	0.0	0.3969	1.0	3.03/3.00
V=351.0060 Å^3	O1	0.3366	0.0	0.0480	1.0	
S.G. = P 2/m	O2	0.0254	0.0	0.1817	1.0	
Lattice Energy	O3	0.4707	0.0	0.3255	1.0	
= -515.93 eV	O4	0.6924	0.0	0.3082	1.0	
	O5	0.1366	0.0	0.4114	1.0	
	O6	0.1186	0.5	0.0182	1.0	
	O7	0.5280	0.5	0.1181	1.0	
	O8	0.2560	0.5	0.2747	1.0	
	O9	0.3406	0.5	0.5108	1.0	
	O10	0.0821	0.5	0.6352	1.0	

*All M site occupancies are expressed in the form of Ti / Ga.

Table 3.IX. Structural Parameters and Lattice Energy of $A_{0.8}Ga_{4.8}Ti_{2.2}O_{12}$

Phase and Lattice Parameters	Atom Positions				Occupancy	Bond Valence Sum (obtained / expected)
	Site	x	y	z		
$A_{0.8}Ga_{4.8}Ti_{2.2}O_{12}$	Na1	0.000000	0.0	0.172(8)	0.40	
As reported [6]	M1	0.1995(2)	0.0022(6)	0.5	0.20 / 0.80*	3.14/3.20
(Figure 2b)	M2	0.3529(4)	0.2208(6)	0.0	0.86 / 0.14*	3.97/3.86
a=15.8278(4) Å	M3	0.000000	0.5	0.5	0.08 / 0.92*	3.11/3.08
b= 9.3326(2) Å	Ga1	0.1443(3)	0.2991(5)	0.0	1.0	3.12/3.00
c= 2.9981(1) Å	O1	0.144(1)	0.102(2)	0.0	1.0	
V= 442.86 $Å^3$	O2	0.295(1)	0.128(2)	0.5	1.0	
S.G. = Pbam	O3	0.444(1)	0.104(2)	0.0	1.0	
Lattice Energy	O4	0.092(1)	0.360(2)	0.5	1.0	
= -624.26 eV	O5	0.250(1)	0.381(2)	0.0	1.0	
	O6	0.386(1)	0.343(2)	0.5	1.0	
$A_{0.8}Ga_{4.8}Ti_{2.2}O_{12}$	Na1	0.0000	0.0	0.2485	0.40	
Post	M1	0.2014	0.0038	0.5	0.20 / 0.80*	3.21/3.20
Simulation	M2	0.3529	0.2171	0.0	0.86 / 0.14*	3.93/3.86
(Figure 2b)	M3	0.0000	0.5	0.5	0.08 / 0.92*	3.13/3.08
a=15.5523 Å	Ga1	0.1403	0.3070	0.0	1.0	3.09/3.00
b= 9.2263 Å	O1	0.1551	0.1081	0.0	1.0	
c= 3.1205 Å	O2	0.2968	0.1303	0.5	1.0	
V= 447.7569 $Å^3$	O3	0.4422	0.0917	0.0	1.0	
S.G. = Pbam	O4	0.0908	0.3529	0.5	1.0	
Lattice Energy	O5	0.2534	0.3794	0.0	1.0	
= -627.99 eV	O6	0.3804	0.3416	0.5	1.0	

*All M site occupancies are expressed in the form of Ti / Ga.

Table 3.IX. (cont.) Structural Parameters and Lattice Energy of $A_{0.8}Ga_{4.8}Ti_{2.2}O_{12}$

Phase and Lattice Parameters	Atom Positions				Occupancy	Bond Valence Sum (obtained / expected)
	Site	x	y	z		
$A_{0.8}Ga_{4.8}Ti_{2.2}O_{12}$	Na1	0.8251	0.5	0.7345	0.80	
Post	M4	0.0000	0.0	0.0000	0.7332/0.2668*	3.90/3.73
Simulation	M5	0.5000	0.5	0.0000	0.7332/0.2668*	3.48/3.73
(Figure 1d)	M6	0.4212	0.0	0.2655	0.7334/0.2666*	3.82/3.73
a=13.1775 Å	M7	0.6460	0.5	0.4696	0.7334/0.2666*	3.63/3.73
b= 3.1076 Å	Ga1	0.2788	0.0	0.7739	1.0	2.91/3.00
c=10.5242 Å	Ga2	0.0635	0.5	0.7478	1.0	2.88/3.00
β=108.2160°	Ga3	0.2430	0.5	0.0413	1.0	3.04/3.00
V=409.3728 Å^3	Ga4	0.1238	0.0	0.4920	1.0	3.00/3.00
S.G. = P 2/m	O1	0.0988	0.5	0.0312	1.0	
Lattice Energy	O2	0.0145	0.0	0.8265	1.0	
= -630.46 eV	O3	0.2799	0.0	0.1345	1.0	
	O4	0.3876	0.5	0.3629	1.0	
	O5	0.2564	0.0	0.4644	1.0	
	O6	0.0648	0.5	0.4112	1.0	
	O7	0.1185	0.0	0.6644	1.0	
	O8	0.2235	0.5	0.8623	1.0	
	O9	0.4116	0.0	0.9181	1.0	
	O10	0.2880	0.5	0.6657	1.0	
	O11	0.4312	0.5	0.1499	1.0	
	O12	0.5590	0.0	0.3871	1.0	
$A_{0.8}Ga_{4.8}Ti_{2.2}O_{12}$	Na1	0.2808	0.0	0.0204	0.40	
Post	M8	0.4327	0.0	0.2731	0.7334/0.2666*	3.70/3.73
Simulation	M9	0.0000	0.0	0.0000	0.7332/0.2668*	3.79/3.73
(Figure 1e)	Ga1	0.1973	0.5	0.2250	1.0	2.92/3.00
a =13.3519 Å	Ga2	0.1457	0.0	0.4855	1.0	3.02/3.00
b= 3.0929 Å	O1	0.1419	0.0	0.1327	1.0	
c= 10.5180 Å	O2	0.3313	0.5	0.2054	1.0	
β=107.8524°	O3	0.4715	0.0	0.0996	1.0	
V= 413.44 Å^3	O4	0.0186	0.0	0.3372	1.0	
S.G. = C 2/m	O5	0.2003	0.5	0.3983	1.0	
Lattice Energy	O6	0.1260	0.5	0.5867	1.0	
= -628.21 eV						

*All M site occupancies are expressed in the form of Ti / Ga.

the observed C2/m structure. The calculated lattice energy of the BGR derivative (P2/m structure, Figure 3.1c) is 2.24 eV lower than that of the reported $Na_{0.8}Ga_{4.8}Ti_{1.2}O_{10}$ structure (C2/m, Figure 3.2a), which suggests that the BGR derivative should be the preferred phase, excluding possible temperature and configurational entropy effects.

Additional simulations were conducted with different Ga/Ti distributions on the cation sites. In all cases, these resulted in further decreases in the minimized lattice energy, but sometimes resulted in larger deviations in the bond valence sums.

The structure of $Na_{0.8}Ga_{4.8}Ti_{2.2}O_{12}$ reported by Michiue *et al.*[4] (Figure 3.2b) has the same composition as structures derived from the n = 7 P2/m and C2/m BGR intergrowths (Figure 3.1d and e). The reported structure of $Na_{0.8}Ga_{4.8}Ti_{2.2}O_{12}$ is similar to the reported structure of $Na_{0.8}Ga_{4.8}Ti_{1.2}O_{10}$ in that it possesses eight-sided tunnels. However, it does not retain complete beta-gallia subunits, i.e. two edge-sharing octahedral flanked by two corner-sharing tetrahedra. The two BGR-derived structures (Figures 3.1d and 3.1e) both contain hexagonal tunnels and complete beta-gallia subunits, but differ in the way in which the beta-gallia and TiO_6 octahedra (i.e. the rutile component) are arranged.

As shown in Table 3.IX, the simulated Pbam structure is in good agreement with the reported structure. The unit cell volumes of the simulated P2/m and C2/m BGR derivatives are within 2% of unit cell volumes reported for $Ga_4Ti_3O_{12}$.[13] The bond valance sums are within 7% of their expected values. The simulated P2/m n = 7 BGR derivative (Figure 3.1d) has a lower lattice energy than that of both the C2/m BGR derivative (Figure 3.1e) and the reported Pbam structure (Figure 3.2b). Excluding the effects of temperature and configurational entropy, these results suggests that the P2/m BGR derivative should be preferred over both the C2/m BGR derivative and the observed Pbam structure.

3.5. Conclusions

Lithium and potassium analogs of the reported sodium-ion conductor $Na_xGa_{4+x}Ti_{1-x}O_8$ ($x \cong 0.7$) did not form via solid-state reaction at 1000 – 1350°C. Phase analysis of samples prepared as $Li_xGa_{4+x}Ti_{1-x}O_8$ and $K_xGa_{4+x}Ti_{1-x}O_8$, where $0.1 \leq x \leq 0.7$ suggest a series of subsolidus phase relationships involving the following compatibility triangles: $LiGa_5O_8$–TiO_2–Ga_2O_3 at 1100 – 1350°C; $K_{2.56}Ga_{22}O_{34.28}$ –$K_{0.8}Ga_{4.8}Ti_{2.2}O_{12}$–$Ga_2O_3$ and $K_{0.8}Ga_{4.8}Ti_{2.2}O_{12}$ –TiO_2–Ga_2O_3 at 1200°C; and $K_{2.56}Ga_{22}O_{34.28}$–$K_{0.14}Ga_{2.14}Ti_{1.86}O_7$–$Ga_2O_3$ and $K_{0.14}Ga_{2.14}Ti_{1.86}O_7$–$TiO_2$–$Ga_2O_3$ at 1350°C

The sodium ion conductor $Na_xGa_{4+x}Ti_{1-x}O_8$, which is structurally related to the n = 5 member of the C2/m beta-gallia-rutile intergrowth series, formed via solid-state reaction over the temperature range 1000 – 1350°C. This phase appears to exist as a compound (or perhaps a very limited solid solution) with $x \cong 0.7$. Another phase, expressed as $Na_yGa_{4+y}Ti_{2-y}O_{10}$, formed via solid-state reaction in the temperature range of 1050 – 1250°C, but was not obtained as a phase-pure sample. The phase assemblages observed in this sample are consistent with $Na_{0.7}Ga_{4.7}Ti_{0.3}O_8$–$TiO_2$–$Ga_2O_3$ and $Na_yGa_{4+y}Ti_{2-y}O_{10}$–$Na_{0.7}Ga_{4.7}Ti_{0.3}O_8$–$TiO_2$ compatibility triangles providing that $y > 1.0$.

Computer simulations were used in an attempt to predict (explain) the preferred phase assemblages. In the case of the Ga_2O_3-TiO_2 and the Li_2O-Ga_2O_3-TiO_2 systems, the calculations were in agreement with the experimental observations. In the case of the sodium and potassium-containing systems, the computer simulations did not support the experimental observations.

3.6 References:

1. D.D. Edwards, T.O. Mason, W. Sinkler, L.D. Marks, K.R. Poeppelmeier, Z. Hu, and J.D. Jorgensen, "Tunneled Intergrowth Structures in the Ga_2O_3-In_2O_3-SnO_2 System," *J. Solid State Chem.*, **150** [2] 294-304 (2000).

2. G.V. Chandrashekar, A. Bednowitz, and S.J. La Placa, "A One Dimensional Sodium Ion Conductor," pp. 447-50 in *Fast Ion Transport in Solids.* Edited by P. Vashishta, J. N. Mundy, and G. K. Shenoy. Elsevier, New York, 1979.

3. Y. Fujiki, M. Watanabe, T. Sasaki, T. Mitsuhashi, Y. Onoda, S. Yoshikado, T. Ohachi, and I. Taniguchi, "Flux Growth of $A_x[Ga_8Ga_{8+x}Ti_{16-x}O_{56}]$ (A=K, Rb, Cs) Single Crystals," *Solid State Ionics,* **40-41** [1] 136-8 (1990).

4. Y. Michiue, T. Sasaki, M. Watanabe, and Y. Fujiki, "Synthesis and Structure Refinement of Sodium Titanogallate Containing One-dimensional Channels of Large Cross Section," *Mater. Res. Bull.*, **28** [2] 173-8 (1993).

5. Y. Michiue and M. Watanabe, "Synthesis and Structure of New Sodium Titanogallate $Na_xTi_{2-x}Ga_{4+x}O_{10}$, Containing One-dimensional Channels," *Solid State Ionics,* **70-71** [1] 186-90 (1994).

6. Y. Michiue, M. Watanbe, and Y. Fujiki, "Flux Growth and Structure Refinement of Na_xGa_x $Ti_{4-x}O_8$," *Mater. Res. Bull.*, **26** [7] 597-603 (1991).

7. T. Mori, J. Suzuki, K. Fujimoto, M. Watanabe, and Y. Hasegawa, "Photocatalytic Reductions of Nitric Oxide in Gas Phase and Nitrate Ion in Water with Reducing Agents on Hollandite Catalyst," *Mater. Res. Soc. Symp. Proc.*, **529**, 125-30 (1999).

8. M. Watanabe, Y. Fujiki, S. Yoshikado, and T. Ohachi, "Structural Features of a New Compound $K_{1-x}Ti_{2+x}Ga_{5-x}O_{12}$ Which Exhibits One-Dimensional Ionic Conduction," *Solid State Ionics,* **35** [3-4] 369-75 (1989).

9. M. Watanabe, T. Sasaki, Y. Kitami, and Y. Fujiki, "Potassium Gallotitanogallate, $K_x[Ga_{2+x}Ti_{2-x}O_7]$ (x</0.25)," *Acta. Cryst.*, **C43** [3] 392-5 (1987).

10. J. Gale, *GULP Manual*. Imperial College of London, Department of Chemistry, London, 1998.

11. G.V. Lewis and C.R.A. Catlow, "Potential Models for Ionic Oxides," *J. Phys. C: Solid State Phys.*, **18** [6] 1149-61 (1985).

12. J. Ahman, G. Svensson, and J. Albertsson, "A Reinvestigation of Beta-gallium Oxide," *Acta Cryst.*, **C52** [6] 1336-8 (1996).

13. A. Kahn, V. Agafonov, D. Michel, and M. Perez Y Jorba, "New Gallium Germanates with Tunnel Structures: alpha-Ga_4GeO_8 and $Ga_4Ge_3O_{12}$," *J. Solid State Chem.,* **65** [3] 377-82 (1986).

14. H. Mueller-Buschbaum and H.R. Freund, "Zur Kristallchemie von Ga_2TiO_5," *Z. Naturforsch.,* **29**, 590-3 (1974).

15. F.R. Theobald, C.R.A. Catlow, and A.N. Cormack, "Lattice Energy Minimization as a Contemporary Technique to Refine Structures Obtained by High-resolution Electron Microscopy," *J. Solid State Chem,* **52** [1] 80-90 (1984).

16. I.D. Brown and D. Altermatt, "Bond-valence Parameters Obtained from a Systematic Analysis of the Inorganic Crystal Structure Database," *Acta. Cryst.,* **B41** [4] 244-8 (1985).

17. H. Ikawa, T. Tsurumi, M. Ishimori, K. Urabe, and S. Udagawa, "Chemical Composition and Crystal Structure of Beta-alumina Type R^+ Gallate ($R^+ = K^+$, NH_4^+)," *J. Solid State Chem.,* **60** [1] 51-61 (1985).

18. J. Joubert, M. Brunel, A. Waintal, and A. Durif, "Etude Cristallographique du Gallate de Lithium et de sa Solution Solide Avec l'Aluminate," *C. R. l'Academie. Sci.,* **256**, 5324-6 (1963).

19. K. Sugiyama and Y. Takeuchi, "The Crystal Strucutre of Rutile as a Function of Temperature up to 1600 degrees C," *Z. Kristallogr.,* **194**, 305-13 (1991).

20. P. Touzain, F. Brisse, and M. Caillet, "Systemes Metaux Alcalins-oxygene eme Partie. Polymorhisme du Monoxide de Potassium K_2O," *Can. J. Chem.,* **48**, 3358-61 (1970).

21. E. Zintl, A. Harder, and B. Dauth, "Gitterstruktur der Oxide, Sulfide, Selenide und Telluride des Lithiums, Natriums and Kaliums," *Z. Elektrochem.,* **198**, 88-101 (1934).

22. D.D. Edwards and T.O. Mason, "Subsolidus Phase Relations in the Ga_2O_3-In_2O_3-SnO_2 System," *J. Am. Ceram. Soc.,* **81** [12] 3285-91 (1998).

23. L.A. Bursill and G.G. Stone, "Tunnel and Intergrowth Structures in the Gallia-rich Gallium Titanate System," *J. Solid State Chem.,* **38** [2] 149-57 (1981).

24. A. Lejus, D. Goldberg, and A. Revcolevschi, "New Compounds Formed from Rutile, TiO_2, and Oxides of Trivalent and Tetravalent Metals," *C.R. Seances Acad. Sci., Ser. C.,* **263C** [20] 1223-6 (1966).

4. An Atomic Force Microscopy Study of the Interaction of DNA and Nano-Structured Beta-Gallia Rutile.

Abstract

The ability to attach DNA molecules to solid planar substrates is desired for imaging the molecule and for building DNA-mediated nanostructures. The deposition of DNA on [001]-rutile and beta-gallia rutile (BGR) substrates from buffer solutions containing various divalent cations was studied using tapping mode atomic force microscopy. Beta-gallia rutile intergrowths were prepared by spin-coating gallium isopropoxide onto [001]-oriented TiO_2 single crystal slabs and heating above 1350 ^{o}C for >24 hours, resulting in the formation of intergrowth lines along the $\{210\}_r$ planes in the parent rutile structure. Rutile and BGR intergrowth substrates were exposed to various buffered solutions containing DNA and the following divalent cations: Ca (II), Co (II), Cu (II), Fe (II), Mg (II), Mn (II), Ni (II), and Zn (II)). Of all the cations examined, only Ni (II) resulted in the attachment of DNA on the rutile surfaces. DNA attachment to BGR surfaces was strong enough to allow AFM imaging when the deposition buffer contained one of the following cations: Co (II), Mg (II), Mn (II), Ni (II), and Zn(II). For all of these cations, DNA attachment occurred preferentially, but not exclusively, along BGR intergrowth lines. When buffers without cation additions and those containing Ca (II), Cu (II) and Fe (II) were used, DNA failed to bind to the BGR surfaces strongly enough to allow AFM imaging. The mechanism(s) by which DNA attaches to the BGR surface are not well understood but may involve the incorporation of divalent cations at the tunnel sites of the BGR intergrowths.

4.1. Introduction

The ability to attach DNA molecules in patterned arrangements on solid planar substrates is desired for building DNA-mediated nanostructures for optical and electronic devices. A variety of techniques, most involving the covalent bond between sulfur and

gold, have been reported for attaching DNA to a planar substrate. Typically, these techniques require the functionalization of DNA with thiol or disulfide groups and sophisticated manipulation methods for fabricating patterns.[1-5]

The attachment of DNA to planar substrates is also required for AFM studies of the biomolecule. Mica has emerged as the preferred substrate for such studies because of its flatness. The attachment of DNA to mica surfaces is significantly aided when the deposition buffer contains divalent or multivalent cations; where varying cation species and cation concentration has been shown to alter the binding of DNA to the mica surface.[6-14] Thundat *et al*. observed the attachment of DNA to mica surfaces with AFM in air when the mica was chemically modified with Co (II), La (III), Mg (II), and Zr (IV) and noted that superior images were recorded with the divalent species.[13] Hansma *et al.* investigated AFM imaging of DNA bound on mica in an aqueous buffer, where DNA was firmly attached in the presence of Ni (II), Co (II), and Zn (II).[14] The mechanism by which DNA is attached to mica surfaces in the presence of divalent cations is not well understood; however, it has been suggested that crystallographic sites, often referred to as cavities, on the mica surface may play a role. It has been speculated that divalent cations sitting in the surface cavities act as an electrostatic bridge between the negatively charged mica surface and phosphate backbone.[14-17] The amount of DNA adsorbed on mica can be roughly controlled, but without additional surface functionalization, the molecules attach randomly to the surface.[15,18]

In this work, we report on the attachment of DNA to beta-gallia rutile (BGR) substrates. We have selected BGR substrates because they possess features which, with further development, may enable the self-assembly of DNA in patterned arrangements without the need for sophisticated manipulation techniques. BGR substrates possess surface sites which may facilitate the binding of DNA and which align to form patterns related to the material's crystal structure. Beta-gallia rutile intergrowths form when gallia (Ga_2O_3) subunits are inserted into [001]-oriented rutile (TiO_2) along $\{210\}_r$ planes. The lattice mismatch between the two crystal structures leads to the formation of one-dimensional tunnels aligned along $\{210\}_r$ and running perpendicular to the rutile surface. These tunnels are approximately 2.5 Å in diameter, making them a suitable host for a small to medium sized cations.[19] The separation of beta-gallia regions can be controlled

by the ratio of gallium to titanium which is governed by the formula $Ga_4Ti_{n-4}O_{2n-2}$.[19-27] As an example, Figure 4.1 shows the n = 25 ($Ga_4Ti_{21}O_{48}$) member of the intergrowth series. By increasing or decreasing the n value, the distance separating the rows of tunnel-rich beta-gallia regions increases or decreases, respectively.[25] At low n values, the BGR intergrowths are considered compounds that are distinctly different phases from rutile and beta-gallia. At higher n values, the intergrowth structures are often viewed as linear defects in the rutile structure. Incorporation of cations in the tunnel sites has been observed. For example, the structure of the one-dimensional ion conductor $Na_{0.7}Ga_{4.7}O_{0.3}O_8$ can be viewed as a derivative of the n = 5 BGR structure (Ga_4TiO_8) by replacing a portion of the Ti^{4+} cations with Ga^{3+} and inserting an equal number of Na^+ cations in the tunnel sites.[19,28]

Based on cation / DNA interactions observed on mica surfaces, we have speculated that incorporation of divalent cation species at the tunnel sites may provide preferential locations for DNA attachment. The aim of this work was to examine the validity of that speculation. Herein, the observed interaction of DNA with BGR surfaces in the presence of divalent cations via AFM is reported.

4.2. Experimental Procedure

Single crystal TiO_2 (001) oriented substrates (5 x 5 x 0.5 mm) were obtained from MTI corp. (Richmond, CA). To prepare the BGR substrates, a gallium isopropoxide solution (0.15 M) was prepared as described by Liu *et al.*[29] and applied to the surfaces of the rutile substrates via spin coating for 25 seconds at 2500 rpm. The coated substrates were dried for 24 hours prior to heating. Initial experiments were performed on two samples to determine the appropriate heating cycles to form suitable BGR substrates. Additional samples were heated at 900 ^oC for 3 hours, then at 1350^oC for 96 to 480 hrs.

A 1 μg / ul, 100 base pair (bp), DNA ladder (Invitrogen, Carlsbad, CA) containing double stranded DNA molecules of 16 sizes (ranging from 100 to 1500 bp and 2072bp) was diluted to 0.5 ng / μl in buffers of 10 mM HEPES (4- (2-Hydroxyethyl) piperazine-1-ethanesulfonic acid), pH 7 and 1 mM concentrations of various salts ($CaCl_2$, $CoCl_2$,

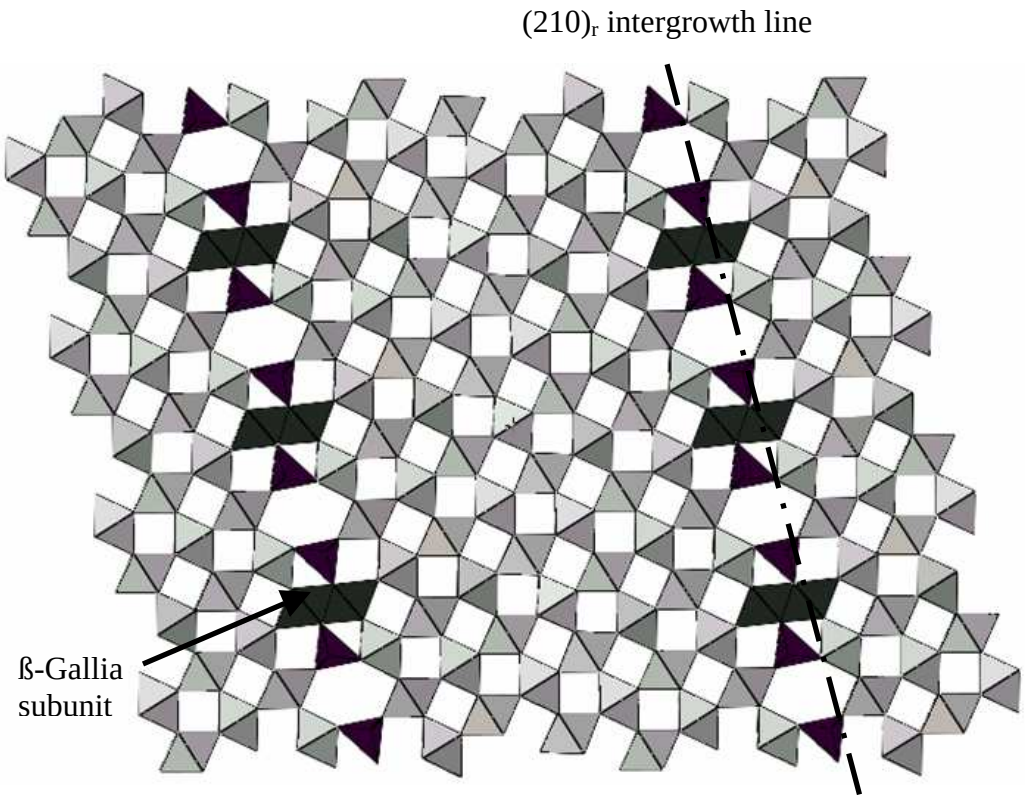

Figure 4.1. Projection of the ß-gallia rutile ($Ga_4Ti_{21}O_{48}$) structure along [001] of the parent rutile structure, after Ref. [24]. Two-dimensional projections of TiO_6 octahedra are shown in gray. Projections of GaO_6 octahedra and GaO_4 tetrahedra are shown in black.

$CuCl_2$, $FeCl_2$, $MgCl_2$, $MnCl_2$, $NiCl_2$, and $ZnCl_2$). A blank sample, containing no salt additions, was also prepared.

BGR and rutile substrates were exposed to the DNA buffer solutions using several different application methods and imaged using atomic force microscopy. Initially, samples were prepared by exposing the substrates to 20 μl of DNA buffer solutions for 10 minutes. The sample surfaces were dried via wicking with filter paper, and compressed air. A second series of samples was first pretreated with a 10 mM divalent salt solution for 5 minutes, rinsed with distilled water, then exposed to 20 μl of DNA buffer solutions for 10 minutes before wicking and drying. For the third series of samples, 20 μl of DNA buffer solution was applied to BGR surfaces and allowed to dry completely prior to imaging. A fourth series was conducted, where the volume of buffer was reduced to 10 μl and applied to both salt-pretreated and untreated BGR surfaces. Following AFM imaging, the dried 10 μl samples were rinsed with distilled water and re-imaged.

Atomic force microscopy was performed using a Nanoscope IIIa instrument (Digital Instruments, Santa Barbara, CA). All imaging was collected in tapping mode using silicon cantilevers (122 μm long, Vecco Nanoprobe, Santa Barbara, CA) and a scan rate of 1.25 Hz. For each sample, an origin was selected and the surface was mapped with Cartesian coordinates. Mapping the sample surface allowed re-imaging of the same area following different surface treatments.

4.3. Results and Discussion

4.3.1. Beta-gallia rutile synthesis

To determine the heating conditions required to fabricate suitable BGR substrates, trials were conducted on two samples. The first BGR test sample (Sample A) was imaged after sequentially heating it at increasing temperatures ranging from 900 to 1350 ^{o}C for 24-96 hours, as shown in Figure 4.2. Intergrowth formation, as evidenced by the formation of lines along the $\{210\}_r$ planes, did not occur until the sample was heated at

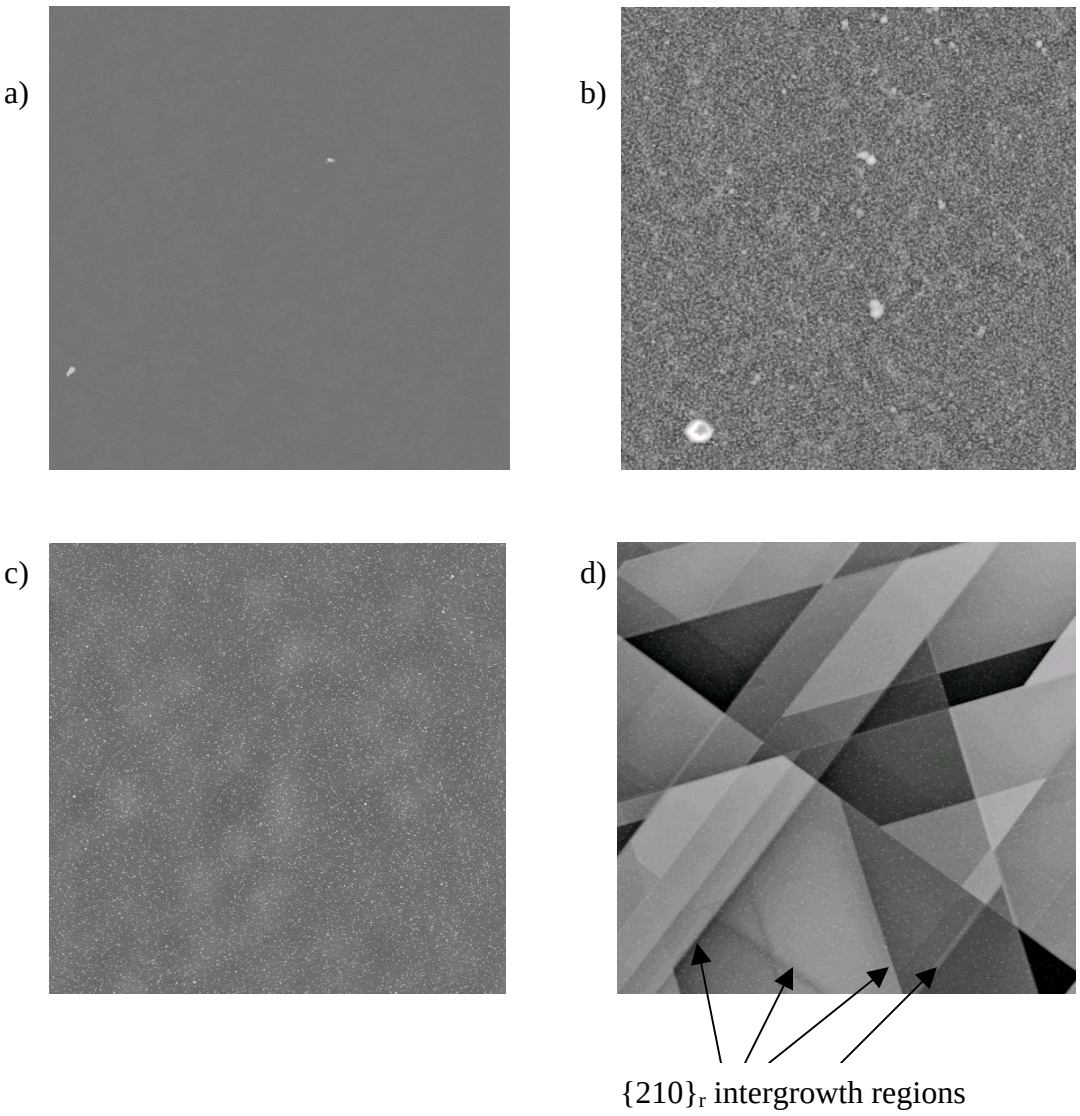

Figure 4.2. AFM height images (10 x 10 μm) of a) bare single crystal [001] TiO_2 (z range: 100 nm), b) BGR fired at 900 ^{o}C for 24 hrs (z range: 100 nm), c) BGR fired at 1100 ^{o}C for 24 hours (z range: 100 nm), d) BGR fired at 1350 ^{o}C for 96hrs (z range: 100 nm). No $\{210\}_r$ intergrowth regions were observed until reaching 1350 ^{o}C.

1350^{o}C. The chemistry of the BGR sample surface was confirmed using Auger electron spectroscopy. As shown in Figure 4.3, gallium was observed primarily along the $\{210\}_r$ intergrowth lines, which can also be observed by scanning electron microscopy. In general, the intergrowth lines were randomly oriented along $\{210\}_r$ planes, but in some regions, a relatively uniform parallel alignment of the intergrowth lines was observed (Figure 4.4). Parallel alignment was predominantly observed in areas adjoining surface cracks. The nature of the surface cracks is not well understood, but we speculate that elevated levels of gallium oxide deposited in the cracks may act as a continuous source of gallium oxide that promotes parallel orientation of the intergrowth lines. The micrographs in Figures 4.3 and 4.4 demonstrate the potential for achieving patterned arrangements of intergrowth lines on the BGR surface.

A second test sample (Sample B) was heated at 1350 ^{o}C and imaged by AFM at sequential periods of time. As illustrated in Figure 4.5, the relative density of observed intergrowth lines initially increased and then decreased with continued heating. The so-called relative density of intergrowth lines was determined by measuring the lengths of $\{210\}_r$ intergrowths in a 10 μm x 10 μm scanned area at eight different positions across the sample surface, averaging the measured lengths, and normalizing the data to that of the images with highest line density. Thus, the maximum line density is shown to be unity. The error bars in Figure 4.5 represent the standard deviation of the eight measurements made for each condition.

One possible explanation for the trend observed for Sample B (Figure 4.5) is that spin coating may initially produce an inhomogeneous distribution of Ga_2O_3 on the rutile surface. If this is the case, surface diffusion, which is generally faster than bulk diffusion, will dominate initially and result in an increase in the density of BGR intergrowth lines across the surface. As Ga_2O_3 becomes uniformly distributed across the surface, the driving force for surface diffusion will diminish; bulk diffusion will begin to dominate; and the density of intergrowth lines will decrease as Ga_2O_3 is transported into the bulk of the TiO_2 crystal. (The observed defects lines are the edges of defect planes which extend beneath the surface.)

Figure 4.5 also includes data from Sample A collected after it was heated at 1350 ^{o}C. In this graph, the first data point for Sample A is shown at 323 hours, corresponding

a)

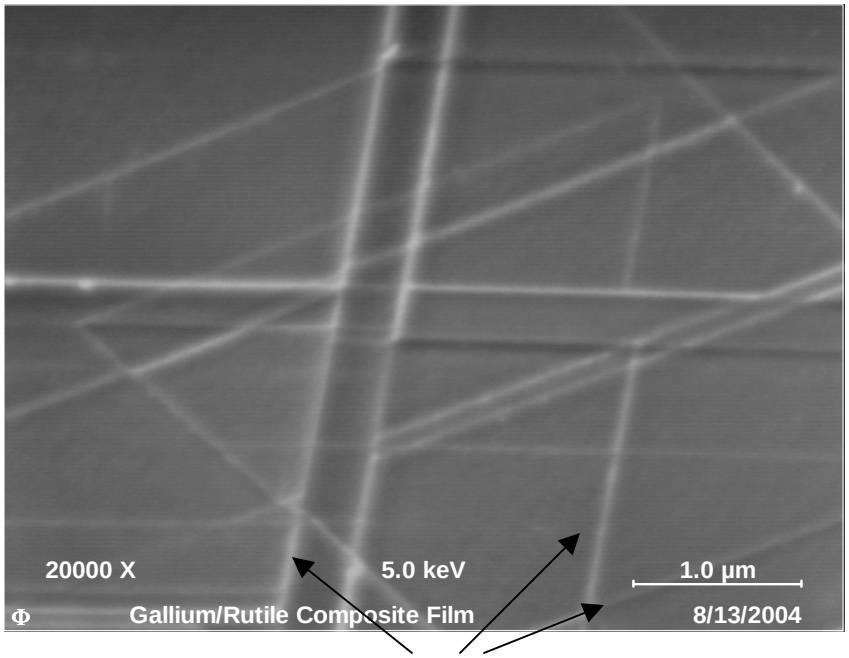

$\{210\}_r$ intergrowth regions

b)

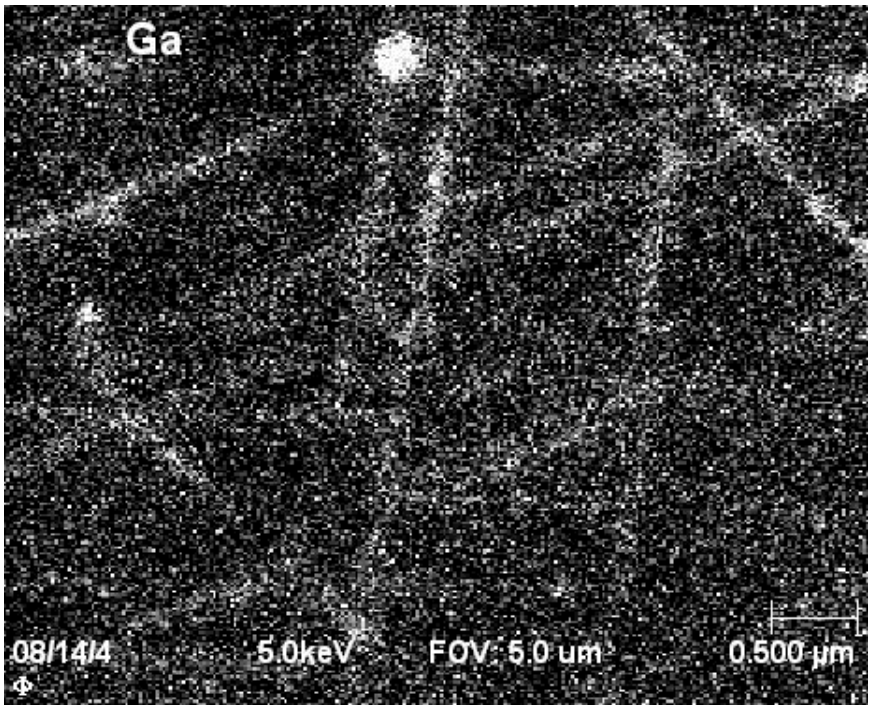

Figure 4.3. a) SEM micrograph of BGR surface, and b) Auger electron spectroscopy overlay of (a), which identifies presence of Ga (bright) residing along $\{210\}_r$ boundaries along [001] TiO_2 surfaces, confirming the surface chemistry.

a)

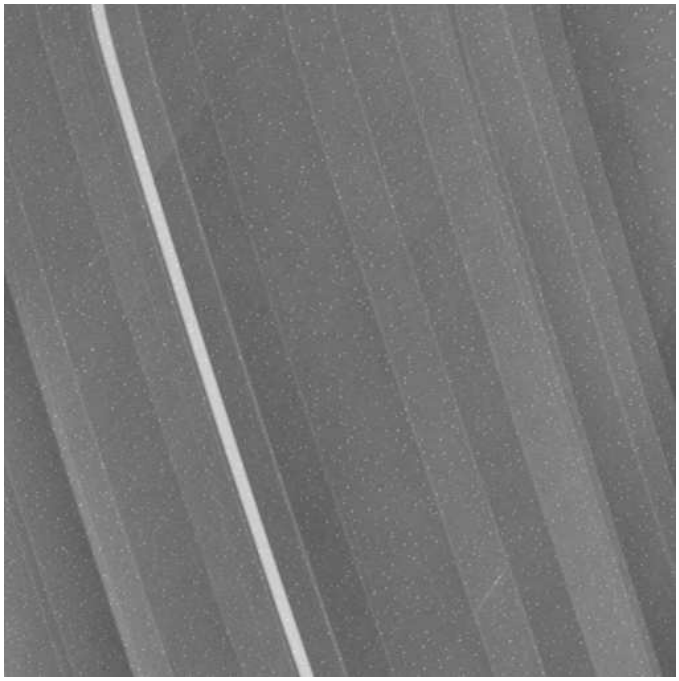

b)

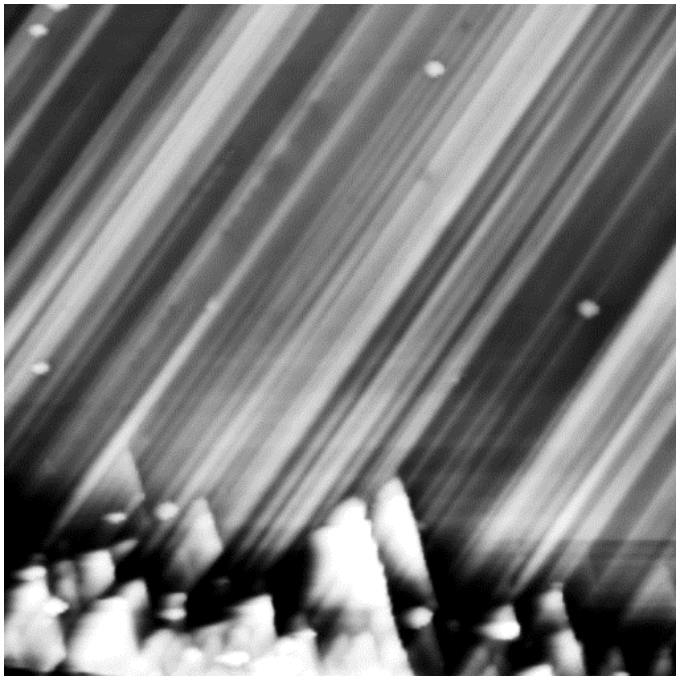

Figure 4.4. Preferential alignment of intergrowth boundaries observed in: a) AFM height image (10 x 10 μm) of BGR fired at 1350 ^{o}C for 96 hours (z range: 100 nm), b) AFM height image (10 x 10 μm) BGR fired at 1350 ^{o}C for 132hrs (z range: 100 nm).

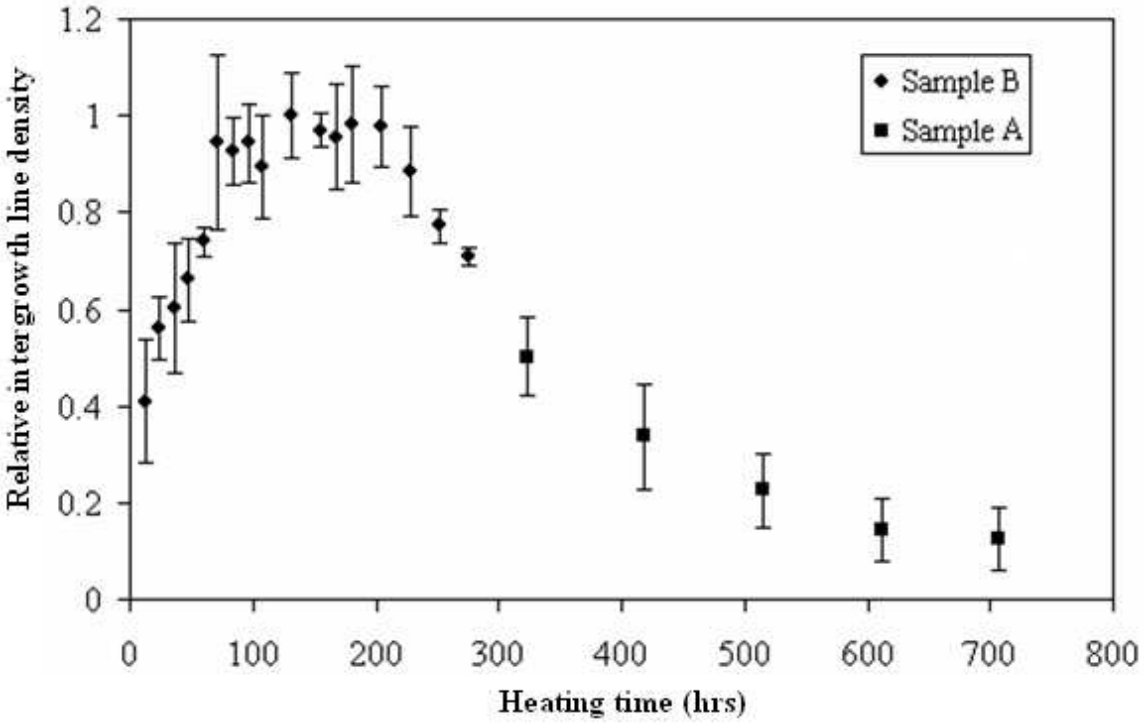

Figure 4.5. Relative $\{210\}_r$ line density as a function of heating time. Sample B was heated at 1350 ^oC. Sample A was initially heated at 900 – 1300 ^oC (data not shown), then heated at 1350 ^oC (data shown).

to 227 hours at temperatures between 900 ^{o}C and 1300 ^{o}C plus 96 hours at 1350 ^{o}C. Considering the difference in initial heating conditions of the two samples, one would not necessarily expect the data for Sample A to continue the trend observed for Sample B as is suggested by Figure 4.5. Nevertheless, the apparent agreement between the two data sets may reflect the role of surface diffusion in the early-stages of the process. Typically, surface diffusion has a relatively low activation energy compared to bulk diffusion, thus initially heating at different temperatures may not have significantly affected the rate at which Ga_2O_3 was distributed across the surface. Perhaps the most important observation regarding the data of Sample A is that the number of intergrowth lines appears to approach a constant level with increased heating, as is to be expected for diffusion from a finite thin-film source.

The majority of BGR substrates used for DNA attachment studies were fired at 900 ^{o}C for 3 hours, then at 1350^{o}C for 96 to 480 hrs. This resulted in substrates with an RMS roughness of ~ 1.5 nm, as determined by the average of several 2 x 2 μm AFM scans. This is approximately 5-6 times the roughness measured for bare mica substrates using the same technique.

4.3.2. DNA attachment studies

A number of different application methods were explored as a means of depositing DNA on BGR and [001]-rutile substrates. The results of these trials are summarized in Tables I and II.

BGR and rutile substrates were exposed to 20 μl of DNA buffer solutions for ten minutes and dried by wicking with filter paper and with compressed air. With the exception of BGR substrates exposed to Ni (II) solutions (Figure 4.6), attachment of DNA was too weak to allow AFM imaging. A second set of wicked samples was prepared in which substrates were pretreated for five minutes with the various salt solutions. Again, attachment was only observed on BGR substrates in the presence of Ni (II) cations. In both cases, DNA attached randomly on the BGR surface, showing no preference for the intergrowth regions. DNA did not attach to the rutile substrates. For

Table 4.I. Summary of DNA Attachment to BGR Surfaces

Amount of Solution Applied (μl)	Surface Exposure	Cation Addition	DNA Attached			
			Bare BGR	Bare BGR (Rinsed)	Pretreated BGR	Pretreated BGR (rinsed)
20	Wicked	none	no	--------	no	--------
20	Wicked	Ca (II)	no	--------	no	--------
20	Wicked	Co (II)	no	--------	no	--------
20	Wicked	Cu (II)	no	--------	no	--------
20	Wicked	Fe (II)	no	--------	no	--------
20	Wicked	Mg (II)	no	--------	no	--------
20	Wicked	Mn (II)	no	--------	no	--------
20	Wicked	Ni (II)	yes	trace	yes	trace
20	Wicked	Zn (II)	no	--------	no	--------
10	Dried	none	no	--------	no	--------
10	Dried	Ca (II)	no	--------	no	--------
10	Dried	Co (II)	yes	trace	yes	trace
10	Dried	Cu (II)	no	--------	no	--------
10	Dried	Fe (II)	no	--------	no	--------
10	Dried	Mg (II)	yes	trace	yes	trace
10	Dried	Mn (II)	yes	trace	yes	trace
10	Dried	Ni (II)	yes	yes	yes	yes
10	Dried	Zn (II)	yes	trace	yes	trace

Table 4.II. Summary of DNA Attachment to TiO_2 Surfaces

Amount of Solution Applied (μl)	Surface Exposure	Cation Addition	DNA Attached			
			Bare TiO_2	Bare TiO_2 (Rinsed)	Pretreated TiO_2	Pretreated TiO_2 (rinsed)
20	Wicked	none	no	--------	no	--------
20	Wicked	Ca (II)	no	--------	no	--------
20	Wicked	Co (II)	no	--------	no	--------
20	Wicked	Cu (II)	no	--------	no	--------
20	Wicked	Fe (II)	no	--------	no	--------
20	Wicked	Mg (II)	no	--------	no	--------
20	Wicked	Mn (II)	no	--------	no	--------
20	Wicked	Ni (II)	no	--------	no	--------
20	Wicked	Zn (II)	no	--------	no	--------
10	Dried	none	no	--------	no	--------
10	Dried	Ca (II)	no	--------	no	--------
10	Dried	Co (II)	no	--------	no	--------
10	Dried	Cu (II)	no	--------	no	--------
10	Dried	Fe (II)	no	--------	no	--------
10	Dried	Mg (II)	no	--------	no	--------
10	Dried	Mn (II)	no	--------	no	--------
10	Dried	Ni (II)	yes	trace	yes	trace
10	Dried	Zn (II)	no	--------	no	--------

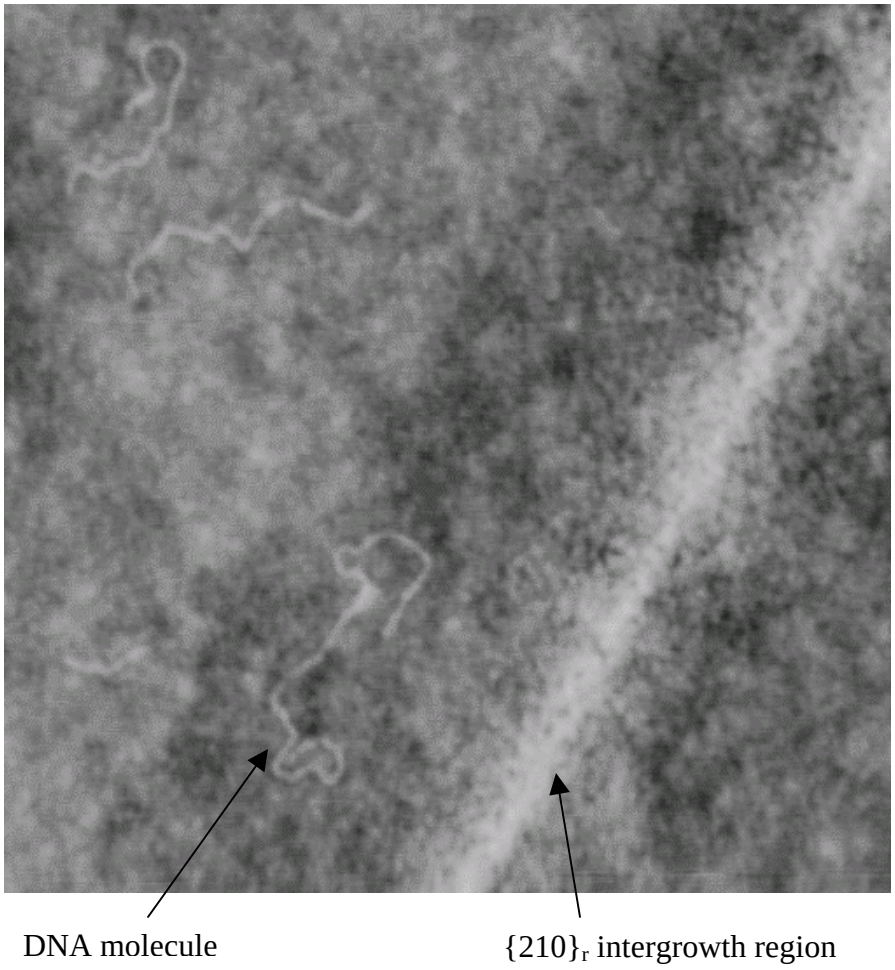

Figure 4.6. AFM height image (1 x 1 μm, z range: 10 nm) of DNA molecules bound to a BGR surface. The DNA / $NiCl_2$ buffer was exposed to the BGR surface for 10 minutes, then wicked with filter paper and allowed to dry.

most of the solutions examined, the force of attachment between the substrate and the DNA molecule was too small to overcome the forces of wicking. Additional experiments were prepared with solutions deposited for periods of 20 and 30 minutes prior to wicking, but similar results were obtained.

To allow a greater amount of time for DNA interaction with the surface and to avoid the forces associated with wicking, 20 μl aliquots of the DNA buffer solutions were allowed to dry completely on the BGR substrates. The dried 20 μl aliquot masked most of the BGR surface features and prevented imaging of DNA attachment, if any. Figure 4.7a shows the edge of the dried salt coating on the BGR surface. The samples were then gently rinsed with distilled water, allowed to dry and re-imaged. Little to no DNA was observed on these sample surfaces. Occasionally, DNA molecules were observed on the sample surface bound to surface irregularities, believed to be undissolved salt (Figure 4.7b). Portions not in direct contact with irregularities appear to be pulled in the direction of the receding meniscus, as shown in Figure 4.7b.

Next, the amount of DNA buffer solution applied to the substrates was reduced to 10 μl. Unlike the 20 μl trials, dried 10 μl aliquots allowed imaging of the underlying substrate. As shown in Figures 4.8a-e, DNA was bound strongly enough to the BGR surfaces in the presence of certain divalent cation salts ($CoCl_2$, $MgCl_2$, $MnCl_2$, $NiCl_2$ and $ZnCl_2$) to allow the imaging of the attached molecules. DNA molecules were not observed in systems when $CaCl_2$, $CuCl_2$, and $FeCl_2$ additions were incorporated. For TiO_2 substrates (both bare and pretreated), attachment of DNA to TiO_2 was only observed when buffers contained Ni (II) ions (Figure 4.9).

When using buffers with no salt additions (blanks), AFM images showed no evidence of attachment on bare or even salt-pretreated surfaces. In the absence of a divalent cation, the attachment force between DNA and the BGR surface was insufficient to withstand wicking, rinsing, and tip forces. The null result validates the importance of the salt additions in contributing to the attachment of DNA to the BGR surface.

To quantify whether or not DNA was preferentially attaching to $\{210\}_r$ intergrowth lines in the presence of divalent cations, the density of DNA molecules attached to $\{210\}_r$ intergrowth lines was compared to that of the density of DNA molecules crossing the equivalent length of lines drawn randomly across the AFM image.

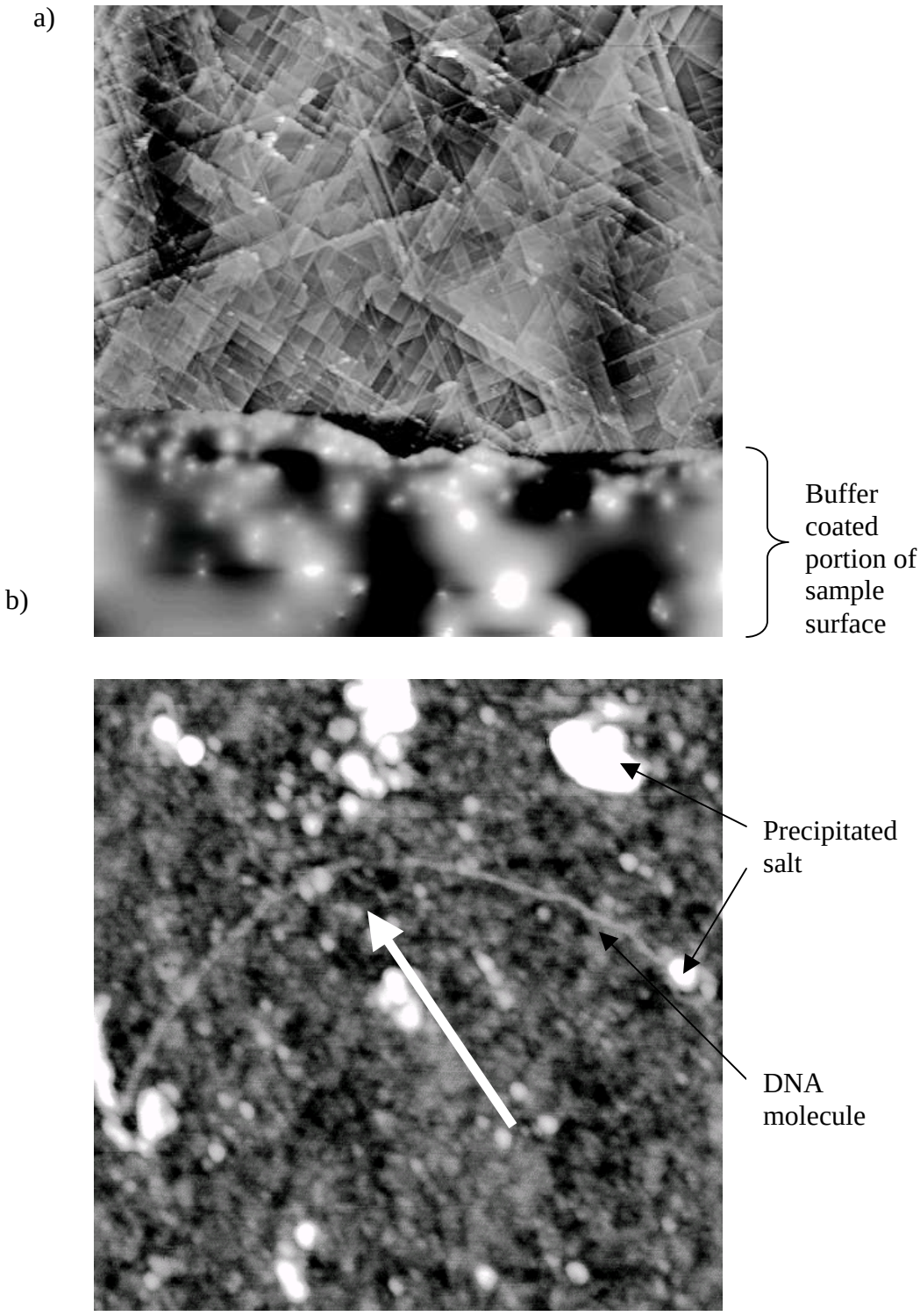

Figure 4.7. a) AFM height image (50 x 50 μm, z range: 300 nm) of the edge of a buffer coating on a BGR surface. b) AFM height image (900 x 900 nm, z range: 6 nm) of a washed BGR surface where DNA molecules have been pulled in the direction of a receding meniscus (white arrow).

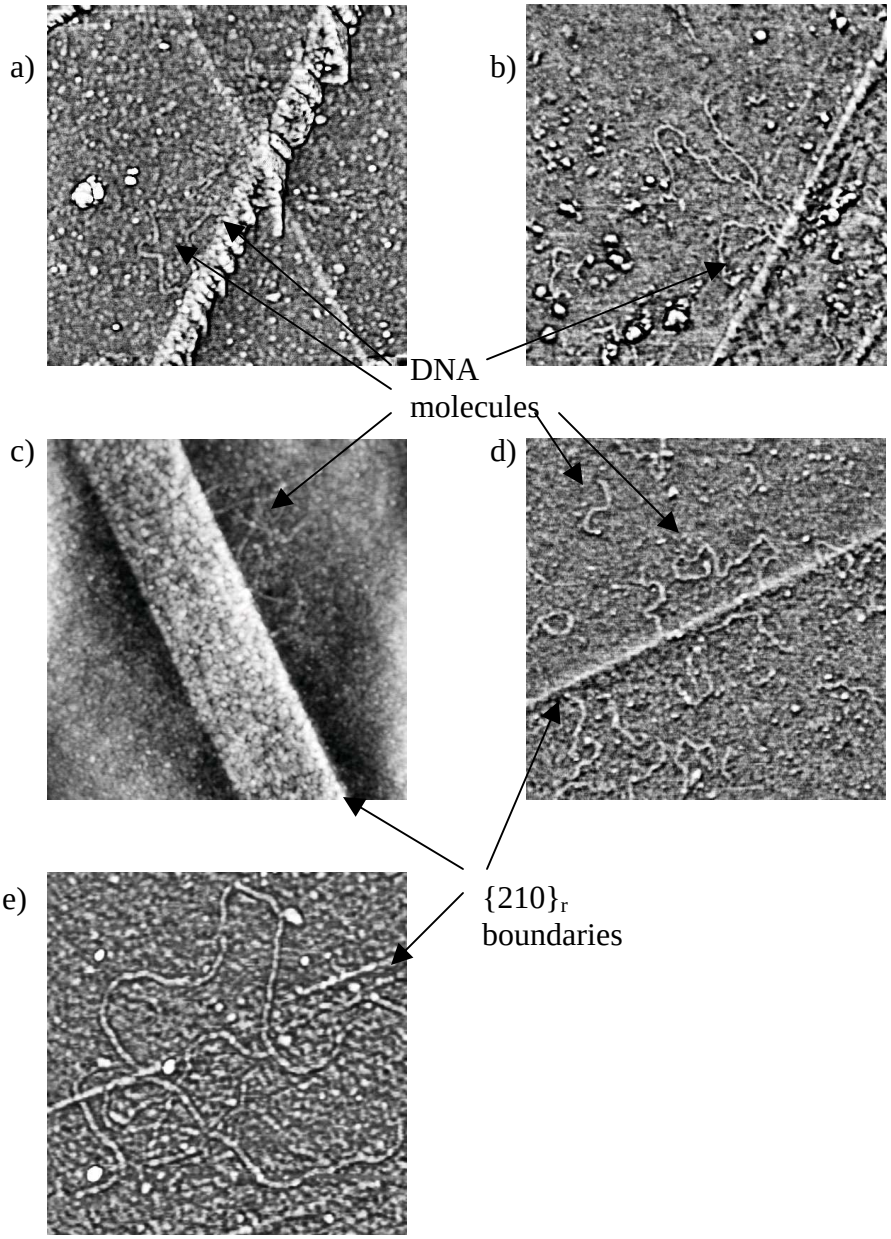

Figure 4.8. AFM images (1 x 1 μm) of DNA attached to BGR surfaces in the presence of a) Co (II) (phase image, z range: 35^{o}) b) Mg (II) (phase image, z range 40^{o}), c) Mn (II) (height image, z range: 10 nm), d) Ni (II) (phase image, z range: 30^{o}), and e) Zn (II) (phase image, z range: 80^{o}) cations.

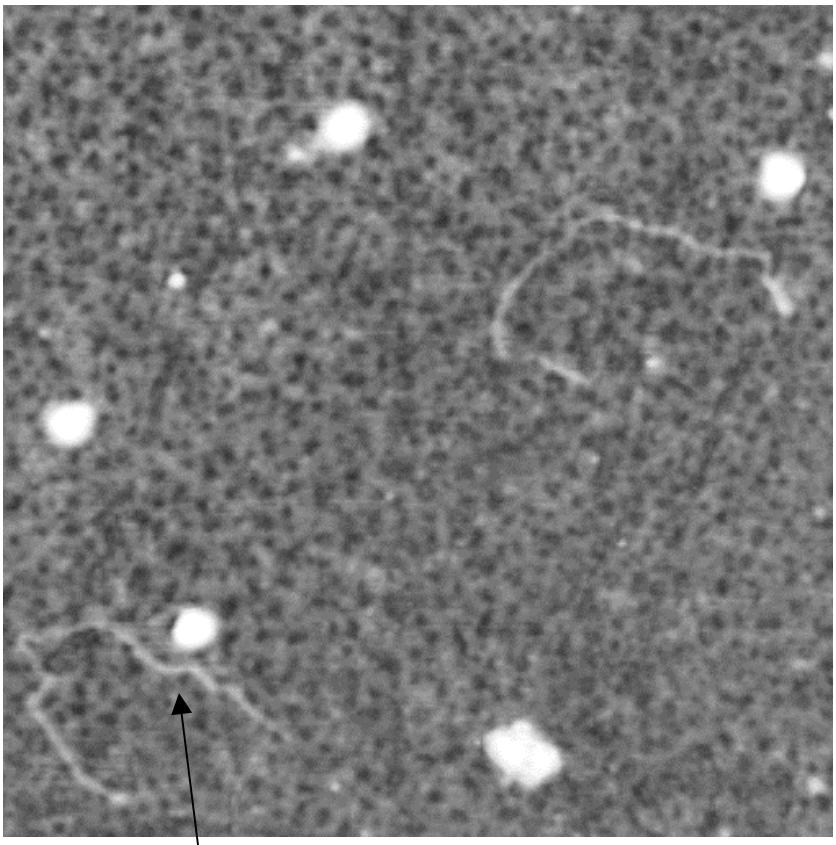

Figure 4.9. AFM image (1 x 1 μm) of DNA attached to a [001]-oriented single crystal TiO_2 surface in the presence of Ni (II) (height image, z range: 15 nm).

In this context, the density of DNA molecules is defined as the number of molecules per micrometer. The random lines were selected by placing an orthogonal grid with sequentially numbered grid lines, 1.25 mm apart, atop the AFM image and using a random number generator to pick an appropriate number of grid lines, along which DNA counting would be conducted. For each image, the random-line counting was repeated eight times and averaged. Intergrowth-line and random-line counts were made for all images collected and averaged to yield the results for the different cations examined. The number of images collected typically ranged from 20 to 30, except for those collected for Mn (II)-treated samples system where only 3 images were available for counting.

Figure 4.10 compares the average density of DNA counted along the $\{210\}_r$ lines to the average density counted along random lines in the AFM images. Significant variations are noted in the counted data, which can be attributed in part to problems associated with properly discerning long, single molecules of DNA from linked and/or aggregated smaller molecules. Moreover, the roughness of the substrate hindered the identification of DNA molecules in images with large scan sizes. Despite the large variations, we conclude that DNA attaches preferentially, although not exclusively, along the intergrowth lines since the density along intergrowth lines was consistently higher than that along the random lines for all of the cations that facilitated DNA binding to BGR surfaces, i.e. (Co (II), Mg (II), Mn (II), Ni (II) and Zn (II)). The two smallest two cations tested (Ni (II), and Mg (II)) yielded samples with the highest DNA densities, but there was no apparent relationship between the degree of preferential attachment and the size of the cations.

Of all the cations examined in this study, Ni (II) was the most effective in binding DNA to the substrate surfaces. Among the wicking trials on BGR substrates, only those prepared with Ni (II) salts showed evidence of DNA attachment. For dried samples, only those prepared with Ni (II) displayed a significant amount of DNA attachment after rinsing. Moreover, Ni (II) was the only cation tested that promoted significant DNA attachment to [001] TiO_2 substrates. The Ni (II) cation was also found to be the most effective in binding DNA to mica surfaces, which was attributed to the cation's size and relatively high hydration enthalpy.[14]

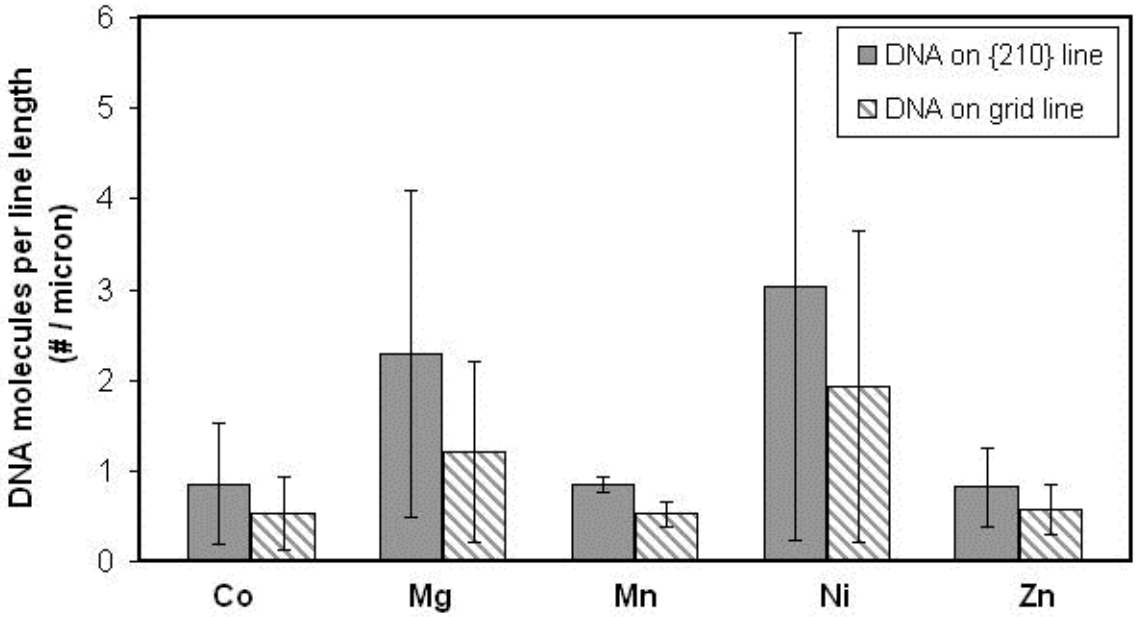

Figure 4.10. A comparison of the density of DNA attached to$\{210\}_r$ intergrowths (solid bars) to the density of DNA observed along random lines along the surface of BGR substrates (dashed bars) for different divalent cation. Data suggests a preference of DNA to attach along $\{210\}_r$ regions.

As mentioned previously, DNA attachment was not observed on BGR substrates when Ca (II), Cu (II), and Fe (II) were used as the divalent cation. Calcium (II) was the largest cation investigated in this study, with an ionic radius of 0.99 Å compared to a range of 0.69 - 0.83 Å for the other cations.[30] In studies of DNA attachment on mica, Hansma *et al.* reported similar results and suggested that Ca (II) was too large to occupy mica cavities.[14] Cu (II) and Fe (II) ions possess ionic radii within the range of cation radii observed to promote DNA binding to the BGR surface, suggesting that factors other than cation size influence attachment. Hansma *et al*. reported previously that buffers containing Cu (II) additions led to lumps of DNA instead of strands on mica surfaces.[14] Other studies have shown that Cu (II) and Fe (II) ions can cause chain mutation, cleavage, and denaturation;[31-35] all of which could negatively influence the molecules' ability to bind to a solid surface.

The mechanism(s) responsible for binding DNA to the BGR surface is not yet well understood. As mentioned previously, tunnel sites along the intergrowth lines are suitable hosts for small-to-medium sized cations. The preferential attachment of DNA at the observed intergrowth lines provides some evidence to support the notion that a divalent cation residing at the tunnel site may facilitate binding, e.g. via an electrostatic bridge as has been proposed previously.[14-16] It is interesting to note that, except for the deposition solutions containing Ni (II), DNA did not attach strongly enough to rutile substrates to allow imaging but was observed on the rutile portion of the BGR substrate. It is possible that isolated tunnel sites or very short intergrowth lines cannot be detected by AFM imaging and that the apparent binding on the rutile portion of the BGR actually involves a tunnel site, but more evidence is required to support this notion.

4.4. Conclusions

BGR intergrowth substrates suitable for DNA attachment studies can be prepared by spin-coating gallium isopropoxide onto [001]-oriented TiO_2 single crystal slabs and heating above 1350 ^{o}C. This generally results in the random orientation of intergrowth lines among different members of the $\{210\}_r$ family of planes. In some instances, the parallel alignment of the intergrowth lines was observed, but the factors that result in

such arrangements are not well understood. Further development of the process will be required to achieve controlled intergrowth arrangements, i.e. patterned substrates. Additionally, methods to achieve a flatter, smoother surface are desired.

The deposition of DNA on [001]-rutile and BGR surfaces from buffer solutions containing various divalent cations was studied. Of all the cations used, only Ni(II) facilitated the attachment of DNA on rutile, albeit in very small quantities. DNA attachment to BGR surfaces was strong enough to allow AFM imaging when the deposition buffer contained one of the following cations: Co (II), Mg (II), Mn (II), Ni (II), and Zn (II). For all of these cations, DNA attachment occurred preferentially, but not exclusively, along BGR intergrowth lines. When buffers without cation additions and those containing Ca (II), Cu (II) and Fe (II) were used, DNA failed to bind the BGR surfaces strongly enough to allow AFM imaging. The mechanism(s) by which DNA attaches to the BGR surface are not well understood, but may involve the incorporation of divalent cations at the tunnel sites of the BGR intergrowths.

4.5. References

1. L.M. Demers, D.S. Ginger, S.J. Park, Z. Li, S.W. Chung, and C.A. Mirkin, "Direct Patterning of Modified Oligonucleotides on Metals and Insulators by Dip-pen Nanolithography," *Science,* **296** [5574] 1836 (2002).

2. P.V. Schwartz, "Meniscus Force Nanografting: Nanoscopic Patterning of DNA," *Langmuir,* **17** [19] 5971-7 (2001).

3. Y. Yourdshahyan, H.K. Zhang, and A.M. Rappe, "N-alkyl Thiol Head-group Interactions with the Au (111) Surface," *Phys. Rev. B: Condens. Matter,* **63** [8] 081405 4pp (2001).

4. Z. Gueroui, "Immobilization and Stretching of DNA Molecules Above a Lithographed Surface," *Colloids Surf., B,* **33** [1] 53-6 (2004).

5. O. Medalia, J. Englander, R. Guckenberger, and J. Sperling, "AFM Imaging in Solution of Protein-DNA Complexes Formed on DNA Anchored to a Gold Surface," *Ultramicroscopy,* **90** [2-3] 103-12 (2002).

6. O. Pietrement, D. Pastre, F. Stephane, J. Jeusset, M. David, F. Landousy, L. Hamon, A. Zozime, and E. Le Cam, "Reversible Binding of DNA on $NiCl_2$-treated Mica by Varying the Ionic Strength," *Langmuir,* **19** [6] 2536-9 (2003).

7. J. Vesenka, M. Guthold, C.L. Tang, D. Keller, E. Delaine, and C. Bustamante, "Substrate Preparation for Reliable Imaging of DNA Molecules with the Scanning Force Microscope," *Ultramicroscopy,* **42-44** [2] 1243-9 (1992).

8. D. Pastre, O. Pietrement, S. Fusil, F. Landousy, J. Jeusset, M. David, L. Hamon, E. Cam, and A. Zozime, "Adsorption of DNA to Mica Mediated by Divalent Counterions: A Theoretical and Experimental Study," *Biophys. J.,* **85** [4] 2507-18 (2003).

9. H.G. Hansma, I. Revenko, K. Kim, and D.E. Laney, "Atomic Force Microscopy of Long and Short Double-stranded, Single-stranded and Triple-stranded Nucleic Acids," *Nucleic Acids Res.,* **24** [4] 713-20 (1996).

10. A. Sanchez-Sevilla, J. Thimonier, M. Marilley, J. Rocca-Serra, and J. Barbet, "Accuracy of AFM Measurements of the Contour Length of DNA Fragments Adsorbed on Mica in Air and in Aqueous Buffer," *Ultramicroscopy,* **92** [3-4] 151-8 (2002).

11. K. Rippe, N. Mucke, and J. Langowski, "Molecules in Motion: Imaging DNA with the Scanning Force Microscope in Aqueous Solutions," *Bioforum Intl.,* **1** [1] 42-4 (1997).

12. M. Bezanilla, S. Manne, D. Laney, Y. Lyubchenko, and H. Hansma, "Adsorption of DNA to Mica, Silylated Mica and Minerals: Characterization by Atomic Force Microscopy," *Langmuir,* **11** [2] 655-9 (1995).

13. T. Thundat, D.P. Allison, R.J. Warmack, G.M. Brown, K.B. Jacobson, J.J. Schrick, and T.L. Ferrell, "Atomic Force Micrsocopy of DNA on Mica and Chemically Modified Mica," *Scanning Microsc.,* **6** [4] 911-8 (1992).

14. H.G. Hansma and D.E. Laney, "DNA Binding to Mica Correlates with Cationic Radius: Assay by Atomic Force Microscopy," *Biophys. J.,* **70** [4] 1933-9 (1996).

15. S.J.T. van Noort, K.O. van der Werf, A.P.M. Eker, C. Wyman, B.G. de Grooth, N.F. van Hulst, and J. Greve, "Direct Visualization of Dynamic Protein-DNA Interactions with a Dedicated Atomic Force Microscope," *Biophys. J.,* **74** [6] 2840-9 (1998).

16. D. Stigter, "An Electrostatic Model for the Dielectric Effects, the Adsorption of Multivalent Ions, and the Bending of B-DNA," *Biopolymers,* **46** [7] 503-16 (1998).

17. C. Rivetti, M. Guthold, and C. Bustamante, "Scanning Force Microscopy of DNA Deposited onto Mica: Equilibration Versus Kinetic Trapping Studied by Statistical Polymer Chain Analysis," *J. Mol. Biol.*, **264** [5] 919-32 (1996).

18. C. Bustamante, M. Guthold, X. Zhu, and G. Yang, "Facilitated Target Location on DNA by Individual Escherichiacoli RNA Polymerase Molecules Observed with the Scanning Force Microscope Operating in Liquid," *J. Biol. Chem.,* **274** [24] 16665-8 (1999).

19. N. Empie and D. Edwards, "Phase Stability and Structure of Alkali Doped-beta-gallia Rutile Intergrowths," *Solid State Ionics,* **177** [1-2] 77-87 (2006).

20. L.A. Bursill, "Intersecting Defect Structures in Gallia- and Magnesia-doped Rutiles," *Acta Cyst.,* **A 35** [3] 449-58 (1979).

21. L.A. Bursill and G.G. Stone, "Tunnel and Intergrowth Structures in the Gallia-rich Gallium Titanate System," *J. Solid State Chem.,* **38** [2] 149-57 (1981).

22. R.M. Gibb and J.S. Anderson, "Electron Microscopy of Solid Solutions and Crystallographic Shear Structures II. Fe_2O_3-TiO_2 and Ga_2O_3-TiO_2 Systems," *J. Solid State Chem.,* **5** [2] 212-25 (1972).

23. A. Kahn, V. Agafonov, D. Michel, and M. Perez Y Jorba, "New Gallium Germanates with Tunnel Structures: alpha-Ga_4GeO_8 and $Ga_4Ge_3O_{12}$," *J. Solid State Chem.,* **65** [3] 377-82 (1986).

24. S. Kamiya and R.J.D. Tilley, "Phase Relations in the Pseudobinary System TiO_2-Ga_2O_3," *J. Solid State Chem.*, **22** [2] 205-16 (1977).

25. D.J. Lloyd, I.E. Grey, and L.A. Bursill, "The Structure of $Ga_4Ti_{21}O_{48}$," *Acta Cryst.*, **B32** [6] 1756-61 (1976).

26. G.G. Stone and L.A. Bursill, "High-resolution Electron Microscopy of (210) Defect Pairs in Gallia-doped Rutile," *Philos. Mag.*, **35** [7] 1397-412 (1977).

27. D.D. Edwards, T.O. Mason, W. Sinkler, L.D. Marks, K.R. Poeppelmeier, Z. Hu, and J.D. Jorgensen, "Tunneled Intergrowth Structures in the Ga_2O_3-In_2O_3-SnO_2 System," *J. Solid State Chem.*, **150** [2] 294-304 (2000).

28. G.V. Chandrashekar, A. Bednowitz, and S.J. La Placa, "A One Dimensional Sodium Ion Conductor," pp. 447-50 in *Fast Ion Transport in Solids.* Edited by P. Vashishta, J. N. Mundy, and G. K. Shenoy. Elsevier, New York, 1979.

29. Y. Li, A. Trinchi, W. Wlodarski, K. Galatsis, and K. Kalantar-Zadeh, "Investigation of the Oxygen Gas Sensing Performance of Ga_2O_3 Thin Films with Different Dopants," *Sens. Actuators*, **B 93** [1-3] 431-4 (2003).

30. R.D. Shannon, "Revised Effective Ionic Radii and Systematic Studies of Interatomic Distances in Halides and Chalcogenides," *Acta Cryst.*, **A 32** [5] 751-67 (1976).

31. L. Tkeshelashvili, T. McBride, K. Spence, and L. Loeb, "Mutation Spectrum of Copper-induced DNA Damage," *J. Biol. Chem.*, **266** [10] 6401-6 (1991).

32. W. Saenger, *Principles of Nucleic Acid Structure*. Springer-Verlang, New York, 1984.

33. G. Eichhorn and P. Clark, "Interactions of Metal Ions with Polynucleotides and Related Compounds, V. The Unwinding and Rewinding of DNA Strands Under the Influence of Copper (II) Ions," *Proc. Natl. Acad. Sci. U.S.A.*, **53** [3] 586-93 (1965).

34. G.L. Eichhorn and Y.A. Shin, "Interaction of Metal Ions with Polynucleotides and Related Compounds. XII. The Relative Effect of Various Metal Ions on DNA Helicity," *J. Am. Chem. Soc.*, **90** [26] 7323-8 (1968).

35. P. Rai, D. Wemmer, and S. Linn, "Preferential Binding and Structural Distortion by Fe^{2+} at RGGG-Containing DNA Sequences Correlates with Enhanced Oxidative Cleavage at Such Sequences," *Nucleic Acids Res.*, **33** [2] 497-510 (2005).

5. The Attachment of DNA to Beta-Gallia Rutile Surfaces as a Function of DNA Solution Age.

Abstract

Beta-gallia rutile (BGR) substrates provide surfaces capable of preferentially binding DNA along $\{210\}_r$ intergrowth boundaries when in the presence of certain divalent cations. The site-specificity of binding and tailor-ability of the separation and orientation of $\{210\}_r$ boundaries could enable BGR surfaces to be used as substrates for nano-electronic, biologic, and mechanical devices. DNA solutions containing additions of different divalent cations and varied aging were deposited on BGR surfaces, which were then scanned with the atomic force microscope. A dramatic decrease in the concentration of DNA bound to BGR surfaces was observed as the DNA solution age increased. Aged DNA solutions also failed to yield significant bands when evaluated with gel electrophoresis. The results suggest that DNA solution age is an important variable influencing DNA attachment to BGR surfaces.

5.1. Introduction

Large scale-development and processing of bottom-up approaches to nano-molecular-devices require unique substrates that are capable of being quickly, reproducibly, and controllably patterned at the nanoscale.[1,2] In addition, the patterned regions will need to possess a predilection to attach molecules selectively in a tunable manner. A number of current methods to generate patterned surfaces involve lithographic and probe-based techniques, which can be too expensive, cumbersome, or time consuming to adequately scale up.[3-7] We are investigating the capability of beta-gallia rutile (BGR) intergrowth structures to serve as substrates possessing inherent pattern-ability of regions able to preferentially attach DNA (Figure 5.1).

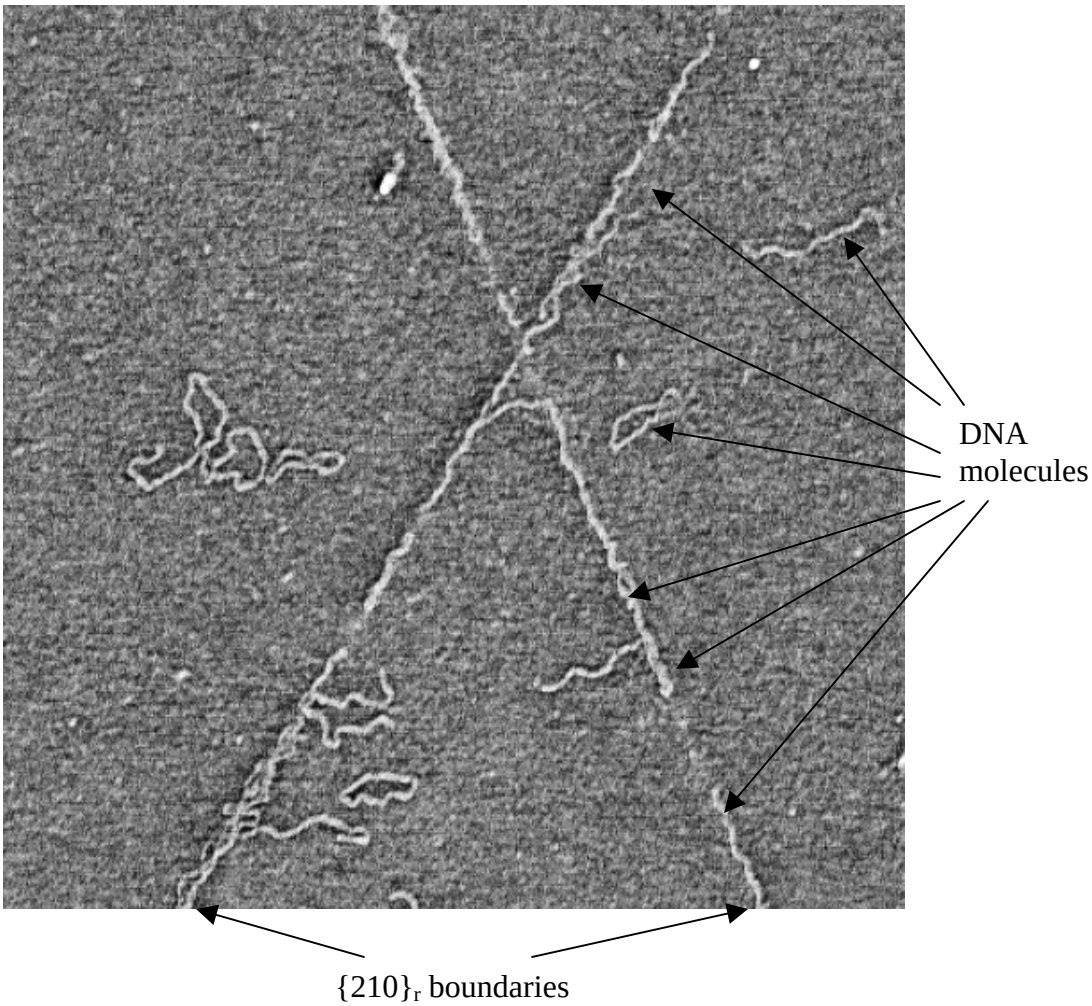

Figure 5.1. a) AFM phase image (1.75 x 1.75 μm, z-range: 15^{o}) demonstrating the preferential attachment of DNA along $\{210\}_r$ intergrowth boundaries of a BGR surface. DNA solution contained 5mM addition of $MgCl_2$.

Beta-gallia rutile possesses a controllable surface structure governed by the formula: $Ga_4Ti_{n-4}O_{2n-2}$ (where n is 9-51 and odd).[8-15] When gallia diffuses into [001]-oriented rutile, beta-gallia subunits insert selectively along $\{210\}_r$ planes. The lattice mismatch between the two crystal structures leads to the formation of one dimensional tunnels aligned along $\{210\}_r$ and running perpendicular to the rutile surface. Figure 5.2 is an AFM image and accompanying polyhedra model of a BGR structure. Increasing or decreasing the ratio of gallium to titanium (the n value), alters the distance separating the rows of tunnel-rich beta-gallia regions providing the tailor-ability to the BGR substrate.

The tunnel sites found along the $\{210\}_r$ boundaries of BGR surfaces are approximately 2.5 Å in diameter, appropriate for a small to medium sized cation to occupy. We have observed that DNA molecules preferentially bind along the $\{210\}_r$ boundaries and speculate that the attachment is facilitated by the insertion of divalent cations in the tunnel sites.[16] A similar interaction is observed when DNA binds to mica surfaces utilizing divalent cations, but here too the nature of binding is not completely understood.[17-27]

Understanding the binding interaction is the key to the development of controllable DNA attachment to suit a given application. A recent study described stronger DNA to BGR binding behavior when DNA buffered solutions contained Ni (II) cations instead of Co (II), Mg (II), and Zn (II).[16] Data obtained from this previous study possessed a considerable degree of variation, perhaps suggesting an ignored factor(s) was influencing the interaction. The focus of this study is to investigate the influence DNA solution age has on the attachment of DNA to BGR surfaces. A better understanding of the variables controlling this interaction could lead to the development of a substrate capable of supporting micro- and nano-scaled molecular constructs.

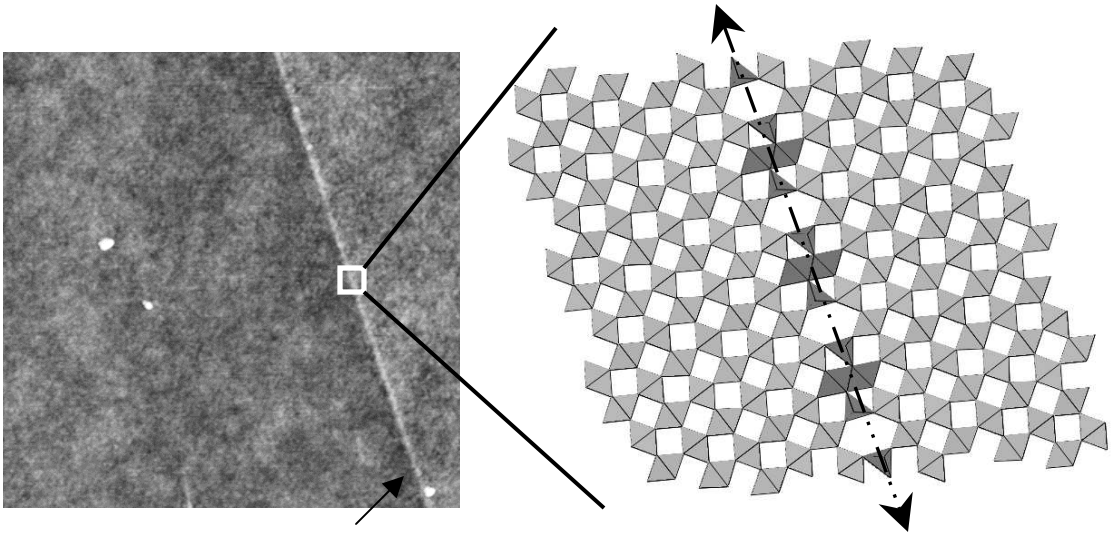

Figure 5.2. a) AFM image (1.2 x 1.2 μm, z-range: 10 nm) of a bare BGR surface. Bright linear region is a $\{210\}_r$ intergrowth region. b) Projection of the outlined section (in 'a') of the BGR structure along [001] of parent rutile. Two-dimensional projections of TiO_6 octahedra are shown in gray. Projections of GaO_6 octahedra and GaO_4 tetrahedra are shown in black (residing along $\{210\}_r$ shear planes). Dashed line represents a $\{210\}_r$ boundary along which cations (and subsequently DNA) are preferentially bound to hexagonal tunnel sites.

5.2. Experimental Procedure

5.2.1 Synthesis of beta-gallia rutile substrates

To prepare the BGR substrates, a 0.15 M gallium-isopropoxide solution[28] was applied to single crystal, [001]-oriented, TiO_2 substrates (5 x 5 x 0.5 mm) (MTI corp, Richmond, CA) via spin coating for 25 seconds at 2500 rpm (application repeated four times). The coated substrates were dried for 24 hrs prior to heating. Samples were heated at 900^{o}C for 3 hrs, then at 1350^{o}C for 48 hrs. The BGR surfaces were pretreated with a 10 mM chloride solution (containing the appropriate divalent cation) for 1 min.; then rinsed with distilled water.

5.2.2. AFM imaging

The samples were characterized, in air, using a Nanoscope III AFM (Digital Instruments, Santa Barbara, CA) in tapping mode. The microscope was equipped with silicon probes (Ted Pella, Inc., Redding, CA) operated at frequencies between 200 and 500 kHz. The cantilevers were 125 μm long with a force constant of 40 N / m. Sample surfaces were mapped with Cartesian coordinates to provide successive scanning of equivalent spatial locations following various surface treatments.

5.2.3. DNA solution preparation

A 100 μg / ml solution of monosized, 1000bp, ds-DNA was obtained from Gensura Laboratories, Inc (San Diego, CA) and diluted to 0.5 μg / ml in 10mM HEPES (4- (2-Hydroxyethyl) piperazine-1-ethanesulfonic acid) buffer, pH 7, and 0.1, 1.0, or 5.0 mM $CoCl_2$, $MgCl_2$, $NiCl_2$, or $ZnCl_2$. All prepared DNA solutions were stored in Nalgene® Cryoware™ sterile cryogenic vials (Rochester, NY). A 2 μl aliquot of the DNA / salt solution (aged at room temperature for times ranging from a few hours to a few months) were applied to BGR substrates, allowed to dry, and visualized with the AFM in tapping mode.

5.2.4. Reporting bound DNA concentration

Because DNA molecules exhibit preferential attachment for $\{210\}_r$ intergrowth regions of BGR surfaces, it would be inappropriate to report surface DNA densities when different surface regions possess different densities of $\{210\}_r$ intergrowth lines. Instead we will compare the average linear DNA density along $\{210\}_r$ boundaries. This value is calculated by taking the number of DNA molecules in contact with $\{210\}_r$ intergrowth boundaries and dividing by the images' total $\{210\}_r$ boundary length (value expressed in molecules per micron). An equivalent length of random grid lines (selected via a random number generator) was applied to each image (average of 10 trials / image), and termed the linear DNA density along random grid lines. Dividing each images' linear DNA density along $\{210\}_r$ lines by the density along random grid lines yields the degree of preference for $\{210\}_r$ regions.

5.2.5. Gel electrophoresis

DNA buffered solutions ranging from 1 hour to 1 year in age (storage at room temperature unless otherwise specified) were separated in E-Gel® (2% with SYBR Safe™) pre-cast agarose gels (Invitrogen™ Carlsbad, CA) run at 70 V for 30 min. The gels were then visualized using a UV transilluminator.

5.3. Results and Discussion

5.3.1. AFM results and discussion

The attachment of DNA to BGR surfaces was significantly influenced by the age of the solution applied. For all cation species, at all cation concentrations, DNA solutions applied to BGR surfaces within one day of solution synthesis exhibited dramatically higher densities of bound DNA (Figure 5.3). Visually such differences were easily observed when comparing AFM scans of surfaces exposed to various ages of DNA solution (Figure 5.4). The relationship between solution age and the average degree of

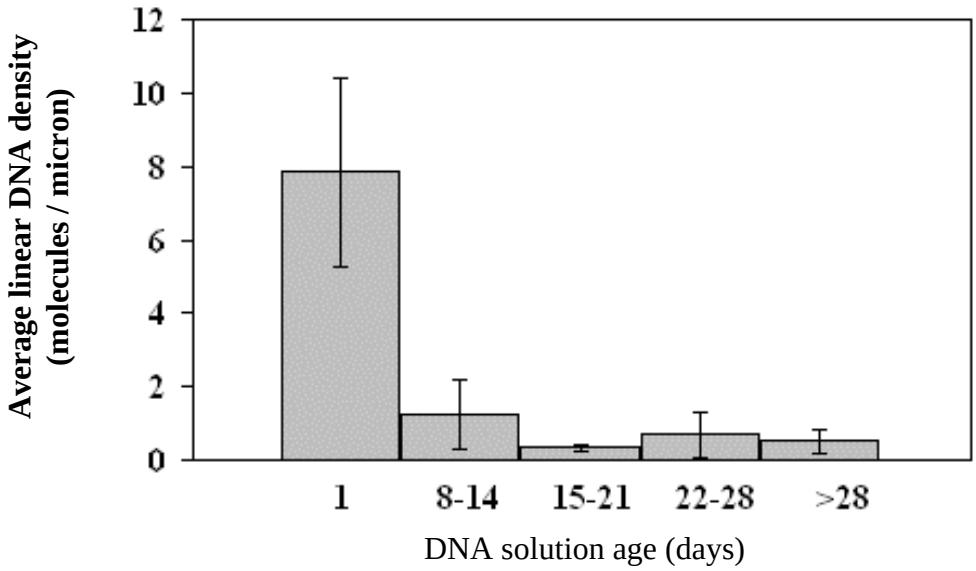

Figure 5.3. Average linear DNA density along $\{210\}_r$ intergrowth boundaries as a function of DNA solution age. A significant decrease in quantity of bound DNA molecules was observed for samples stored at room temperature longer than a week prior to application.

a)

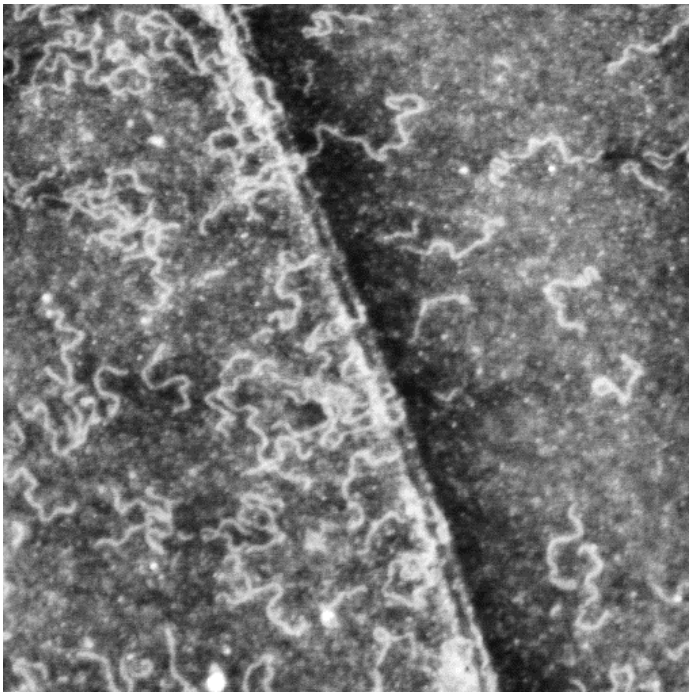

b)

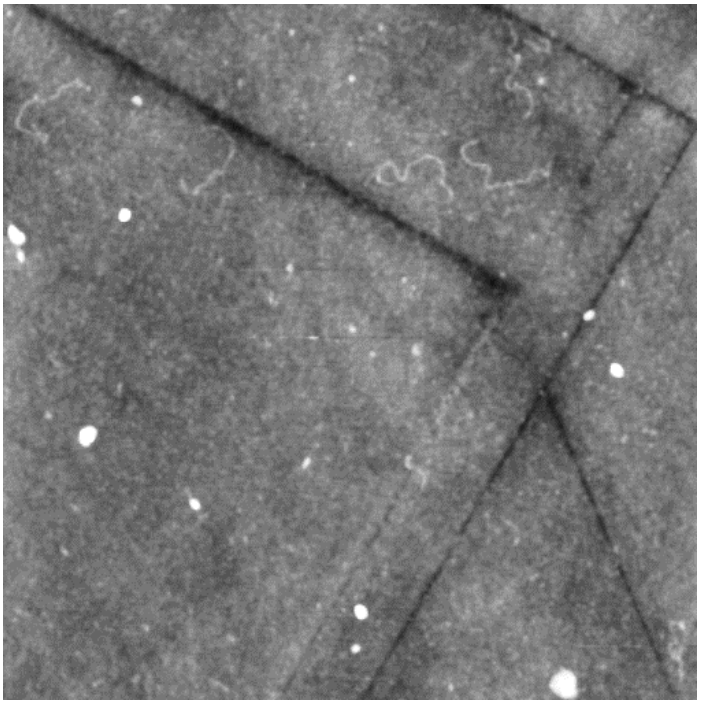

Figure 5.4. AFM scans (1.5 x 1.5 μm, z-scale 10 nm) of BGR surfaces exposed to DNA solutions containing additions of 1 mM $CoCl_2$ at a buffer age of: a) 1 day, and b) 42 days. As the age of the DNA buffer is increased, there is a considerable decrease in the density of bound DNA molecules.

preferential attachment of DNA to $\{210\}_r$ boundaries is displayed in Figure 5.5. The preference for $\{210\}_r$ is exhibited throughout all solution ages (degree of preference >1); however, there appears to be a slight decrease in the average degree of preference as solution age increases, but due to the variance in the data, a significant result cannot be identified.

The average linear $\{210\}_r$ DNA density of solutions prepared with 1 mM MCl_2 (M = divalent cation) both ignoring (checkered bars), and considering solution age (by separating 1 day solutions (solid bar) from solutions with an age greater than 1 day (dashed bar)) are presented in Figure 5.6. When ignoring the age effect, deviations within the data are on the order of the actual average values. Separating data points taken within one day of DNA solution preparation, led to significant decreases in the standard deviations, as well as significant changes in the average linear DNA densities within each group.

Previously, we reported superior DNA binding when buffered solutions contained additions of Ni (II) cations compared to other divalent cations.[16] However, these DNA solutions containing Ni (II) additions were applied to surfaces within 1-2 weeks, whereas samples containing other divalent cations were applied at longer times after solution synthesis (~2-4 weeks). Based on the results of our current study, the increased attachment of DNA in the presence of Ni (II) cations could be attributed to the solution age. It was previously described that only Ni (II) cations were able to sufficiently bind DNA to withstand a rinsing procedure; however, in this study DNA was observed to remain bound, post rinsing, when using a solution less than one week old with the addition of 1 mM $MgCl_2$ (Figure 5.7). In both situations, the density of bound DNA is reduced following the rinsing step.

5.3.2. Gel electrophoresis results and discussion

Photographs of gel-electrophoresis are shown in Figures 5.8 and 5.9. Figure 5.8 displays a gel run with solutions containing solely $MgCl_2$ additions. Lanes 1 and 5 contain a standard 1000-bp fragment DNA quantitation standard (0.5, and 1.0 μl / ml DNA in 10mM HEPES, pH 7 respectively) with no salt addition, prepared ~ 3 weeks

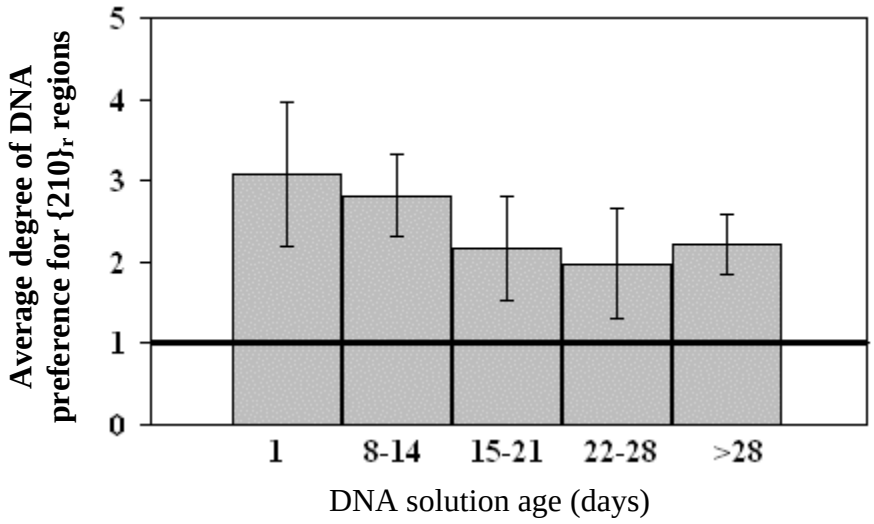

Figure 5.5. Average degree of DNA preference for $\{210\}_r$ intergrowth boundaries as a function of DNA solution age. Solutions at all tested ages showed a preference for $\{210\}_r$ boundaries (average degree >1 (black horizontal line)). A slight decrease in preference with respect to solution age is observed, but the variation within the data is too large to verify the trend.

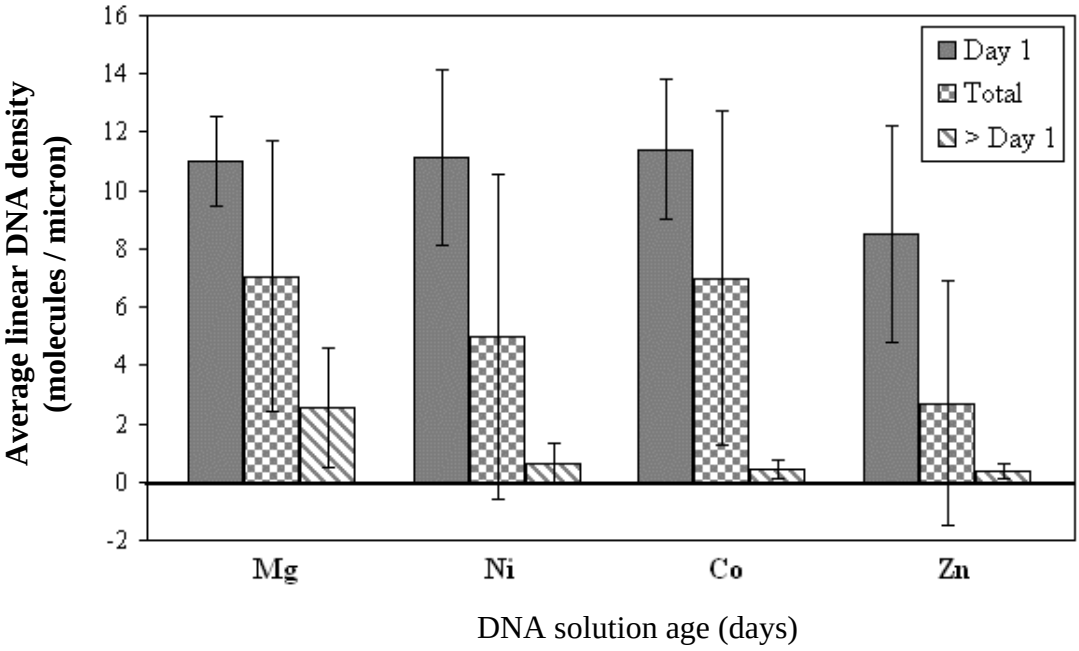

Figure 5.6. Average linear DNA density along $\{210\}_r$ intergrowth boundaries as a function of DNA solution (containing 1 mM MCl_2) age. The significant variability of the original data (checkered columns) is dramatically reduced by separating the data collected with fresh solutions (solid grey columns) from older solutions (striped columns). The difference in the averages of the separated data supports the significance of treating solution age as a variable.

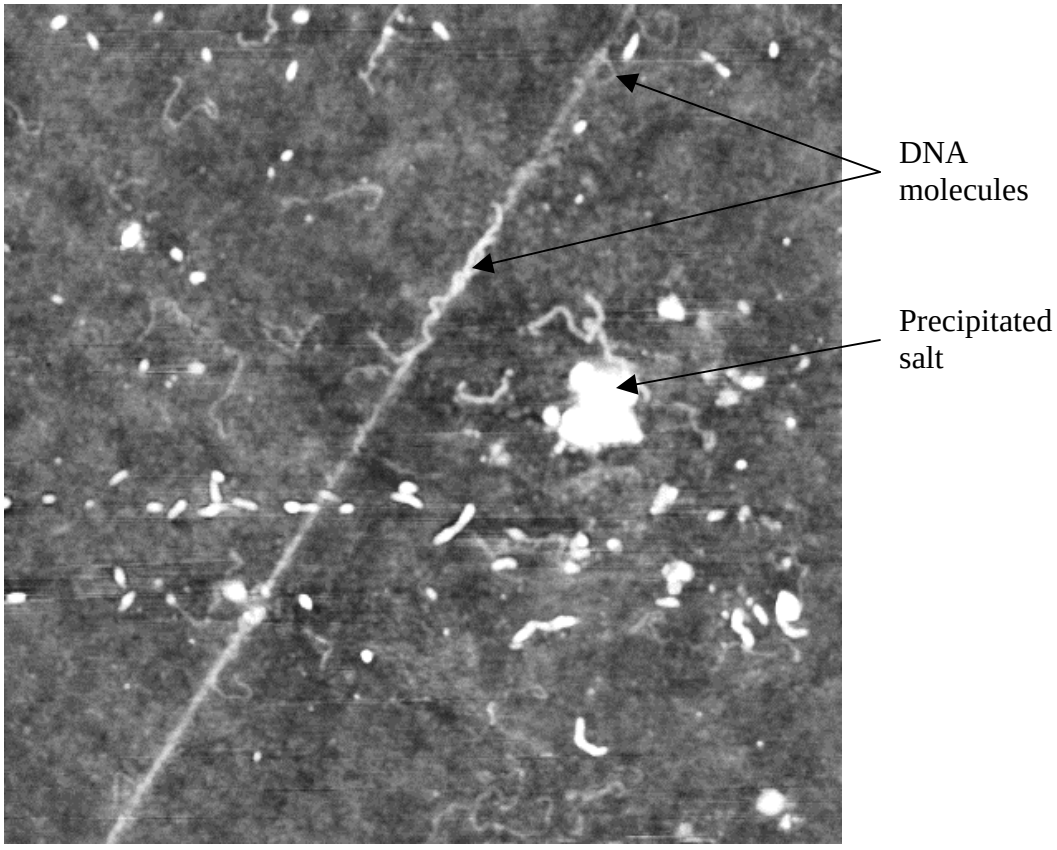

Figure 5.7. AFM image (2 x 2 μm scan, z-scale: 8 nm), post rinsing, of a freshly prepared DNA solution containing 5 mM $MgCl_2$ dried to a BGR surface. DNA molecules are still present after the rinsing procedure.

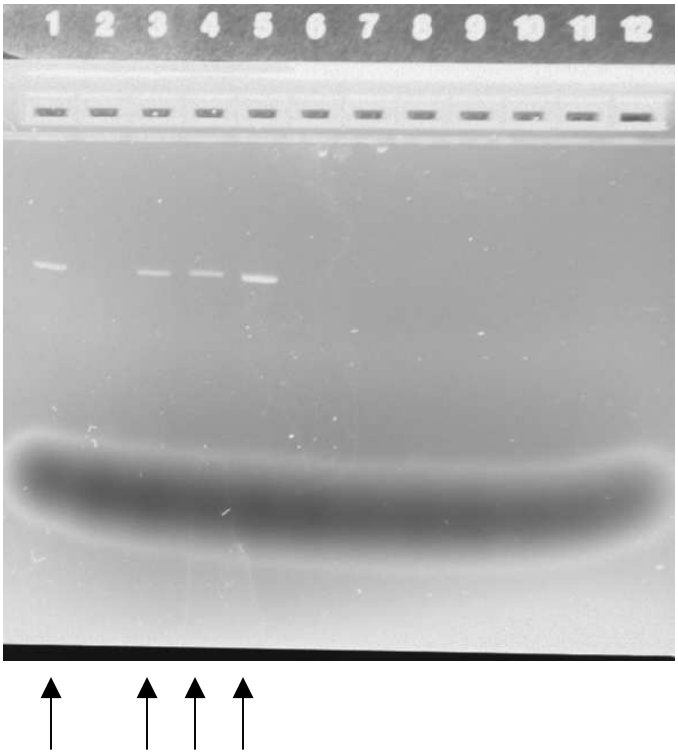

Figure 5.8. Electrophoresis gel of new and aged DNA solutions containing additions of $MgCl_2$. Only lanes containing freshly prepared DNA solutions exhibited significant enough concentrations of DNA to be detected.

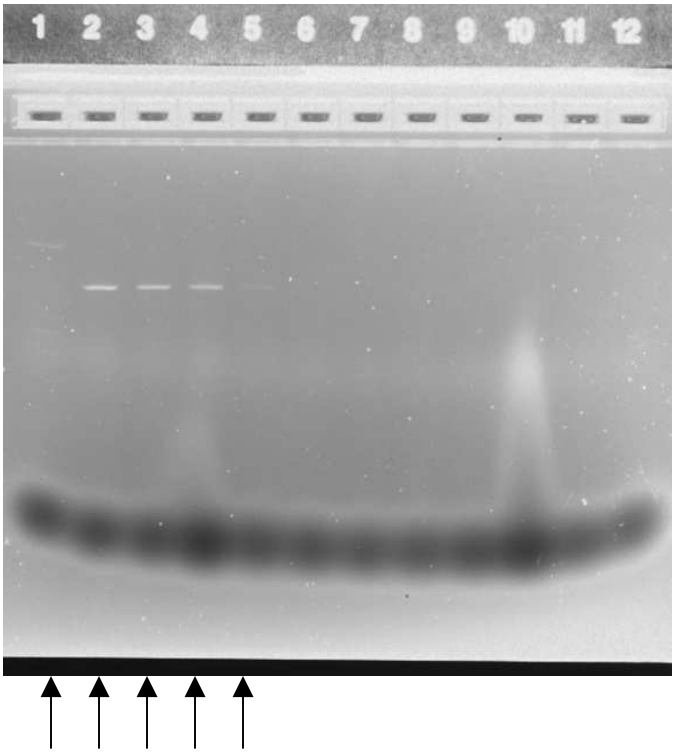

Figure 5.9. Electrophoresis gel of new and aged DNA solutions containing additions of $NiCl_2$. Only lanes containing freshly prepared DNA solutions exhibited significant enough concentrations of DNA to be detected.

prior to electrophoresis, but stored in a freezer at 4^{o}C until use. Lanes 2-4 contain freshly prepared DNA solutions with 0.5, 1.0, and 5.0 mM $MgCl_2$. Lane 6 contains a standard 1000-bp DNA standard (0.5 μl / ml) with no addition, prepared ~8 month prior to electrophoresis, and stored at room temperature. Lanes 7-9, and 10-12 contain solutions possessing increasing concentrations of $MgCl_2$ prepared ~8 and ~6 months prior to electrophoresis, and stored at room temperature.

Samples run in Lanes 1, 5, and 6 contain no salt additions. The increase in band intensity from 1 to 5 is the result of the higher DNA concentration. The absence of a band for sample 6 suggests that prolonged solution storage at room temperature has lead to DNA degradation. Similar results were observed when comparing freshly prepared samples (Lanes 2-4) to aged samples (7-12). Bands present for freshly prepared solutions with $MgCl_2$ additions of 1 and 5 mM (Lanes 3 and 4 respectively) match with the 1000-bp standard (lane 1) whereas no positive band is observed for Lanes 7-12.

Results obtained from DNA solutions containing $NiCl_2$ additions can be observed in Figure 5.9. Lane 1 contains a 100-bp ladder solution (0.5 μl / ml DNA in 10mM HEPES, pH 7) with no salt addition, prepared ~ 1 year prior to electrophoresis, but stored in a freezer at 4^{o}C until use. Lane 2 contains a standard 1000-bp fragment DNA quantitation standard (0.5 μl / ml DNA in 10mM HEPES, pH 7 respectively) with no salt addition, prepared ~ 3 weeks prior to electrophoresis, but stored in a freezer at 4^{o}C until use. Lanes 3-5 contain freshly prepared solutions of standard 1000-bp DNA fragments containing additions of 0.5, 1.0, and 5.0 mM $NiCl_2$. Lanes 6-8, and 9-11 contain solutions possessing increasing concentrations (0.5, 1.0, and 5.0) of $NiCl_2$, prepared ~8 and ~6 months (respectively) prior to electrophoresis, and stored at room temperature. Lane 12 contains a solution possessing the addition of 5 mM $NiCl_2$ prepared ~3 months prior to electrophoresis, and stored at room temperature. The 100-bp ladder DNA is expressed as a series of faintly observed bands in Lane 1.

Similar to results obtained from the previous electrophoresis sample, only freshly prepared solutions displayed the 1000-bp band. An interesting difference observed between the two gels, is the fainter band in Lane 5 corresponding to the DNA solution containing 5.0 mM $NiCl_2$ concentration. Typically the intensity of bands corresponds to the density of DNA present within the sample (as displayed in Lanes 1 and 5 (0.5 and 1.0

μg / ml respectively) of Figure 5.8), so a fainter band would suggest less DNA. Comparing images obtained via AFM (Figure 5.10 a, b) the conformation of DNA is altered by the increase in the concentration of $NiCl_2$. The molecules bound with additions of 0.5 mM $NiCl_2$ appear loosely bound, possibly outstretched by the force of a receding meniscus; whereas the molecules bound at 5 mM $NiCl_2$ possess a collapsed conformation. Additionally, an increase in precipitated salt (bright spots in AFM images) was also observed when increasing solution salt concentration. The reduced conformations and presence of precipitated salt could lead to a fainter band, as both conditions may influence the ability of DNA molecules to travel through the gel, via formation of DNA aggregates. Within $MgCl_2$ containing solutions the conformation of DNA bound in the presence of Mg (II) ions did not appear to be as significantly affected as those exposed to $NiCl_2$; nor was an increase in salt precipitation as significant in samples studied with supplements of $MgCl_2$.

Metal cations have been shown to form water insoluble hydroxides at alkaline pH, or at sufficiently high cation concentrations at neutral pH.[26,29] Hydroxides of transition metal cations possess lower solubilities than those formed with alkaline earths, [30] which supports the greater occurrence of precipitates observed from samples prepared with Ni (II) additions compared to Mg (II). Kejnovosky and Kypr observed strong sedimentation of DNA in solutions exposed to 10 mM concentrations of transition metal chlorides (of Zn (II), Mn (II), Co (II), Ni (II)), while solutions prepared with Mg (II), Ca (II) and Ba (II) chlorides contained no detectable amounts of DNA in the sediment (solutions were incubated for 20 min. prior to centrifugation).[29] The amount of DNA in the sediment was shown to increase with cation concentration and pH, with >90% of the DNA existing in the sediment with zinc and manganese chlorides at a concentration of 10mM and a pH > 8.[29] Observing Figure 5.10b, nearly every DNA molecule bound on the BGR surface appears to be in contact with precipitated salt, confirming a strong interaction between the two species. These results suggest that the weaker band observed at 5 mM $NiCl_2$ could be attributed to DNA sedimentation.

Electrophoresis results from aged DNA solutions possess insufficient concentrations to yield bands. DNA aggregation or sedimentation could have contributed to the null result. Occasionally while imaging dried DNA solutions on BGR surfaces

a)

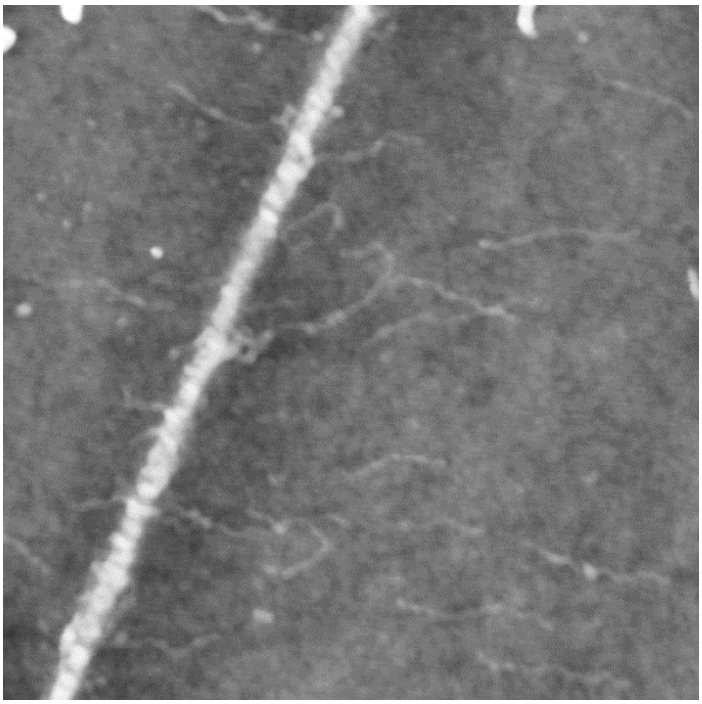

b)

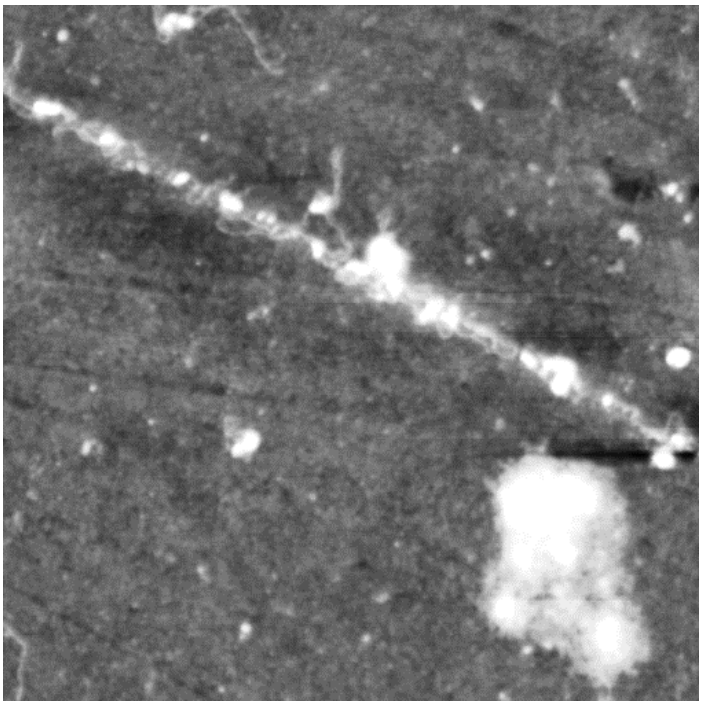

Figure 5.10. AFM scans (1.5 x 1.5 μm, z-scale 18 nm) of BGR surfaces exposed to freshly prepared DNA solutions containing additions of: a) 0.5 mM $NiCl_2$. b) 5.0 mM $NiCl_2$. As the concentration of $NiCl_2$ is increased the conformation of bound DNA molecules appears to become more condensed, and an increase in salt precipitates (bright spots) is observed.

(with AFM) we would encounter large DNA aggregates (Figure 5.11). In general we tended to observe the aggregates less often when imaging fresh solutions, but since surface sampling is so small compared to the size of the BGR substrate surface, we possess insufficient data to properly quantify a trend. The formation of enough DNA aggregates could have reduced the concentration of lone DNA fragments to a level unable to be identified by electrophoresis (or by the AFM). However, if large DNA aggregates existed, we might expect to observe bands lying above the 1000-bp fragment. Failure to observe these bands, would suggest aggregate sedimentation.

Electrophoresis of all aged DNA standards (without salt additions) failed to display the 1000-bp band, so there must be an additional cause then the divalent cation induced sedimentation to explain the null result. Prolonged storage of DNA solutions at room temperature may have caused DNA degradation via residual nuclease activity, leading to insufficient DNA concentrations (of similar sizes) to allow detection via gel electrophoresis.[29] The exact method of degradation is unknown, but may include some degree of chain cleavage (to explain electrophoresis results) as well as influencing the binding behavior of the remaining molecules (to explain AFM results).

Results of both gel electrophoresis and AFM exhibit significant reductions in 1000-bp fragment DNA concentration as a function of DNA solution age (at room temperature) for both samples with and without additions of salt solutions. This reduction is attributed to either (or both) the aggregation / sedimentation of DNA molecules (leading to the decrease in lone molecule concentration), or DNA degradation (influencing the size and reactivity of DNA molecules). These results may explain why we had previously observed superior DNA attachment to BGR surfaces when deposition solutions contained additions of Ni (II) cations (used closer to preparation date than other cation containing solutions) instead of Co (II), Mg (II), Mn (II), or Zn (II).

5.4. Conclusion

DNA solution age is a critical variable that influences the binding of DNA to BGR substrates. A dramatic decrease in bound DNA concentration was observed to accompany increases in DNA solution age. Additionally, aged DNA solutions failed to

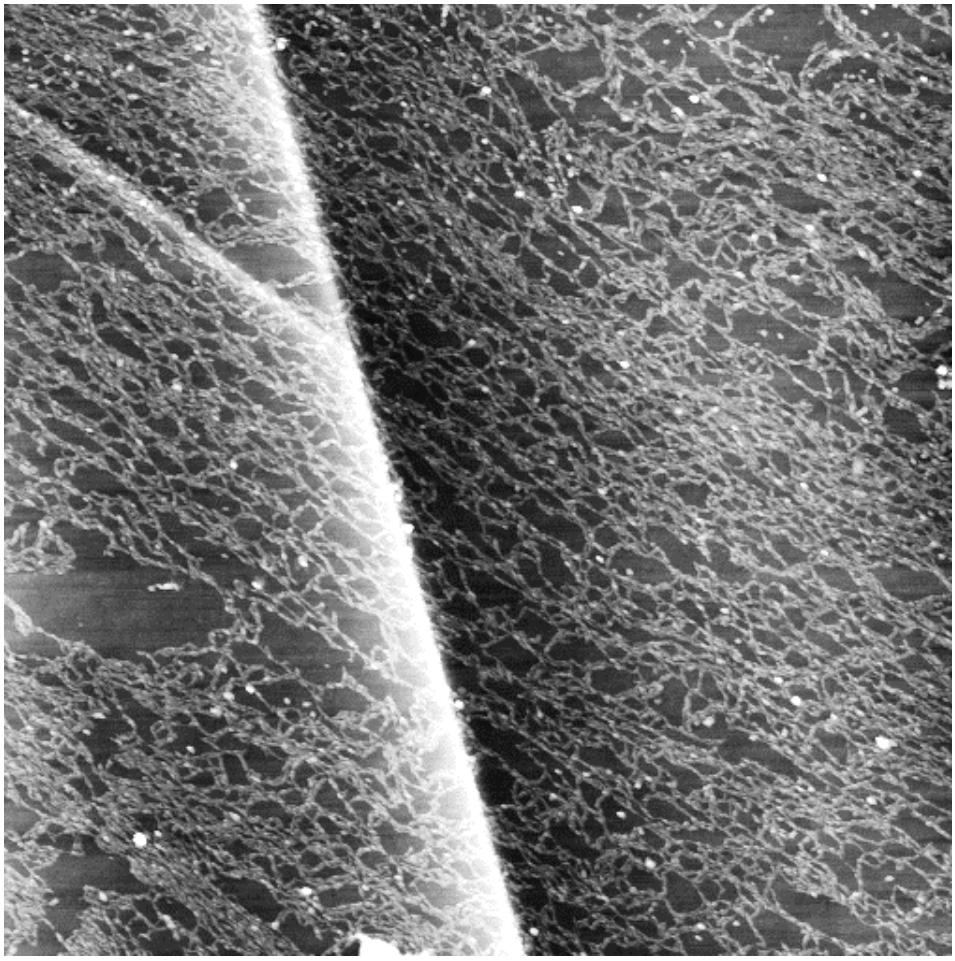

Figure 5.11. AFM scan (5 x 5 μm, z-scale 30 nm, 78 day-old buffer) of a BGR surface exposed to a DNA solution containing the addition of 0.5 mM $CoCl_2$. The image captures a large network of DNA on the sample surface. The presence of networked DNA would result in lower concentrations of lone DNA molecules at other surface locations.

yield distinctive bands during electrophoresis analysis. The exact cause for the null result is unknown, but may be attributed to the formation and sedimentation of DNA attractive metal hydroxides, or possibly an increase in degree of DNA networking, with respect to time. Freshly prepared DNA solutions should be used for deposition experiments, as well as added attention to solution pHs (when using transition metals) to avoid any degradation-induced molecular behaviors.

Classifying the influence of solution age has allowed us to properly elucidate previously unexplained phenomena, as well as provided us a means to effectively isolate additional variables. Understanding the effect each successive variable has on DNA / BGR system could enable tunable (strength and degree) DNA attachment; possibly leading to the development a novel substrate for the assembly of nano- and molecular constructs.

5.5. References

1. R. Bashir, "Invited Review: DNA-mediated Artificial Nanobiostructures: State of the Art and Future Directions," *Superlattices and Microstruct.,* **29** [1] 1-16 (2001).

2. C.M. Niemeyer, "Self-assembled Nanostructures Based on DNA: Towards the Development of Nanobiotechnology," *Cur. Opin. Chem. Biol.,* **4** [6] 609-18 (2000).

3. L.M. Demers, D.S. Ginger, S.J. Park, Z. Li, S.W. Chung, and C.A. Mirkin, "Direct Patterning of Modified Oligonucleotides on Metals and Insulators by Dip-pen Nanolithography," *Science,* **296** [5574] 1836-8 (2002).

4. M. Fujita, W. Mizutani, M. Gad, H. Shigekawa, and H. Tokumoto, "Patterning DNA on Micron Scale on Mica," *Ultramicroscopy,* **91** [1-4] 281-5 (2002).

5. Z. Gueroui, "Immobilization and Stretching of DNA Molecules Above a Lithographed Surface," *Colloids Surf., B,* **33** [1] 53-6 (2004).

6. O. Medalia, J. Englander, R. Guckenberger, and J. Sperling, "AFM Imaging in Solution of Protein-DNA Complexes Formed on DNA Anchored to a Gold Surface," *Ultramicroscopy,* **90** [2-3] 103-12 (2002).

7. P.V. Schwartz, "Meniscus Force Nanografting: Nanoscopic Patterning of DNA," *Langmuir,* **17** [19] 5971-7 (2001).

8. L.A. Bursill, "Intersecting Defect Structures in Gallia- and Magnesia-doped Rutiles," *Acta Cyst.,* **A 35** [3] 449-58 (1979).

9. L.A. Bursill and G.G. Stone, "Tunnel and Intergrowth Structures in the Gallia-rich Gallium Titanate System," *J. Solid State Chem.,* **38** [2] 149-57 (1981).

10. R.M. Gibb and J.S. Anderson, "Electron Microscopy of Solid Solutions and Crystallographic Shear Structures II. Fe_2O_3-TiO_2 and Ga_2O_3-TiO_2 Systems," *J. Solid State Chem.,* **5** [2] 212-25 (1972).

11. A. Kahn, V. Agafonov, D. Michel, and M. Perez Y Jorba, "New Gallium Germanates with Tunnel Structures: alpha-Ga_4GeO_8 and $Ga_4Ge_3O_{12}$," *J. Solid State Chem.,* **65** [3] 377-82 (1986).

12. S. Kamiya and R.J.D. Tilley, "Phase Relations in the Pseudobinary System TiO_2-Ga_2O_3," *J. Solid State Chem.,* **22** [2] 205-16 (1977).

13. D.J. Lloyd, I.E. Grey, and L.A. Bursill, "The Structure of $Ga_4Ti_{21}O_{48}$," *Acta Cryst.,* **B32** [6] 1756-61 (1976).

14. G.G. Stone and L.A. Bursill, "High-resolution Electron Microscopy of (210) Defect Pairs in Gallia-doped Rutile," *Philos. Mag.,* **35** [7] 1397-412 (1977).

15. D.D. Edwards, T.O. Mason, W. Sinkler, L.D. Marks, K.R. Poeppelmeier, Z. Hu, and J.D. Jorgensen, "Tunneled Intergrowth Structures in the Ga_2O_3-In_2O_3-SnO_2 System," *J. Solid State Chem.,* **150** [2] 294-304 (2000).

16. N. Empie and D. Edwards, "Atomic Force Microscopy Study of the Interaction of DNA and Nano-structured Beta-gallia Rutile," *Langmuir,* **22** [18] 7678-63 (2006).

17. O. Pietrement, D. Pastre, F. Stephane, J. Jeusset, M. David, F. Landousy, L. Hamon, A. Zozime, and E. Le Cam, "Reversible Binding of DNA on $NiCl_2$-treated Mica by Varying the Ionic Strength," *Langmuir,* **19** [6] 2536-9 (2003).

18. J. Vesenka, M. Guthold, C.L. Tang, D. Keller, E. Delaine, and C. Bustamante, "Substrate Preparation for Reliable Imaging of DNA Molecules with the Scanning Force Microscope," *Ultramicroscopy,* **42-44** [2] 1243-9 (1992).

19. D. Pastre, O. Pietrement, S. Fusil, F. Landousy, J. Jeusset, M. David, L. Hamon, E. Cam, and A. Zozime, "Adsorption of DNA to Mica Mediated by Divalent Counterions: A Theoretical and Experimental Study," *Biophys. J.,* **85** [4] 2507-18 (2003).

20. H.G. Hansma, I. Revenko, K. Kim, and D.E. Laney, "Atomic Force Microscopy of Long and Short Double-stranded, Single-stranded and Triple-stranded Nucleic Acids," *Nucleic Acids Res.,* **24** [4] 713-20 (1996).

21. A. Sanchez-Sevilla, J. Thimonier, M. Marilley, J. Rocca-Serra, and J. Barbet, "Accuracy of AFM Measurements of the Contour Length of DNA Fragments Adsorbed on Mica in Air and in Aqueous Buffer," *Ultramicroscopy,* **92** [3-4] 151-8 (2002).

22. K. Rippe, N. Mucke, and J. Langowski, "Molecules in Motion: Imaging DNA with the Scanning Force Microscope in Aqueous Solutions," *Bioforum Intl.,* **1** [1] 42-4 (1997).

23. M. Bezanilla, S. Manne, D. Laney, Y. Lyubchenko, and H. Hansma, "Adsorption of DNA to Mica, Silylated Mica and Minerals: Characterization by Atomic Force Microscopy," *Langmuir,* **11** [2] 655-9 (1995).

24. T. Thundat, D.P. Allison, R.J. Warmack, G.M. Brown, K.B. Jacobson, J.J. Schrick, and T.L. Ferrell, "Atomic Force Micrsocopy of DNA on Mica and Chemically Modified Mica," *Scanning Microsc.,* **6** [4] 911-8 (1992).

25. H.G. Hansma and D.E. Laney, "DNA Binding to Mica Correlates with Cationic Radius: Assay by Atomic Force Microscopy," *Biophys. J.,* **70** [4] 1933-9 (1996).

26. N.H. Thomson, S. Kasas, B.L. Smith, H.G. Hansma, and P.K. Hansma, "Reversible Binding of DNA to Mica for AFM Imaging," *Langmuir,* **12** [24] 5905-8 (1996).

27. H. Cheng, K. Zhang, J. Libera, M. Olvera de la Cruz, and M. Bedzyk, "Polynucleotide Adsorption to Negatively Charged Surfaces in Divalent Salt Solutions," *Biophys. J.,* **90** [4] 1164-74 (2006).

28. Y. Li, A. Trinchi, W. Wlodarski, K. Galatsis, and K. Kalantar-Zadeh, "Investigation of the Oxygen Gas Sensing Performance of Ga_2O_3 Thin Films with Different Dopants," *Sens. Actuators,* **B 93** [1-3] 431-4 (2003).

29. E. Kejnovsky and J. Kypr, "Millimolar Concentrations of Zinc and Other Metal Cations Cause Sedimentation of DNA," *Nucleic Acids Res.,* **26** [23] 5295-9 (1998).

30. *CRC Handbook of Chemistry and Physics*, 74th ed. Edited by D. Lide. Chemical Rubber Publishing, Boca Raton, FL, 1994.

6. DNA Attachment to Beta-Gallia Rutile Surfaces as a Function of Divalent Cationic Concentration

Abstract

A suitable planar substrate for the controllable attachment of DNA molecules is desired to aid in advancing nano-electronic, -biologic, and –mechanical technologies. The beta-gallia rutile (BGR) surface has displayed preferential attachment of DNA to $\{210\}_r$ intergrowth boundaries in the presence of certain divalent cations. This study investigates the influence of cation species and concentration on the behavior of DNA attachment to identify how each variable could be altered to aid in optimizing the binding behavior. Four divalent salts ($CoCl_2$, $MgCl_2$, $NiCl_2$, and $ZnCl_2$), at three concentrations (0.5, 1.0, and 5.0 mM), were added to DNA solutions which were exposed to BGR surfaces. Using an atomic force microscope, DNA was observed to preferentially attach to $\{210\}_r$ intergrowth regions of BGR surfaces at all tested cations and cation concentrations. For each cation species, the greatest DNA density was observed at a cation concentration of 1mM; further additions in salt concentration led to decreases in DNA density. From examining end-to-end distances it would appear that the binding strength of DNA molecules had increased with increasing cation concentration. Increased salt precipitation was also observed as sample cation concentration was increased.

6.1. Introduction

A great deal is understood at both the micro- and nano-scales of science; however, the interaction of species between these scales remains a target of numerous studies. DNA is a commonly studied biomolecule due to its controllable structure and complementary base-pairing. Additionally, utilizing highly specific enzymes (endonucleases and ligases) provides the means for the molecular processing of DNA.[1]

A variety of DNA-inspired applications have been conceived, from nanowires and microarrays, to nanomechanical devices. In order to manufacture such applications, a controllable, reliable, and reproducible means to selectively attach and align DNA molecules to substrates is required.

Bare and chemically treated mica surfaces are presently the preferred surface (due to their flatness) to study DNA structure by scanning probe methods. The density of bound DNA on mica surfaces has been shown to be influenced by such variables as cation species, pH, and DNA solution concentration.[2-9] Unfortunately, the specific location of bound DNA molecules can not be controlled by solely adjusting the above variables. In order to provide site-specific attachment on these substrates, additional functionalization steps are required, including the application of patterned aminosilane or gold films.[10-12] Common means to achieve patterned architectures on planar surfaces rely on lithographic or microprobe application processes.[10,11,13-15] Such methods can involve numerous time-consuming steps, the production of needless waste, and can, in some cases, produce patterns on limited size scales.

The limitations observed within the bare-mica system have driven our research to identify and synthesize a substrate providing the possibility of patterned DNA attachment without requiring additional functionalization steps. Previously, we reported the ability of certain divalent cations (Co (II), Mg (II), Mn (II), Ni (II) and Zn (II)) to preferentially attach DNA along $\{210\}_r$ intergrowth regions of beta-gallia rutile (BGR) surfaces.[16] In that study, a ladder DNA solution containing many lengths of DNA molecules was used, preventing adequate conditions to quantify the molecular binding behavior among the various cations.

BGR intergrowths describe a system of phases formed by the insertion of beta-gallia subunits along $\{210\}_r$ planes of (001)-oriented rutile single crystal surfaces. The insertion of beta-gallia along $\{210\}_r$ planes results in the formation of one-dimensional tunnel sites spaced ~ 1nm apart along the $\{210\}_r$ intergrowth boundaries (Figure 6.1). The tunnel sites are ~ 0.25 nm in diameter, adequate for the insertion of small to mid-sized cations.[17] Studies investigating the interaction of DNA and mica surfaces observed that the binding between these two like-charged surfaces is facilitated by the presence of divalent cations.[5,7,8,18] A similar mechanism is believed to exist between DNA and BGR

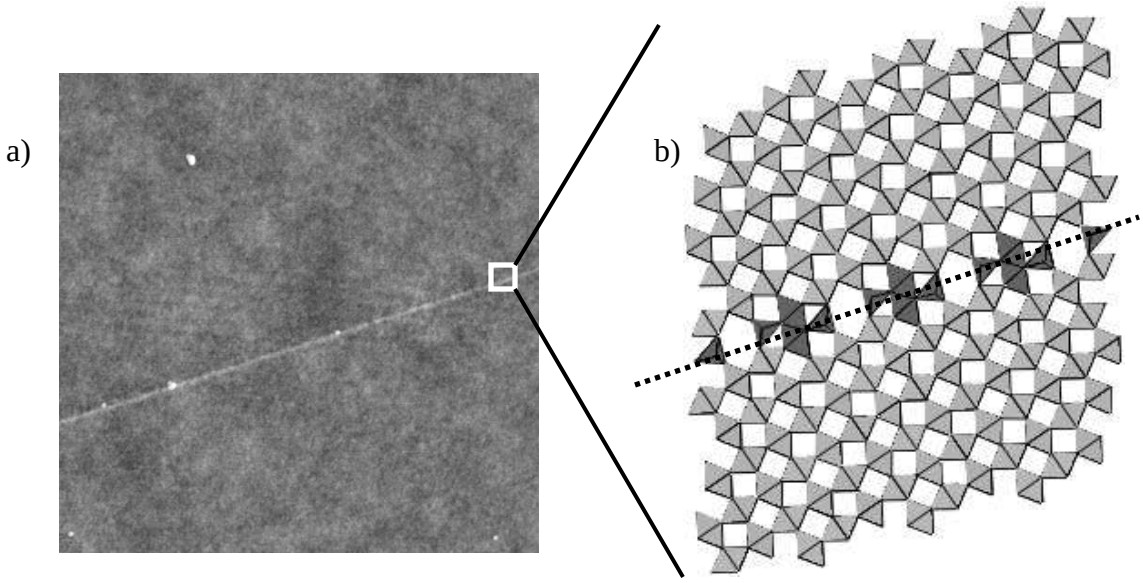

Figure 6.1. a) AFM image (1.5 x 1.5 μm, z-scale : 15 μm) of a bare BGR surface. The bright line running left to right is a $(210)_r$ intergrowth boundary. b) Projection of the BGR structure ($Ga_4Ti_{21}O_{48}$) along [001] of the parent rutile structure, after Ref. [24]. Two-dimensional projections of TiO_6 octahedra are shown in gray. Projections of GaO_6 octahedra and GaO_4 tetrahedra are shown in black. (residing along $\{210\}_r$ shear planes). Dashed line represents a $\{210\}_r$ boundary along which cations (and subsequently DNA) are preferentially bound to hexagonal tunnel sites.

surfaces where the selective attachment of DNA along $\{210\}_r$ intergrowth boundaries is believed to be due to the preference of divalent cations to occupy the $\{210\}_r$ intergrowth tunnel sites.[16,19] BGR phases are characterized by the general equation $Ga_4Ti_{n-4}O_{2n-2}$ (n>9), where the ratio of Ga : Ti governs the distance between gallia-rich $\{210\}_r$ planes.[19-26] A BGR substrate inherently possessing a tailor-able separation of intergrowth lines could be suitable for the self-assembly of nano- and micro-constructs of DNA molecules.

For the present study, we investigate the attachment of monosized DNA to BGR surfaces in the presence of various divalent cation species (Co (II), Mg (II), Ni (II) and Zn (II)) and concentration (0.5, 1.0, 5.0 mM). A solution of monsized (1000bp) DNA fragments was selected to provide comparisons among cation species and cation concentration, to aid in understanding of the role divalent cations play in binding DNA to BGR surfaces. Developing a better understanding of the binding mechanism could enable future studies in buffer solution optimization to achieve controllable binding conditions specific for unique applications.

6.2. Experimental Procedure

6.2.1. Substrate synthesis

To prepare the BGR substrates, a 0.15 M gallium-isopropoxide solution[27] was applied to single crystal, (001)-oriented, TiO_2 substrates (5 x 5 x 0.5 mm) (MTI corp, Richmond, CA) via spin coating for 25 seconds at 2500 rpm (application repeated four times). The coated substrates were dried for 24 hrs prior to heating. Samples were heated at 900^{o}C for 3 hrs, then at 1350^{o}C for 48 hrs. The BGR surfaces were pretreated with a 10 mM chloride solution (containing the appropriate divalent cation) for 1 min.; then rinsed with distilled water. The BGR substrates were then exposed to 2 μl aliquots of salt-containing DNA solution, which were allowed to dry prior to AFM imaging.

6.2.2. DNA preparation

A 100 μg / ml solution of monosized, 1000bp, ds-DNA was obtained from Gensura Laboratories, Inc (San Diego, CA) and diluted to 0.5 μg / ml in 10mM HEPES (4- (2-Hydroxyethyl) piperazine-1-ethanesulfonic acid) buffer, pH 7, and 0.5, 1.0, or 5.0 mM $CoCl_2$, $MgCl_2$, $NiCl_2$, or $ZnCl_2$. A 2 μl aliquot of the DNA / salt solution was applied to each BGR surface within 8 hours of buffer synthesis to avoid the effects of DNA solution aging.

6.2.3. AFM imaging

The samples were characterized, in air, using a Nanoscope III AFM (Digital Instruments, Santa Barbara, CA) in tapping mode. The microscope was equipped with silicon probes (Ted Pella, Inc., Redding, CA) operating at frequencies between 200 and 500 kHz. The cantilevers were 125 μm long with a force constant of 40 N / m. Sample surfaces were mapped with Cartesian coordinates to provide successive scanning of equivalent spatial locations following various surface treatments.

6.2.4. Degree of binding preference

A procedure to determine preferential attachment was developed which involves comparing the density of DNA per $\{210\}_r$ intergrowth boundary to that of an equivalent length of random grid line. The length and number of DNA molecules in contact with $\{210\}_r$ intergrowth lines was recorded. A 113 x 113 line grid was overlaid onto the images, the number of DNA molecules in contact with an equal length (to the length of the $\{210\}_r$ intergrowth line) of grid line(s) was also recorded. Molecules intersected by more than one grid line, or more than one $\{210\}_r$ line were only counted once. A random number generator was used to determine which grid lines would be selected. For each image, the grid method was applied ten times to yield an average value for the number of intersected DNA molecules. To aid comparisons between cation concentration and cation species, the number of intersected DNA molecules was normalized by the

appropriate length, and designated as the linear DNA density (molecules / μm). At each cation / concentration level, between 20-40 AFM scans (typically 1 x 1 μm to 2 x 2 μm) were used to calculate the average linear DNA densities. A value designated as the degree of preference describes the linear DNA density of {210} intergrowth lines divided by the linear DNA density of grid lines. If a system were to show no preference, we would expect this value to equal one.

DNA preferential attachment behavior along $\{210\}_r$ boundaries prevents the adequate comparison of total DNA surface density among different scans, since these scans possess different total lengths of $\{210\}_r$ intergrowth lines (images possessing a greater percentage area occupied by $\{210\}_r$ boundaries would have greater DNA densities). In light of this effect, we report the linear DNA density per μm $\{210\}_r$ boundary, and per μm randomly oriented, equivalent length, grid line.

6.3. Results and Discussion

Our group has recently investigated the influence of divalent cation additions to 100 bp ladder DNA solutions exposed to BGR surfaces. The preferential attachment of DNA molecules along the $\{210\}_r$ intergrowth boundaries occurred when buffer solutions containing Co (II), Mg (II), Mn (II), Ni (II), and Zn (II) were used.[16] Here we investigate the influence of cation concentration / species on DNA attachment. For easier quantitation, a monosized DNA segment was chosen.

DNA attached to BGR surfaces at all cation species (Co (II), Mg (II), Ni (II), and Zn (II)) and concentration levels (0.5, 1.0, 5.0 mM) studied. Images collected were analyzed via the grid method, which revealed that all the samples had exhibited preferential attachment; i.e. the average DNA density along the $(210\}_r$ boundary line was greater than the average DNA density on equivalent length random grid lines (Figure 6.2).

For each cation species tested, the samples possessing 1 mM MCl_2 (M = divalent metal cation) appeared to promote the greatest amount of DNA attachment (Figure 6.2).

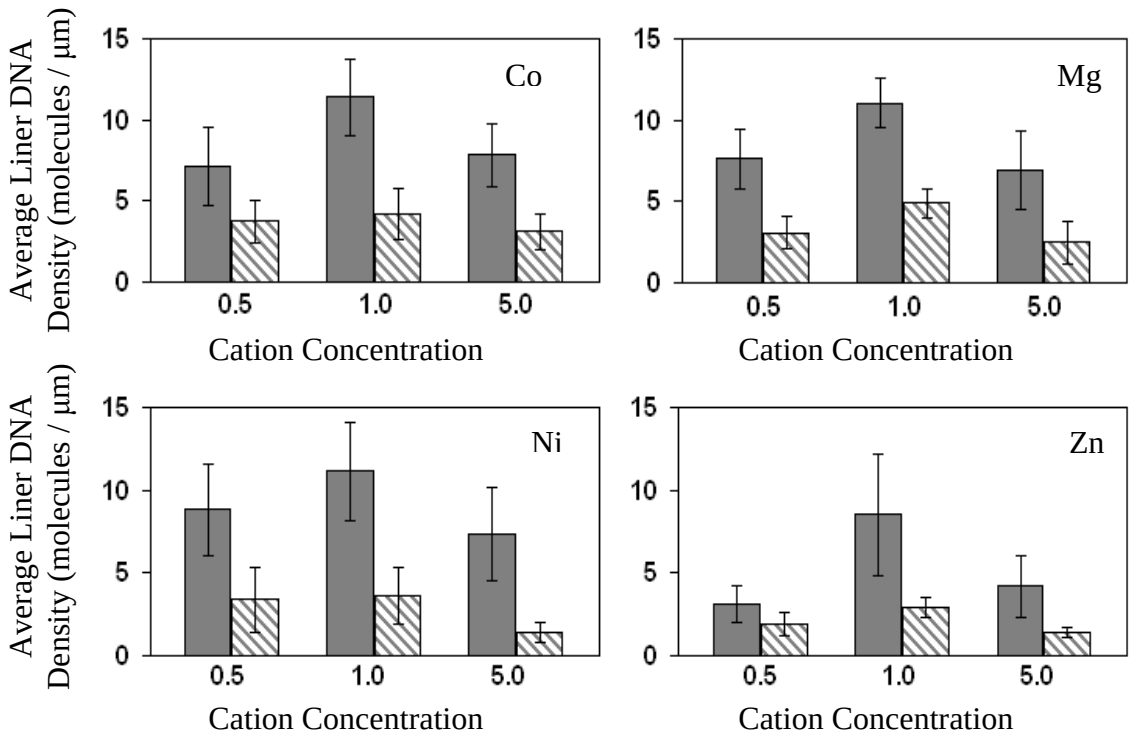

Figure 6.2. Average linear DNA densities as a function of cation species and cation concentration. The solid bars represent average densities of DNA on $\{210\}_r$ intergrowth lines, while the dashed lines are average densities on equivalent length, random grid lines. For all cation species and cation concentrations, densities of DNA on $\{210\}_r$ intergrowth lines are significantly higher than those found on grid lines, suggesting preferential binding of DNA to $\{210\}_r$ intergrowth regions of BGR surfaces.

In a study by Hansma and Laney, a similar relationship was described within the DNA / mica system in the presence of Ni (II), Co (II), and Zn (II).[5] Initial increases in DNA attachment from 0.5 to 1.0mM MCl_2 support the hypothesis that divalent cations are facilitating the binding between two negatively charged surfaces. The reduction in DNA density from 1.0 to 5.0 mM, may contradict this behavior; but similar reductions in DNA density at elevated cation concentration have been observed in experimental studies between DNA and mica and DNA and silica surfaces conducted elsewhere.[5,9,18] Mechanisms for reduced DNA surface densities at high salt concentrations have been proposed previously, including mass action, precipitated salt effects, and induced molecular aggregation.

A mass action argument to explain the decrease in DNA concentration would suggest that as the salt concentration increases, both the DNA and BGR surface will become saturated with divalent cations.[5] Additional ions in excess of saturation may be unable to react with surface species, instead, impeding intimate contact required to bind the two surfaces.

Thompson *et al.* observed similar increases in deposition of DNA at initial increases in Zn (II) concentration; but further increases in salt concentration lead to the deposition of salt layers on the mica surface, eventually forming a thick coating that masks the bound DNA.[9] Unlike their study, our current research was conducted in air (not in fluid). In our work we have observed regions which appear caked with dried buffer (Figure 6.3a). A schematic diagram of a drying DNA solution droplet is shown in Figure 6.4. The dried regions are believed to be DNA dense, since they most likely contain any molecules that had not bound due to the force of the receding meniscus. The occurrence of coated regions increased in samples containing 5 mM salt solution. All of the DNA that has not attached to the surface could be pooled in these locations. If a lion-share of the DNA has been pooled in areas that could not be imaged, lower concentrations may then remain for regions that were able to be scanned.

Certain metal cations have been shown to form water insoluble hydroxides at alkaline pH, or at sufficiently high cation concentrations at neutral pH.[9,28] Kejnovosky and Kypr observed sedimentation of DNA in solutions exposed to mM concentrations of transition metal chlorides of Zn (II), Mn (II), Co (II), Ni (II) (solutions were incubated for

a)

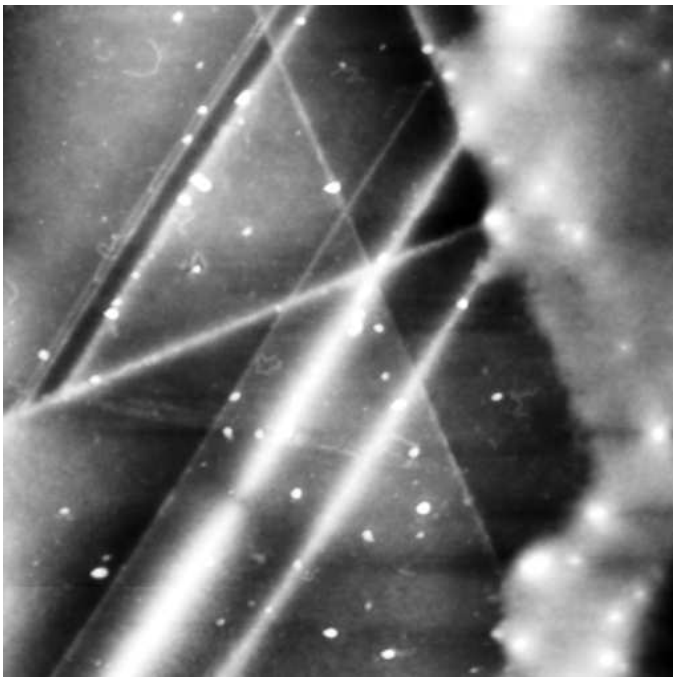

b)

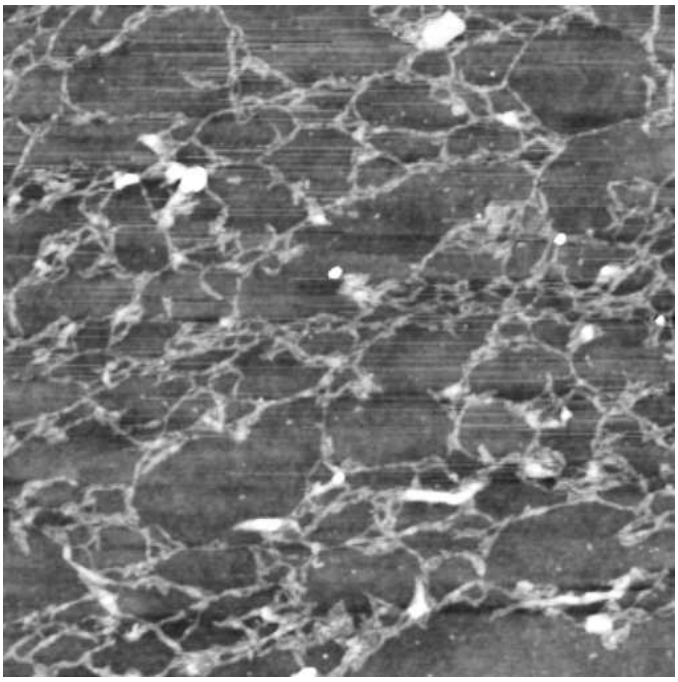

Figure 6.3. AFM images (3 x 3 μm, z scale: 30nm) of: a) A BGR surface exposed to a DNA solution containing 1 mM $ZnCl_2$. The large lighter-colored globular structure along the right side of the image is a portion of the BGR surface covered by a layer of dried salt. b) A network of intertwined, aggregates of DNA bound to a BGR surface exposed to a DNA solution containing 5 mM $ZnCl_2$.

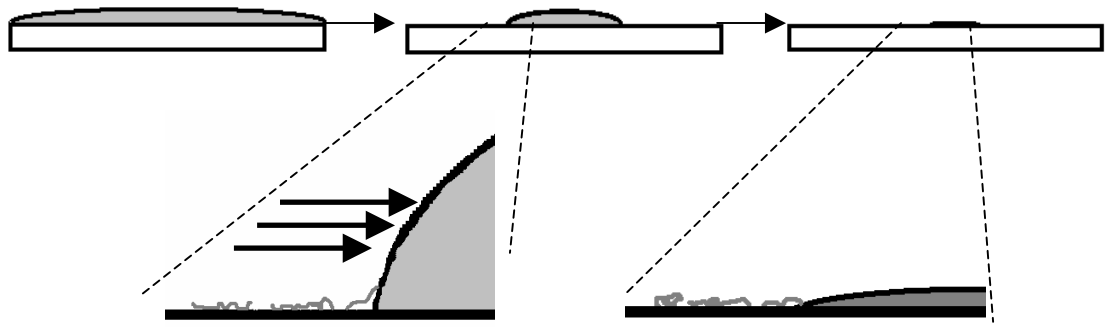

Figure 6.4. A schematic of a DNA solution droplet (gray) drying on a BGR surface. As the droplet dries, the receding meniscus pulls with it any unbound DNA molecules. The last frame shows the remnants of the receding meniscus; which is typically too thick / rough to image underlying features. This dried region could possess higher concentrations of DNA than the surrounding areas. The surface area of dried buffer regions tended to increase with additions in buffer salt concentration.

20 min. prior to centrifugation). The amount of DNA in the sediment of their experiment was shown to increase with cation concentration and pH [28]. For our samples, increases in the precipitation and sedimentation of DNA-attracting salts could impart lower concentrations of lone DNA molecules left in solution. While micro-pipetting from DNA solutions, the DNA-rich sediments may not have been removed from the containers, or may contribute to the un-observable regions.

While scanning some regions of our surfaces, highly dense aggregates of DNA molecules were observed (Figure 6.3b). In general, these aggregates appeared more common in samples prepared at higher salt concentrations; but since our substrate surface is on the order of ten-million times larger than the scan size, the sampling we are taking is not sufficient to properly verify a trend. A study conducted by Dahlgreen and Lyubchenko, however, found an increase in DNA dimer and trimer formation as a function of cation concentration.[29] So there could in fact be an increase in the prevalence of aggregated DNA in samples prepared with 5 mM DNA. Finding the location of heavily aggregated DNA could prove difficult; it is more probable to instead observe regions containing predominately less-dense, isolated DNA molecules. The removal of molecules from the overall solution (via aggregation) would reduce the number of lone DNA molecules elsewhere, contributing to lower DNA concentration counts.

The average preference for DNA to bind to $\{210\}_r$ regions (average DNA density along $\{210\}_r$ boundaries divided by the average density along equivalent length grid line) is displayed in Figure 6.5. All values are greater than unity, suggesting a preference of DNA molecules for $\{210\}_r$ intergrowth boundaries. The average values suggest a general increase in degree of preferential attachment as salt concentration increases, but the variability within the data inhibits proper identification of a trend.

Although considerable variability exists within the data in Figure 6.6, it roughly appears that at each cation concentration, the solutions containing Zn (II) bound the least DNA along $\{210\}_r$ regions. Data collected by Hansma and Laney also observed that DNA solutions containing Zn (II) cations bound less DNA to mica surfaces than solutions containing Co (II) or Ni (II).[5] Cationic size had previously been considered an important variable in the attachment of DNA to BGR and mica surfaces, with attachment believed to depend on the cations' ability to reside in tunnel sites or recessed cavities

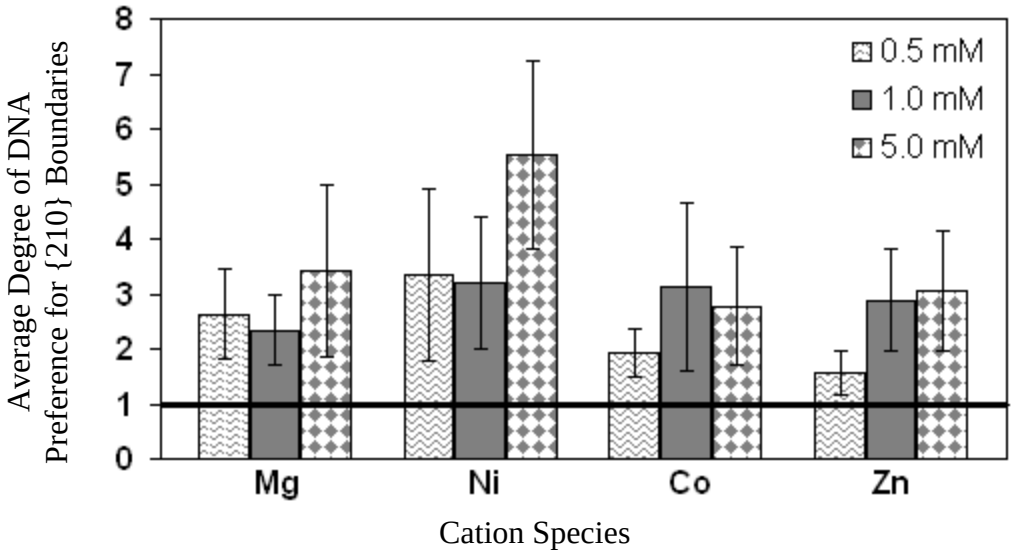

Figure 6.5. Average degree of DNA preference for $\{210\}_r$ intergrowth boundaries on BGR surfaces as a function of cation species and concentration. Black horizontal line drawn at a degree of 1 represents a situation where no site specific binding preference would exist. All averages and deviations are above the black line so there exists a significant preference for DNA to attach to $\{210\}_r$ intergrowth boundaries of BGR surfaces. The averages suggest a slight increase in degree of $\{210\}_r$ preference as a function of increasing salt concentration.

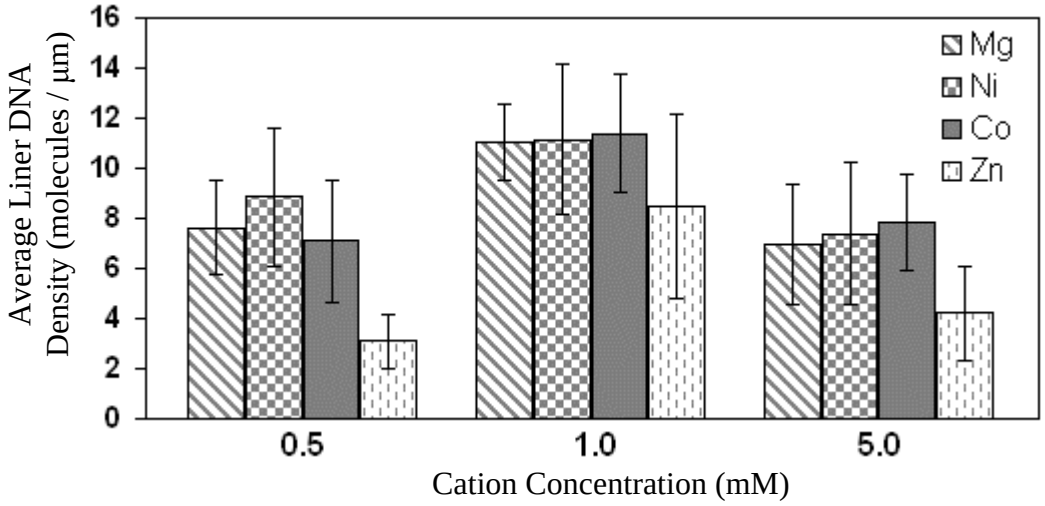

Figure 6.6. Average linear DNA density along $\{210\}_r$ boundaries as a function of cation concentration and cation species. Average DNA densities collected in presence of Zn (II) cations appear to be less compared to the other cations species at all tested cation concentrations.

along the respective surfaces.[5,16] Zinc (II) and Co (II) cations possess similar ionic radii (0.740 and 0.745 Å respectively [30]), but the degree of DNA attachment does not appear to be equal. A cation's enthalpy of hydration was also believed to influence its ability to bind DNA.[5] Zn (II) and Co (II) possess very similar enthalpies of hydration as well (-2044 and -2054 kJ/mol [31]). These results would suggest that additional factors beyond ionic radii and enthalpy of hydration are influencing the degree of attachment.

A possible explanation for the lower degree of binding in the DNA buffers with Zn (II) additions may be related to zinc precipitation. Thompson *et al.* reported solutions prepared at high salt concentration (>2.5 mM) produced the precipitation of zinc hydroxide on mica substrates.[9] Kejnovosky and Kypr observed >90% of the DNA existing in the sediment for zinc and manganese chlorides at a concentration of 10mM and a pH > 8.[28] The results of their study determined that the rate of DNA sedimentation correlated with a cations' ability to form an insoluable hydroxide; which both decreased along the following sequence: Zn, Co, Ni, Mn, Mg, Ca.[28,32] So solutions containing additions of Zn (II) would be expected to possess the greatest degree of hydroxide formation and DNA sedimentation. Images obtained from solutions containing Zn (II) additions confirmed these results, typically possessing greater amounts of salt precipitates (bright spots) which also increased as the concentration of Zn (II) is increased (Figure 6.7). Enhanced DNA sedimentation prior to sampling could have lead to lower concentrations of bound DNA. Additionally, the formation of the hydroxide would cause a decrease in the solution pH, which has also been shown to have a significant effect on the adsorption of DNA to mica surfaces.[9,18,33]

A second possible explanation may be due to a greater predilection for molecule aggregation within solutions containing Zn (II). Dahlgren and Lubchenko had observed dramatic reductions in number of isolated DNA molecules in the presence of $ZnCl_2$ (especially at salt concentration greater than 3 mM) as compared to $MgCl_2$ or $MnCl_2$.[29] DNA molecules imaged from $ZnCl_2$ containing samples in our study are more frequently observed bound (in very condensed conformations) to salt precipitates than in other cation-containing solutions. Zn (II) cations have been observed to promote kinks within DNA chains; these salt induced kinks could lead to highly condensed conformations leading to a reduced surface area and a corresponding reduction in the number of reactive

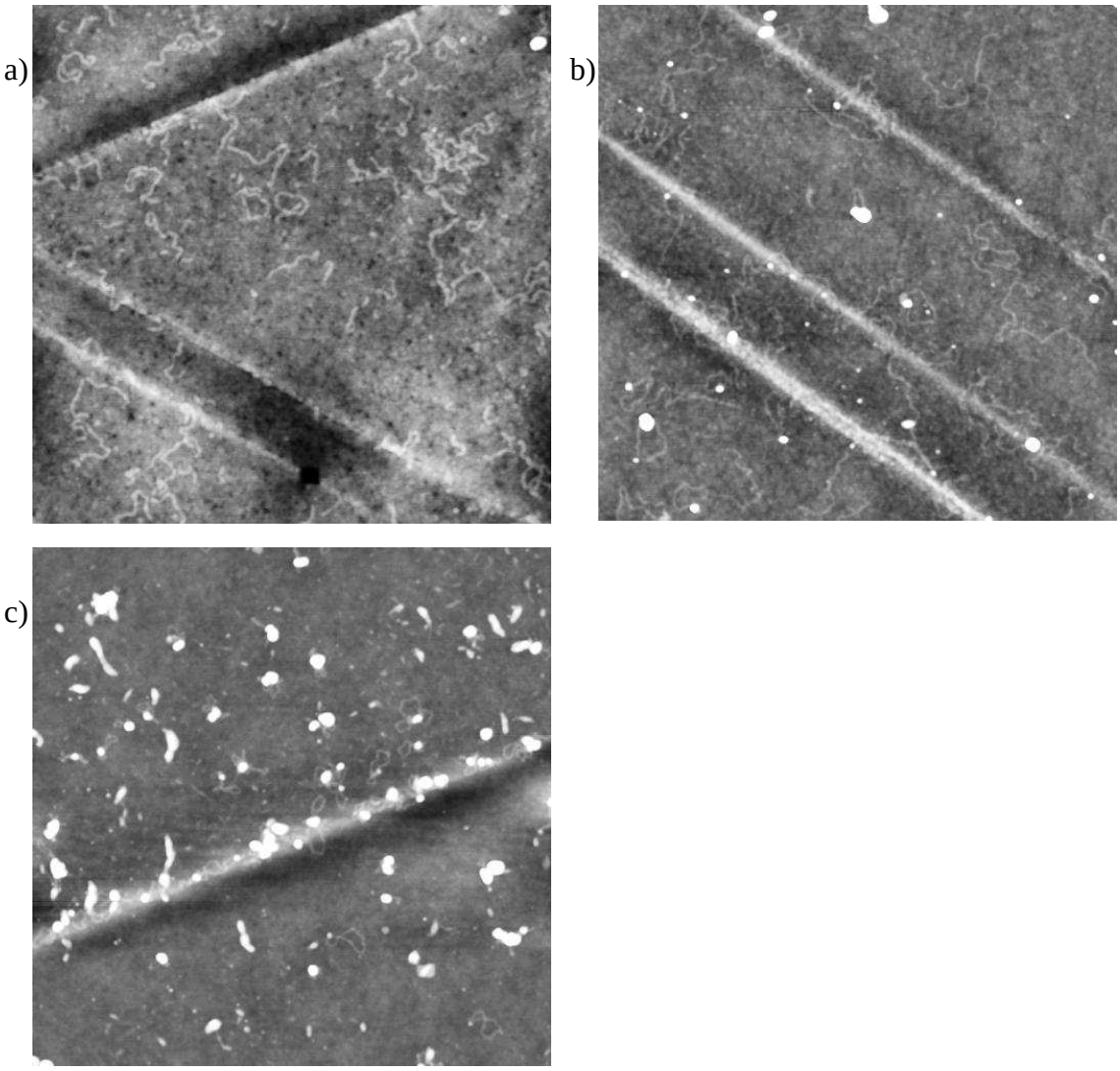

Figure 6.7. AFM images (1.5 x 1.5 μm, z-range: 15 nm) of BGR surfaces exposed to DNA solutions containing additions of: a) 0.5 mM $ZnCl_2$ b) 1.0 mM $ZnCl_2$ c) 5.0 mM $ZnCl_2$. As the concentration of $ZnCl_2$ is increased the conformation of bound DNA molecules appears to become more condensed, and an increase in salt precipitates is observed.

surface sites capable of binding to the BGR surface.[34] These condensed conformations may also have generated improper DNA counts. Additionally, as described above, there may also exist regions containing extremely dense, aggregated DNA networks, reducing the DNA concentration for the remaining surface regions.

6.3.1. Strength of attachment

The end-to-end distance of bound DNA has been described as a suitable parameter to estimate the molecules' binding strength.[7] DNA molecules strongly bound to a surface will resemble rigid projections of their 3-D confirmations upon adsorbing to the surface, whereas loosely bound molecules will be able to equilibrate to a 2-D conformation.[7,35] Surface irregularities and DNA overlapping / aggregation observed at 1 and 5mM salt concentrations hindered effective calculation of end-to-end distances; but, in general, molecules bound to BGR surfaces appeared to become more condensed with increased cation concentration, suggesting that additions in divalent salt promote stronger binding of DNA (Figure 6.7-6.10).

Images collected from solutions containing $ZnCl_2$, possessed the largest amount of dried salt as compared to the other cation solutions (Figure 6.7a-c). DNA molecule conformations were highly condensed when in contact with salt precipitates (Figure 6.7c). Molecules bound along $\{210\}_r$ intergrowth boundaries in the presence of 1 and 5 mM and $ZnCl_2$ possess much smaller end-to-end distances (in most cases, the molecules were too entangled to measure effective distances) than those bound to rutile-rich surface regions (Figure 6.7b,c) .

The DNA molecules bound in the presence of 0.5 mM $NiCl_2$ appeared to be aligned in a given direction (believed to be the direction of the receding meniscus [36,37]). At this salt concentration the majority of DNA molecules appear to attach at their endpoints, with the remainder of the molecule being pulled in the direction of the receding meniscus (Figure 6.8a). As the salt concentration of the solution was increased to 1mM, the molecules bound to the BGR surface appeared to become more collapsed and condensed, suggesting a stronger binding to the surface (Figure 6.8b). At 5 mM, an increase in dried salt (globular shaped) is observed lying predominately along $\{210\}_r$

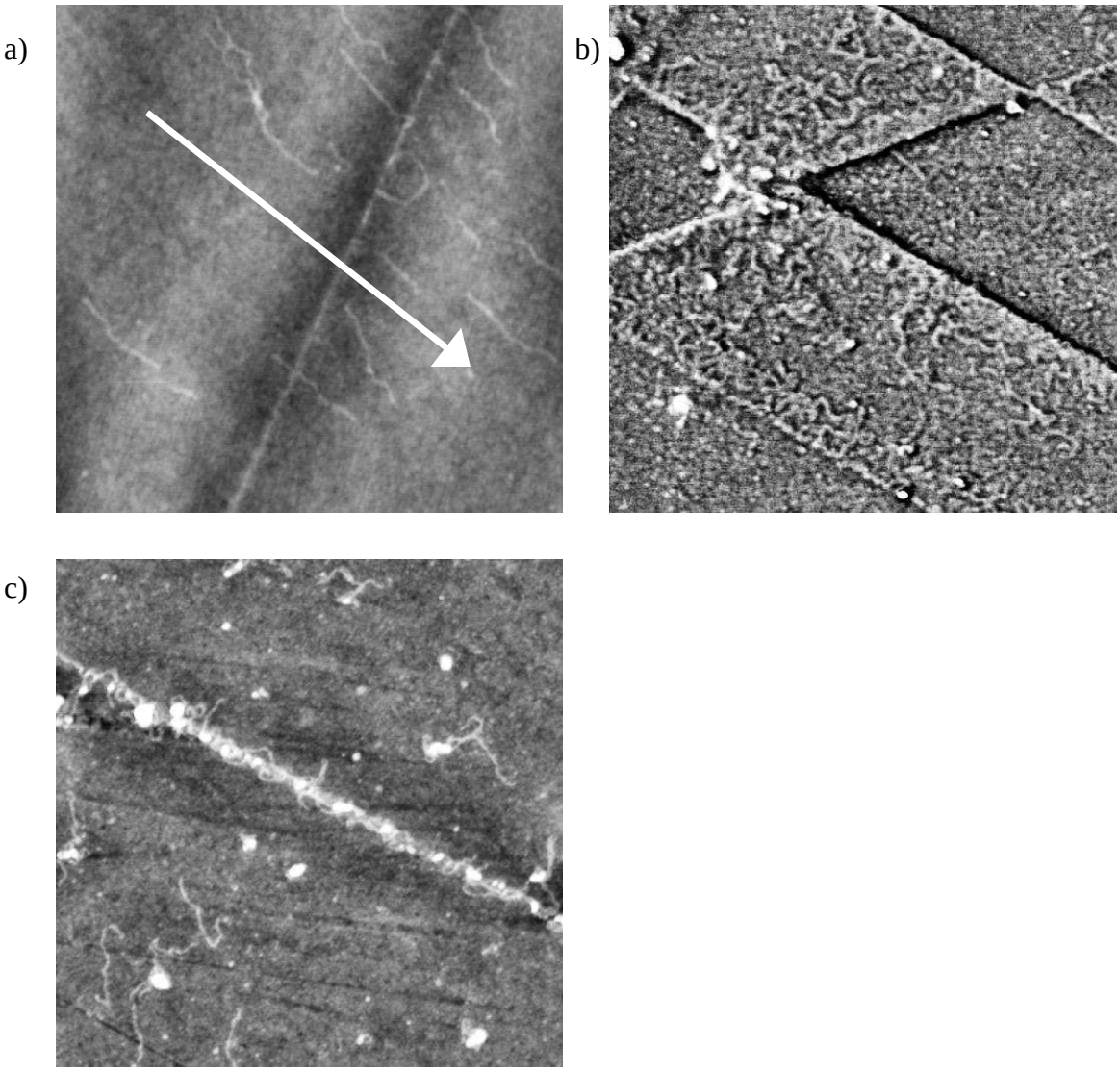

Figure 6.8. AFM images (1.5 x 1.5 μm) of BGR surfaces exposed to DNA solutions containing additions of: a) 0.5 mM $NiCl_2$ (z-scale: 15nm). The white arrow describes the assumed direction of the receding meniscus. The associated force of the meniscus is believed to explain the aligned orientation of bound molecules. b) 1.0 mM $NiCl_2$ (phase image, z-scale: 20^o) c) 5.0 mM $NiCl_2$ (z-scale: 15nm). As the concentration of $NiCl_2$ is increased the conformation of bound DNA molecules appears to become more condensed, and an increase in salt precipitates is observed.

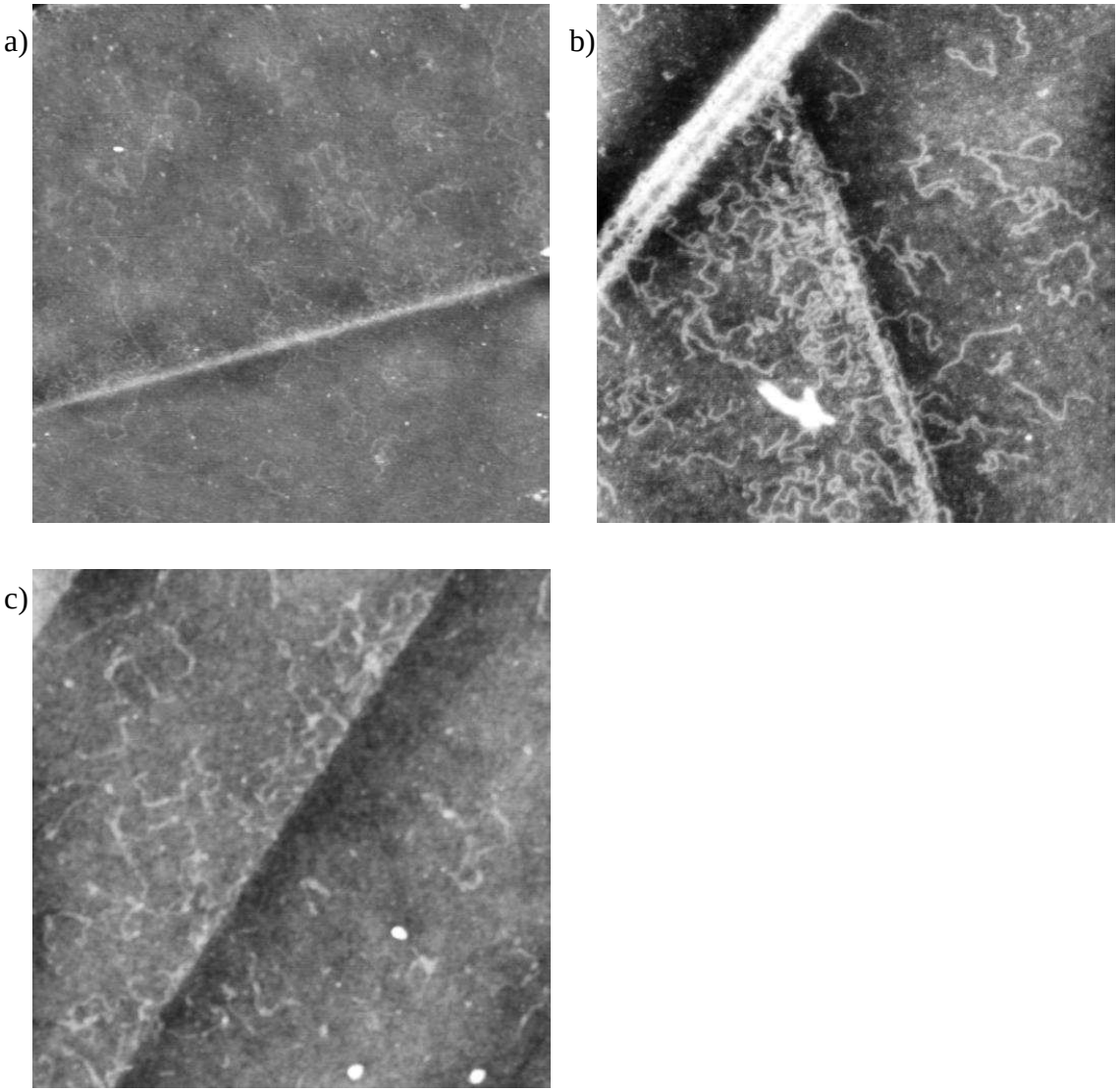

Figure 6.9. AFM images (1.5 x 1.5 μm, z-scale: 15nm) of BGR surfaces exposed to DNA solutions containing additions of: a) 0.5 mM $CoCl_2$. b) 1.0 mM $CoCl_2$. c) 5.0 mM $CoCl_2$. As the concentration of $CoCl_2$ is increased the conformation of bound DNA molecules appears to become more condensed.

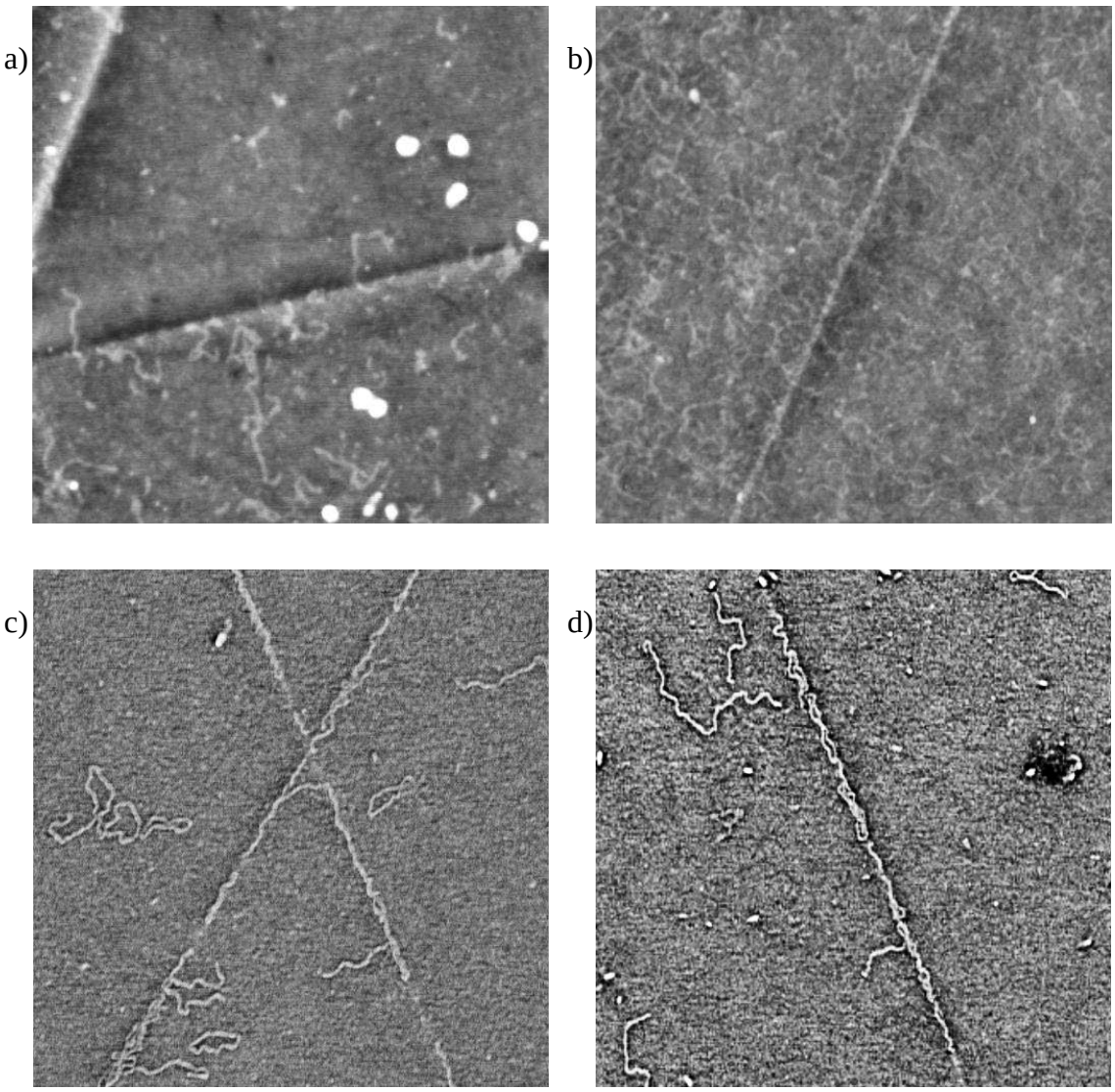

Figure 6.10. AFM images (1.5 x 1.5 μm) of BGR surfaces exposed to DNA solutions containing additions of: a) 0.5 mM $MgCl_2$ (z-scale: 15nm). b) 1.0mM $MgCl_2$ (z-scale: 15nm). c) 5.0 mM $MgCl_2$ (phase image, z-scale: 20^o). d) 5.0 mM $MgCl_2$ (phase image, z-scale: 20^o). Images c and d in the presence of 5 mM $MgCl_2$ exhibit a high degree of preferential attachment of DNA along $\{210\}_r$ intergrowth boundaries.

intergrowth boundaries (Figure 6.8c). Observing a greater degree of salt deposition along $\{210\}_r$ intergrowth boundaries supports the belief that the divalent cations are preferentially attaching to tunnel sites within these linear boundaries, subsequently facilitating the attachment of DNA.

Solutions containing Co (II) additions appeared to follow similar trends observed within the other cation-containing solutions (Figure 6.9a-c). Molecules bound to $\{210\}_r$ boundaries appeared to become more condensed with increases in cation concentration (Figure 6.9a-c). At a concentration of 0.5 mM $CoCl_2$ (Figure 6.9a) the DNA molecules did not appear to be as extended as they were while in the presence of 0.5mM $NiCl_2$ (Figure 6.8a), suggesting that at this level of salt concentration, Co (II) cations bind DNA molecules more tightly than Ni (II) cations. At the 5.0 mM concentration, there did not appear to be as many salt deposits as those observed in the presence of $NiCl_2$ or $ZnCl_2$, so highly condensed DNA conformations were not as prevalent.

Solutions containing 0.5 and 1.0 mM $MgCl_2$ behaved similarly to other cation-containing solutions (Figure 6.10a,b); a decrease in end-to-end distance was observed while increasing $MgCl_2$ concentration. The binding of DNA molecules along {210} boundaries in the presence of 5.0 mM $MgCl_2$ differed from the adsorption behavior observed with the other divalent cations tested. At 5.0 mM $MgCl_2$, both highly condensed, and outstretched molecules were observed (Figure 6.10c). The outstretched behavior observed within the Mg (II) samples is not believed to be due to a receding meniscus force (as observed at 0.5 mM $NiCl_2$ solutions) since the orientation of bound molecules is not uniform in one direction (compare Figure 6.10a to Figure 6.8a), but rather aligned along $\{210\}_r$ intergrowth boundaries. This difference in binding behavior could be based in the interaction between the divalent cation and the DNA molecule. According to Izatt *et al*., the Mg (II) cation binds primarily to the phosphate groups along the DNA backbone; whereas the affinity for nucleotide base-binding in relation to phosphate binding increases in the following order: Mg (II), Co (II), Ni (II), Mn (II), Zn (II), Cd (II), and Cu (II).[38,39] In DNA solutions containing Co (II), Ni (II), and Zn (II) additions, a higher degree of base binding could lead to higher affinities for molecular aggregation from base – base hybridization;[29] whereas the Mg (II) cations' higher affinity for phosphate binding sites could lead to a reduction in molecular aggregation.

6.4. Conclusion

Monosized 1000-bp solutions of DNA molecules containing additions of divalent salts ($CoCl_2$, $MgCl_2$, $NiCl_2$, and $ZnCl_2$ at 0.5, 1.0, and 5.0 mM concentrations) were observed to attach DNA preferentially to $\{210\}_r$ intergrowth regions of BGR surfaces. The results of this study have further supported the hypothesis that tunnel sites along $\{210\}_r$ intergrowth boundaries serve as preferential positions for divalent cation occupation. The degree of binding preference was determined by comparing the number of DNA molecules bound to $\{210\}_r$ boundaries to the number intersected by an equivalent length of randomly oriented grid lines. Increasing the salt concentration of the DNA solutions from 0.5 to 1.0 mM led to increases in attached DNA density; while further salt addition to a level of 5.0 mM led to decreased DNA attachment. Although no clear reason for this behavior could be identified, the results of our study support mechanisms including the mass action, precipitated salt, and induced molecular aggregation to explain this decrease. Of the four cations tested, solutions contains Zn (II) appeared to bind the lowest amount of DNA. The lower DNA surface densities were attributed to factors including zinc-hydroxide / -salt precipitation, as well as the cations heightened predilection for DNA molecule aggregation.

The binding strength of attached DNA molecules appeared to increase as a function of cation concentration, as reflected in their end-to-end distances. Comparing data collected from DNA solutions containing differing salt concentrations and divalent cation species, has proved that altering these variables could allow for the optimization of binding conditions to suit unique applications. For instance, if DNA–protein interaction is the focus of a study, the DNA molecule should be accessible to the protein; a loosely bound conformation would then be more desirable. To achieve such a conformation lower salt concentrations should be selected. Although the roughness of currently synthesized BGR surfaces may inhibit the identification of more intimate features of DNA structure, the substrate does succeed in providing a surface for the site-specific attachment of DNA without additional / cumbersome functionalization steps required with alternate substrates.

6.5. References

1. C.M. Niemeyer, "Self-assembled Nanostructures Based on DNA: Towards the Development of Nanobiotechnology," *Cur. Opin. Chem. Biol.*, **4** [6] 609-18 (2000).

2. Y. Fang, T.S. Spisz, and J.H. Hoh, "Ethanol-induced Structural Transitions of DNA on Mica," *Nucleic Acids Res.*, **27** [8] 1943-9 (1999).

3. M. Guthold, M. Bezanilla, D. Erie, B. Jenkins, H. Hansma, and C. Bustamante, "Following the Assembly of RNA Polymerase-DNA Complexes in Aqueous Solutions with the Scanning Force Microscope," *Proc. Natl. Acad. Sci. U.S.A.*, **91** [26] 12927-31 (1994).

4. H. Hansma, M. Benzanilla, F. Zanhausern, M. Adrian, and R. Sinsheimer, "Atomic Force Microscopy of DNA in Aqueous Solutions," *Nucleic Acids Res.*, **21** [3] 505-12 (1993).

5. H.G. Hansma and D.E. Laney, "DNA Binding to Mica Correlates with Cationic Radius: Assay by Atomic Force Microscopy," *Biophys. J.*, **70** [4] 1933-9 (1996).

6. Y.L. Lyubchenko, B.L. Jacobs, S.M. Lindsay, and A. Stasiak, "Atomic Force Microscopy of Nucleoprotein Complexes," *Scanning Microsc.*, **9** [3] 705-27 (1995).

7. D. Pastre, O. Pietrement, S. Fusil, F. Landousy, J. Jeusset, M. David, L. Hamon, E. Cam, and A. Zozime, "Adsorption of DNA to Mica Mediated by Divalent Counterions: A Theoretical and Experimental Study," *Biophys. J.*, **85** [4] 2507-18 (2003).

8. O. Pietrement, D. Pastre, F. Stephane, J. Jeusset, M. David, F. Landousy, L. Hamon, A. Zozime, and E. Le Cam, "Reversible Binding of DNA on $NiCl_2$-treated Mica by Varying the Ionic Strength," *Langmuir*, **19** [6] 2536-9 (2003).

9. N.H. Thomson, S. Kasas, B.L. Smith, H.G. Hansma, and P.K. Hansma, "Reversible Binding of DNA to Mica for AFM Imaging," *Langmuir*, **12** [24] 5905-8 (1996).

10. M. Fujita, W. Mizutani, M. Gad, H. Shigekawa, and H. Tokumoto, "Patterning DNA on Micron Scale on Mica," *Ultramicroscopy*, **91** [1-4] 281-5 (2002).

11. O. Medalia, J. Englander, R. Guckenberger, and J. Sperling, "AFM Imaging in Solution of Protein-DNA Complexes Formed on DNA Anchored to a Gold Surface," *Ultramicroscopy*, **90** [2-3] 103-12 (2002).

12. Y. Yourdshahyan, H.K. Zhang, and A.M. Rappe, "N-alkyl Thiol Head-group Interactions with the Au (111) Surface," *Phys. Rev. B: Condens. Matter,* **63** [8] 081405 4pp (2001).

13. L.M. Demers, D.S. Ginger, S.J. Park, Z. Li, S.W. Chung, and C.A. Mirkin, "Direct Patterning of Modified Oligonucleotides on Metals and Insulators by Dip-pen Nanolithography," *Science,* **296** [5574] 1836 (2002).

14. Z. Gueroui, "Immobilization and Stretching of DNA Molecules Above a Lithographed Surface," *Colloids Surf., B,* **33** [1] 53-6 (2004).

15. P.V. Schwartz, "Meniscus Force Nanografting: Nanoscopic Patterning of DNA," *Langmuir,* **17** [19] 5971-7 (2001).

16. N. Empie and D. Edwards, "Atomic Force Microscopy Study of the Interaction of DNA and Nano-structured Beta-gallia Rutile," *Langmuir,* **22** [18] 7678-63 (2006).

17. G.V. Chandrashekar, A. Bednowitz, and S.J. La Placa, "A One Dimensional Sodium Ion Conductor," pp. 447-50 in *Fast Ion Transport in Solids.* Edited by P. Vashishta, J. N. Mundy, and G. K. Shenoy. Elsevier, New York, 1979.

18. H. Cheng, K. Zhang, J. Libera, M. Olvera de la Cruz, and M. Bedzyk, "Polynucleotide Adsorption to Negatively Charged Surfaces in Divalent Salt Solutions," *Biophys. J.,* **90** [4] 1164-74 (2006).

19. N. Empie and D. Edwards, "Phase Stability and Structure of Alkali Doped-beta-gallia Rutile Intergrowths," *Solid State Ionics,* **177** [1-2] 77-87 (2006).

20. L.A. Bursill, "Intersecting Defect Structures in Gallia- and Magnesia-doped Rutiles," *Acta Cyst.,* **A 35** [3] 449-58 (1979).

21. L.A. Bursill and G.G. Stone, "Tunnel and Intergrowth Structures in the Gallia-rich Gallium Titanate System," *J. Solid State Chem.,* **38** [2] 149-57 (1981).

22. D.D. Edwards, T.O. Mason, W. Sinkler, L.D. Marks, K.R. Poeppelmeier, Z. Hu, and J.D. Jorgensen, "Tunneled Intergrowth Structures in the Ga_2O_3-In_2O_3-SnO_2 System," *J. Solid State Chem.,* **150** [2] 294-304 (2000).

23. R.M. Gibb and J.S. Anderson, "Electron Microscopy of Solid Solutions and Crystallographic Shear Structures II. Fe_2O_3-TiO_2 and Ga_2O_3-TiO_2 Systems," *J. Solid State Chem.,* **5** [2] 212-25 (1972).

24. A. Kahn, V. Agafonov, D. Michel, and M. Perez Y Jorba, "New Gallium Germanates with Tunnel Structures: alpha-Ga_4GeO_8 and $Ga_4Ge_3O_{12}$," *J. Solid State Chem.,* **65** [3] 377-82 (1986).

25. S. Kamiya and R.J.D. Tilley, "Phase Relations in the Pseudobinary System TiO_2-Ga_2O_3," *J. Solid State Chem.*, **22** [2] 205-16 (1977).

26. D.J. Lloyd, I.E. Grey, and L.A. Bursill, "The Structure of $Ga_4Ti_{21}O_{48}$," *Acta Cryst.*, **B32** [6] 1756-61 (1976).

27. Y. Li, A. Trinchi, W. Wlodarski, K. Galatsis, and K. Kalantar-Zadeh, "Investigation of the Oxygen Gas Sensing Performance of Ga_2O_3 Thin Films with Different Dopants," *Sens. Actuators*, **B 93** [1-3] 431-4 (2003).

28. E. Kejnovsky and J. Kypr, "Millimolar Concentrations of Zinc and Other Metal Cations Cause Sedimentation of DNA," *Nucleic Acids Res.*, **26** [23] 5295-9 (1998).

29. P.R. Dahlgren and Y.L. Lyubchenko, "Atomic Force Microscopy Study of the Effects of Mg^{2+} and Other Divalent Cations on the End-to-end DNA Interactions," *Biochemistry*, **41** [36] 11372-8 (2002).

30. R.D. Shannon, "Revised Effective Ionic Radii and Systematic Studies of Interatomic Distances in Halides and Chalcogenides," *Acta Cryst.*, **A 32** [5] 751-67 (1976).

31. *Principles of Descriptive Chemistry*. Edited by G. Wulfsberg. Brooks / Cole, Monterey, CA, 1987.

32. *CRC Handbook of Chemistry and Physics*, 74th ed. Edited by D. Lide. Chemical Rubber Publishing, Boca Raton, FL, 1994.

33. J.F. Allemand, D. Bensimon, L. Jullien, A. Bensimon, and V. Croquette, "pH-dependent Specific Binding and Combing of DNA," *Biophys. J.*, **73** [4] 2064-70 (1997).

34. W. Han, S.M. Lindsay, M. Dlakic, and R.E. Harrington, "Kinked DNA," *Nature*, **386** [6625] 563 (1997).

35. C. Rivetti, M. Guthold, and C. Bustamante, "Scanning Force Microscopy of DNA Deposited onto Mica: Equilibration Versus Kinetic Trapping Studied by Statistical Polymer Chain Analysis," *J. Mol. Biol.*, **264** [5] 919-32 (1996).

36. A. Bensimon, A. Simon, A. Chiffaudel, V. Croquette, F. Heslot, and D. Bensimon, "Alignment and Sensitive Detection of DNA by Moving Interface," *Science*, **265** [5181] 2096-8 (1994).

37. D. Bensimon, J. Simon, V. Croquette, and A. Bensimon, "Stretching DNA with a Receding Meniscus: Experiments and Models," *Phys. Rev. Lett.*, **74** [23] 4754-7 (1995).

38. R. Izatt, J. Christensen, and J. Rytting, "Sites and Thermodynamic Quantities Associated with Proton and Metal Ion Interaction with Ribonucleic Acid, Deoxyribonucleic Acid, and Their Constituent Bases, Nucleosides, and Nucleotides," *Chem. Rev.*, **71** [5] 439-81 (1971).

39. G.L. Eichhorn and Y.A. Shin, "Interaction of Metal Ions with Polynucleotides and Related Compounds. XII. The Relative Effect of Various Metal Ions on DNA Helicity," *J. Am. Chem. Soc.*, **90** [26] 7323-8 (1968).

7. Summary and Conclusions

A series samples prepared as analogs of a sodium doped n=5 BGR intergrowth $A_xGa_{4+x}Ti_{1-x}O_8$ (A= Li, K, ~$0.1 \leq x \leq 0.7$) phases failed to form via solid state reaction at 1000 – 1350^{o}C. Phase analysis via X-ray diffraction generated a series of compatibility triangles, where the minimized lattice energies (via GULP computer modeling) of appropriate stoichiometric phases were compared to the lattice energy of the intergrowth phase. For the Li system the results from computer modeling supported those observed experimentally; where the minimized lattice energies of the observed phases were lower than those collected for an intergrowth phase. The modeling results collected from the A= Na and K trials suggested that mixes of the component oxides were the most energetically favorable combination which differed from what was observed experimentally, this difference could be due to the static nature of the simulation. An n=5 intergrowth was observed experimentally when doping with Na cations; however, a phase pure n=5 doped intergrowth was never observed.

BGR intergrowth substrates suitable for preferential DNA attachment were prepared by spin-coating gallium isopropoxide onto [001]-oriented TiO_2 single crystal slabs and heating above 1350^{o}C. The duration of firing at elevated temperature appears to influence the density of $\{210\}_r$ intergrowth lines. Exposure of BGR surfaces with DNA buffered solutions containing milli-molar additions of certain divalent metal chlorides ($NiCl_2$, $MgCl_2$, $MnCl_2$, $CoCl_2$, and $ZnCl_2$) resulted in the preferential attachment of DNA molecules along $\{210\}_r$ intergrowth regions of BGR with sufficient strength to allow imaging with tapping mode AFM. A method to determine the degree of preferential binding was developed and reported. The results of this study support the hypothesis that tunnel sites along $\{210\}_r$ intergrowth boundaries serve as preferential positions for divalent cation occupation as well as regions possessing a heightened affinity for DNA attachment..

Results conducted with a ladder-DNA solution yielded significant levels of variation in bound DNA density. In a follow-up study, a dramatic decrease in bound DNA concentration was observed to accompany increases in DNA solution age. The possible causes for the reduced DNA densities were: the formation and sedimentation of

DNA-attractive metal hydroxides, and / or an increase in degree of DNA networking with respect to time. By using only freshly prepared DNA solutions for later studies, the author has significantly reduced the deviation in collected DNA densities. For future experiments, the author cannot express enough the importance of using freshly synthesized DNA buffers while carefully monitoring solution pH, to limit the precipitation and sedimentation of metal hydroxides.

From studies with monosized 1000-bp DNA solutions containing additions of $CoCl_2$, $MgCl_2$, $NiCl_2$, and $ZnCl_2$ at 0.5, 1.0, and 5.0 mM concentrations it was determined that increasing the salt concentration from 0.5 to 1.0 mM led to increases in attached DNA density, while further salt addition to a level of 5.0 mM led to decreased DNA attachment. These results agreed with data reported for DNA binding to mica surfaces. The results of our study support hypotheses including the mass action, precipitated salt, and induced molecular aggregation effects to explain this decrease. Substrate pretreatment (with 10 mM salt solutions) was not sufficient to bind significant quantities of DNA molecules from solutions containing no cation additions. Additionally, the fact that at 0.5, 1.0, and 5.0 mM concentrations produce an excess of ~10,000 to 100,000 more cations (~6×10^{14} to 6×10^{15}) than tunnel sites (~2×10^{10}) would suggest that the DNA – cation interaction is more important. Interestingly, at a DNA concentration of 0.5 µg / ml and a drop volume of 0.002 µl, approximately 2×10^{15} negative binding sites are available for cation binding, suggesting that within the 0.5 to 5.0 mM range of salt concentrations the entire binding sites along all of the DNA molecules could become saturated. If saturation of DNA molecules is occurring, excess divalent cations could begin to inhibit the intimate interaction required to bind the DNA molecules with the BGR surface. Testing additional cation concentrations between 0.5 and 5.0 could prove beneficial to help identify at what cation concentration the maximum DNA attachment is occurring.

Of the four cations tested, solutions containing Zn (II) appeared to bind the lowest amount of DNA. The lower DNA surface densities were attributed to factors including zinc-hydroxide / -salt precipitation, as well as the cations' heightened predilection for molecule aggregation. Bound DNA end-to-end distances were examined to provide

qualitative estimates of the molecule to surface binding strength; which appeared to increase as a function of cation concentration.

Comparing data collected from DNA solutions containing differing salt concentrations and divalent cation species has proven that altering these variables could allow for the optimization of binding conditions to suit unique applications. For instance, if DNA–protein interaction is the focus of a study, the DNA molecule should be accessible to the protein. A loosely bound conformation would be more desirable; to achieve such a conformation lower salt concentrations should be selected. Although the roughness of currently synthesized BGR surfaces may inhibit the identification of more intimate features of DNA structure, the substrate does succeed in providing a surface for the site-specific attachment of DNA without additional / cumbersome functionalization steps required with alternate substrates.

7.1. Future Directions

7.1.1. BGR substrate

While preparing BGR substrates via spin coating we generally observed the random orientation of intergrowth lines among different members of the $\{210\}_r$ family of planes. In some instances, the parallel alignment of the intergrowth lines was observed. Future research to clarify the factors governing intergrowth alignment will be vital to enable BGR surfaces to act as DNA patterning substrates. The random orientation of $\{210\}_r$ intergrowth boundaries is believed to be due to the formation of a variety of n value BGR phases, attributed to the inhomogeneous application of beta-gallia. Controlling the surface chemistry during synthesis of BGR intergrowths could lead to the formation of oriented, periodically spaced $\{210\}_r$ boundaries. For BGR to simply act as surfaces for AFM examination of DNA molecules, methods to achieve a flatter, smoother surface will be needed.

7.1.2 Application of DNA

Isolating the influence of DNA solution age significantly reduced the deviation in bound DNA surface densities, but a noticeable degree of deviation remains. The DNA solution application process was sufficient to characterize trends and analyze process variables, but the presence of un-scanable regions of dried buffer limited surface uniformity. The lack of uniformity within the same sample could be attributed to the drying process. The introduction of alternate coating procedures like spin or dip-coating may help to produce more uniform DNA distributions. However, the forces inherent to these methods may produce stretched DNA molecules (or remove DNA altogether), masking proper DNA end-to-end distances.[1-3] Humidity too has been shown to significantly influence the imaging of DNA molecules with the AFM. Higher humidity can lead to more hydrated DNA molecules, as well as heightened AFM tip-to-surface interaction (the increase in adsorbed water at the tip increases the tip-meniscus scanning force) which could remove more strongly bound DNA molecules.[4-7] Controlling the humidity of the scanning (in air) environment could prove costly and cumbersome, but performing AFM under fluid would effectively remove the drying and humidity effects, possibly producing a more reliable result. Additionally, the nano-fabrication of molecular constructs and devices will most likely be conducted in fluid, so understanding the interaction between DNA and BGR surfaces in fluids would be of considerable importance.

7.1.3 Binding mechanism

Conducting similar experiments with circular plasmid DNA at varying divalent cation concentrations may help clarify the mechanism of attachment by studying solely backbone interactions. It was observed that at lower cation concentrations, the more negatively charged endpoints are believed to bind first, using circular DNA molecules removes all DNA endpoints. If the quantity of bound DNA is greatly decreased for plasmid DNA, the importance of DNA endpoints to surface attachment could be identified.

7.2. References

1. M. Sasou, S. Sugiyama, T. Yoshino, and T. Ohtani, "Molecular Flat Mica Surface Silanized with Methyltrimethoxysilane for Fixing and Straightening DNA," *Langmuir,* **19** [23] 9845-9 (2003).

2. H. Yokota, J. Sunwoo, M. Sarikaya, G. van den Engh, and R. Aebersold, "Spin-Stretching of DNA and Protein Molecules for Detection by Fluorescence and Atomic Force Micrsocopy," *Anal. Chem.,* **71** [19] 4418-22 (1999).

3. H. Zheng, D. Pang, Z. Lu, Z. Zhang, and Z. Xie, "Combing DNA on CTAB-coated Surfaces," *Biophys. Chem.,* **112** [1] 27-33 (2004).

4. A. Engel, Y. Lyubchenko, and D. Muller, "Atomic Force Microscopy: A Powerful Tool to Observe Biomolecules at Work," *Trends Cell Biol.,* **9** [2] 77-80 (1999).

5. H. Hansma, J. Vesenka, C. Siergerist, G. Kelderman, H. Morrett, R. Sinsheimer, V. Elings, C. Bustamante, and P. Hansma, "Reproducible Imaging and Dissection of Plasmid DNA Under Liquid with the Atomic Force Microscope," *Science,* **256** [5060] 1180-4 (1992).

6. T. Thundat, R.J. Warmack, D.P. Allison, L.A. Bottomley, A.J. Lourenco, and T.L. Ferrell, "Atomic Force Microscopy of Deoxyribonucleic Acid Strands Adsorbed on Mica: The Effects of Humiditiy on Apparent Width and Image Contrast," *J. Vac. Sci. Technol. A,* **10** [4] 630-5 (1992).

7. J. Yang and Z. Shao, "Effect of Probe Force on the Resolution of Atomic Force Microscopy of DNA," *Ultramicroscopy,* **50** [2] 157-70 (1993).